STRUCTURAL AND MORPHOLOGICAL INVESTIGATION OF CARBON BASED MATERIALS FOR ELECTROCHEMICAL APPLICATIONS

A Dissertation

by

SWARN JHA

Submitted to the Graduate and Professional School of
Texas A&M University
in partial fulfillment of the requirements for the degree of

DOCTOR OF PHILOSOPHY

Chair of Committee,	Hong Liang
Committee Members,	Michael Pate
	Matt Pharr
	Mahmoud El-Halwagi
Head of Department,	Guillermo Aguilar

December 2021

Major Subject: Mechanical Engineering

Copyright 2021 Swarn Jha

ABSTRACT

Bio-derived carbon-based-supercapacitor electrodes present an economical solution as sustainable sources for energy storage. Serious knowledge gaps exist for bio-derived carbon electrodes in terms of causes of largely unknown surface chemistry, poor volumetric energy density, and uneven pore structure and distribution which adversely affect electrochemical performance, cost, and scalability. To date, it is not yet clear how the electrochemical performance is affected by chemical composition and molecular structure in bio-derived carbon. In addition, the relation of surface morphology and microstructure with electrochemistry has not been established. This research attempts to fill those knowledge gaps with new understanding of the effects of bio-derived carbon structure and morphology on electrochemical performance.

The goal of this research is to obtain new knowledge in terms of biomass electrochemistry to design and engineer sustainable and high-performance electronics. To reach the goal, this research will investigate the structural and morphological characteristics of lignin based materials and their effects on electrochemical performance as electrodes. Specifically, it is intended to understand 1) how the presence of different chemical structures and 2) particle morphologies of lignin affect the charge storage and cycle life of a quasi solid-state supercapacitor. To carry out the research, experimental approaches combined with theoretical analysis will be conducted. Specific tasks include fabrication, assembly, test, analysis, and optimization of supercapacitor electrodes using various bio-derived lignin differing in structural identity and morphological features.

Lignin varying in structural identity (alkaline lignin (AL), lignosulfonate (LS), and dealkaline lignin (DAL)) and morphology (micro-fiber lignin and nano-spherical lignin) are used to evaluate electrochemical behavior. Specific capacitance, retention, impedance, energy, and power density results are compared and analyzed.

This research generates new knowledge in understanding lignin electrochemistry that will aid in significant advances in the future design of bio-derived carbon based electrochemical devices. Novel synthesis processes for electroactive lignin micro and nanoparticles will be developed. Unique design of lignin supercapacitors will be accomplished and improved to attain high performance.

This thesis contains seven chapters. Following the background introduction in Chapter I, the motivation and objectives of this work are presented in Chapter II. This is followed by the research on structural investigation of micro-lignin fibers: electrochemical behavior of alkali lignin fibers (Chapter III), transition metal oxide ($NiWO_4$) nanoparticles doped lignin (Chapter IV), and effects of hydrothermally impregnated MnO_2 particles on lignin fibers (Chapter V). Structural investigation on nano-spherical lignin particles is covered in Chapter VI. Finally, a summary and commentary on future directions of research are provided in Chapter VII.

ACKNOWLEDGMENTS

I would like to extend my gratitude and a heartfelt thank you to my research advisor Dr. Hong Liang for her excellent guidance, support, and encouragement throughout the duration of this research work and for being a wonderful advisor. I would also like to thank my research committee faculty members Dr. Pate, Dr. Halwagi, Dr. Pharr, and Dr. Pharr for their continued guidance and support.

I would like to thank my mother Mrs. Prabha Jha and father Mr. Paras Nath Jha for supporting me throughout this journey and always being there for me. I thank my sisters Binti Jha, Babli Jha, nieces (Shuvangi and Sharda), grandfather Mr. Anant Pathak and all my family members for their continued support and encouragement.

I thank surface science group lab mates, in particular, Siddhi Mehta and Yan Chen for their help during my research. A great thanks to my dear friends Prasanth, Sourav, Warren and all other friends at Texas A&M who made this journey fun and a great experience. I thank my undergrads from the Aggie Research Program whom I mentored and who helped me a great deal in research work.

I would like to extend my gratitude to the graduate advisor Dr. Rasmussen, Dr. Li, Dr. McAdams, Dr. Polycarpou, and Dr. Guillermo Aguilar graduate program specialist Mrs.

Rebecca Simon, Ms. Sandy Havens, and other faculty members of the department of Mechanical Engineering who helped me immensely from time to time.

A great thank you to the Texas A&M Engineering Experiment Station, STLE Houston, and Texas A&M University Libraries for the resources used during this research.

CONTRIBUTORS AND FUNDING SOURCES

All work for the thesis was completed by the student, under the advisement of Dr. Hong Liang of the J. Mike Walker'66 Department of Mechanical Engineering.

There are no outside funding contributions to acknowledge related to the research and compilation of this document.

TABLE OF CONTENTS

CHAPTER V DESIGN AND SYNTHESIS OF HIGH PERFORMANCE FLEXIBLE AND GREEN SUPERCAPACITORS MADE OF MANGANESE-DIOXIDE-DECORATED ALKALI LIGNIN……………………….………………...122

LIST OF FIGURES

LIST OF TABLES

Page

CHAPTER I

INTRODUCTION

1.1 Supercapacitors

Finding new, effective, and sustainable solutions to face the challenges posed by the energy demands are crucial for economy and environment [1-4]. In this regard, both energy production and energy storage technologies need drastic improvements to meet those challenges. [5, 6]. New materials for energy storage, such as in lithium-ion batteries, have been extensively focused in recent research [7-10]. Batteries and supercapacitors have been the key focus of enhancing energy storage [7, 9, 11-15]. Recently, supercapacitors have gained a lot of attention for their high specific capacitance, energy density, and power density which are clearly more advantageous over the conventional dielectric capacitors [16-21].

A supercapacitor (SC) is a high-capacity capacitor with capacitance values much higher than other capacitors (but lower voltage limits) that bridges the gap between electrolytic capacitors and rechargeable batteries (Figure 1.1) [22]. They store 10 to 100 times more energy per unit volume or mass than electrolytic capacitors and deliver charge much faster than batteries. For instance, a 7 μm thick micron size supercapacitor, which used AC electrode and 1 M Et_4NBF_4/propylene carbonate electrolyte, had a specific capacitance of 0.9 $mF\cdot cm^{-2}$ at a scan rate of 100 $V\cdot s^{-1}$ [23]. Liu et al. prepared an electrochemical micro-capacitor with carbon nanotube (CNT) composite electrodes by thin-film technology and making use of photolithography. Specific capacitance reported by them was 36.5 Fg^{-1}, energy density reported was ~0.4 $Wh \cdot kg^{-1}$ while the specific power reported was ~1 $kW \cdot kg^{-1}$ [24].

An all-solid-state supercapacitor is highly sought due to the ease of portability and use. Additionally, the use of solid-state supercapacitors eliminates the safety risk posed by conventional liquid electrolytes which are combustible and bulky [25]. As such, considerable efforts are directed towards the fabrication of solid-state supercapacitors [26]. In the last decade, there is a rising trend to produce flexible supercapacitors due to exponential growth in the flexible electronics industry [27-29]. Flexible devices offer the advantage of being used in conditions of additional strains without diminished performance. The bandwidth of application of wearable flexible electronics is huge, ranging from human wearable watches and clothing to sensors used in automobiles [30, 31]. As such, a number of research efforts are directed towards the fabrication, design, and synthesis of solid-state flexible supercapacitors [32-34]. The asymmetric design of a supercapacitor is beneficial in extending the potential window by employing one electrode for Faradic reactions, and the other as a capacitor for improved power density.

Recently, several carbon-based materials are used as supercapacitor electroactive material. Some examples include graphene, graphite, activated carbon, carbon nanotubes (CNTs), carbon hollow spheres and carbon fibers [35, 36]. Furthermore, various combinations of electrodes and electrolytes are used in different designs with varying levels of success in terms of obtained specific capacitance, energy density, power density, capacity retention, and coulombic efficiency.

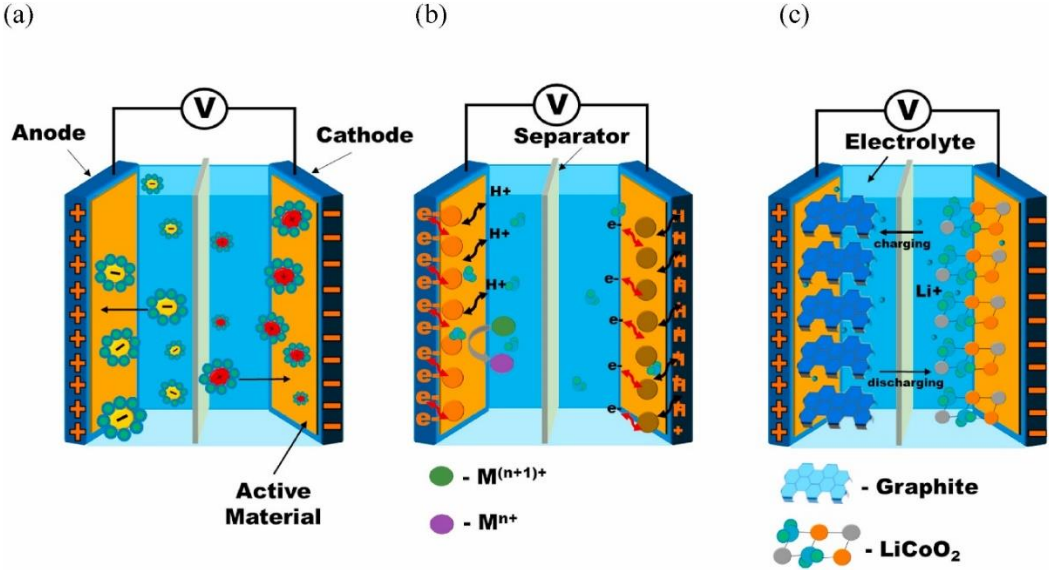

Fig. 1.1 Figure showing a) electric double layer capacitor (EDLC), b) pseudocapacitor, and c) battery charge storage mechanisms.

1.2 Plant-based carbon for energy storage

Carbon is one of the most widely used element for energy storage applications. However, the inorganic carbon derived from traditional sources is non-biodegradable. Energy storage devices that employ traditional sources of carbon lead to problems like electric wastes and environmental pollution. This has necessitated reliance on renewable sources like the plant based carbon. Carbon forms the backbone of naturally occurring polymers like lignin, cellulose, and hemicellulose. Plant based carbon is a clean, abundant, and renewable resource.

Plant-based carbon has a complex chemistry that is largely not understood. For electrochemical applications, both the chemical structure and morphology of the plant carbon is important. Chemical structure reveals the presence of functional groups, bonding, chain length, chain orientation etc. Morphology reveals the shape of molecule, surface, porosity, pore size and distribution etc. Hence, in order to have a comprehensive understanding of the electrochemical behavior of plant carbon, both its structure and morphology needs to be studied [37-39].

1.3 Lignin as electroactive material for energy storage

Plant based lignin has tremendous potential for energy storage device. Some advantages of lignin are low cost, renewability, favorable functional groups, high diversity, high carbon content, and huge reserves. Present applications of lignin include energy storage resins, asphalt, ethanol production, electrode materials, conversion, electrolytes, binders, and production of porous carbons. However, lignin output remains low in global industries despite lignin stock being ranked the second most abundant biomass following cellulose [39, 40]. The issues that prevent higher commercial utilization of lignin in chemical and materials industries are its structure complexity, low solubility, incompatibility with host matrices, and varied molecular weight when unmodified. Therefore, critical research in lignin’s pretreatment methods, mechanisms, functional groups, and monolignols is imperative to increasing the application of lignin in several sectors.

1.3.1 Pretreatments of Lignin

The diversity of lignin’s functional groups makes it possible to modify lignin to be applied to several areas, such as chemical catalysis and material synthesis [37]. Specific pretreatments and manufacturing methods are used for the structural deconstruction of lignin. It has been proposed that breaking the bonds between lignin and carbohydrates can enhance monosaccharide yield, reduce particle size, increase pore size, accessibility surface area, solubility, decrease energy needs, and ensure amenability to post-treatments [38-40]. These properties of product lignin can be considered valuable in commercial applications, such as carbonaceous materials. Unfortunately, plant materials have a highly fused structure of carbohydrates and lignin. This remains the main challenge for its extraction from various sources. Further complications arise when condensation and oxidation reactions occur simultaneously when isolating pure lignin. At the same time, effective lignin conversion can be approached through a variety of specific pretreatments, such as physical, physio-chemical, chemical, and biological methods [41]. Pretreatments aim to produce desired compounds through the cleavage of aryl–/alkyl–ether, CC, and ester bonds. This goal can be achieved by hydrolysis, demethoxylation, condensation, and alkyation reactions [42]. Reduction in particle size (a few millimeters to 5 centimeters) and a decrease in cellulose crystallization are evident effects of physical pretreatments, such as grinding, milling, and cutting, mechanical methods. Further cellulose decrystallization promotes an increase in pore size and accessibility of the surface area of the substrate [41]. An increase in carbonyl and phenolic groups while cleaving β–O-4 linkages is the resulting composition of lignin brought by mechanical pretreatments. Similarly, the degradation of lignin can be facilitated by a variety of microorganisms through enzymatic hydrolysis [43]. Biological pretreatments are primarily fueled by white-rot fungi species: Phanerochaete chrysosporium, Phlebia radiata, Dichmitus squalens, Rigidosporus lignosus and Junguasepar abilima [44]. Their potency in secreting enzymes allows for the delignification and depolymerization of lignin, which then promotes amenability to saccharification [45]. Therefore, this plant material degrading process is not only eco-friendly, but also cost-effective. In another route, strong acids, alkalis, organic solvents, and ionic liquids can be used to chemically break its linkages. Particularly, acid pretreatments predominantly depolymerize lignin by the cleavage of β–O-4 bonds. Alkaline treatments, such as soaking in sodium hydroxide, have been found to increase porosity and surface area through effective delignification. In fact, these advantages occur in mild reaction conditions where interactions with hemicellulose is minimized. Physico-chemical pretreatments intend to ameliorate direct microbial use after enzymatic saccharification of polysaccharides and sugar yields.

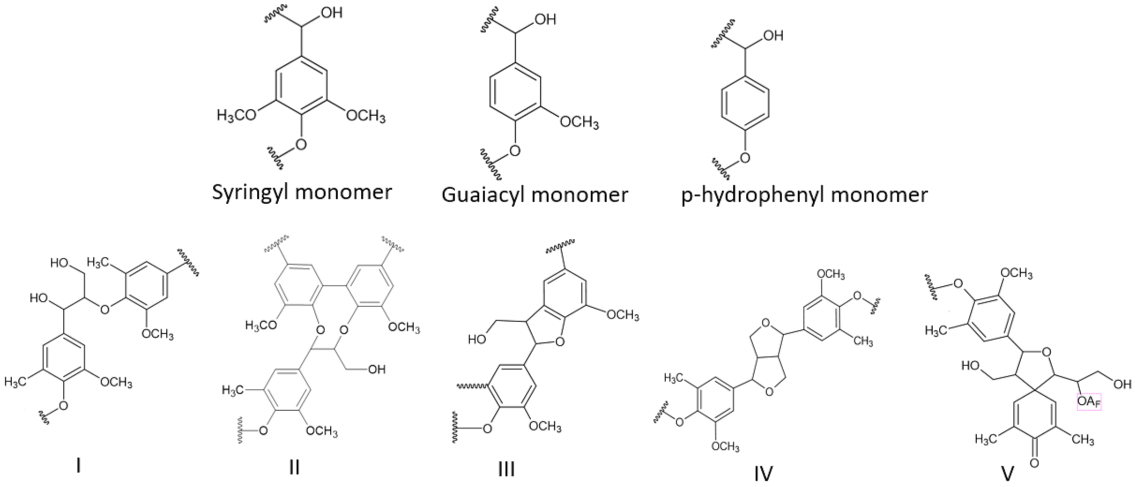

a) Lignin structural units

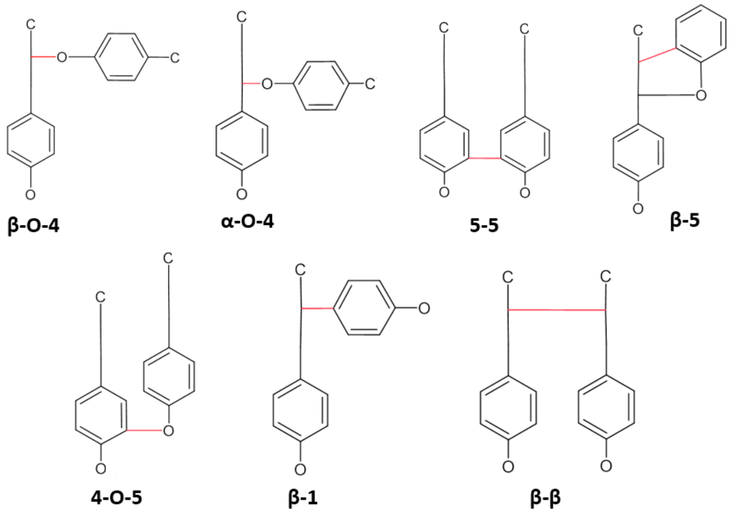

b) Linkages

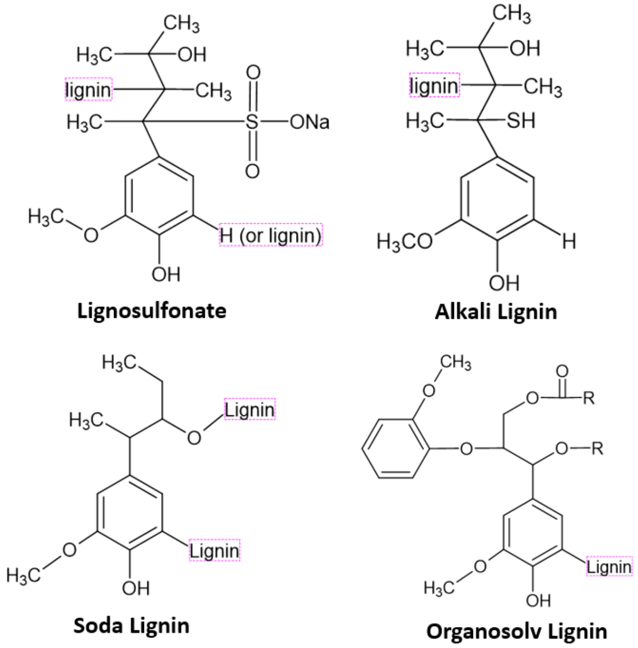

c) Lignin structural variants

Fig. 1.2 Lignin structures.

1.3.2 Structure of Lignin

Lignin is a complex biopolymer with an amorphous and cross-linked structure that is produced by plants for structural support and rigidity (Figure 1.2). Lignin's heterogeneous molecular weight is largely dependent on the plant source. The polymeric framework of lignin has many structural irregularities when comparing vascular plants. In most vascular plants, ether and carbon-carbon bonds connect several distinct methoxylated phenylpropanoid units through oxidative combinatorial coupling, forming an amorphous three-dimensional macromolecule. Proportional differences of the monomers (monolignols) of lignin are the reason for the structural irregularities. Primary functional groups methoxyl, ether, and benzyl constitute the chemical structure of monolignols, which are interlinking units of methoxylated hydroxycinnamyl alcohols that form the complex heterogeneity polymer structure of lignin.

Table 1. Chemical classification of lignin based on monomeric units and linkage types

Constituent	Hardwood (%)	Softwood (%)	Grasses (%)
β-*O*-4′	60	45-50	
5-5′	5	18-25	
β-5′	6	9-12	
β-1′	7	7-10	
α-*O*-4′	7	6-8	
4-*O*-5′	7	4-8	
β-β′	3	3	
p-Coumaryl alcohol	0-8	< 5	5 -35
Coniferyl alcohol	25 - 50	> 95	35-80
Sinapyl alcohol	45 -75	0	20-55

Monolignols units being 4-hydroxyphenyl (H unit), guaiacyl (G unit), and syringyl (S unit) derivatives are similar in considerable respect to the formation of aromatic, aliphatic ether bonds with β-O-4′ and α-O-4′ linkages (Figure 1.2). These linkages present in lignin determine the degree of branching and reactivity. Table 1 shows the chemical classification of lignin based on monomeric units and linkage types. Attached to the basic phenylpropanoid skeleton, benzylic hydroxyl, phenolic hydroxyl, and carbonyl groups have the most prominent effect on the reactivity of lignin polymers in modification reactions, such as sulfomethylation with formaldehyde and bisulfite. Precursors of methoxylated hydroxycinnamyl alcohols include coniferyl alcohol, p-coumaryl alcohol, and sinapyl alcohol which are biosynthesized through catalysis reactions of several enzymes from L-phenylalanine. Key distinctions amongst these three units arise due to the degree of methoxylation on the benzene ring. Furthermore, lignin is amphiphilic in nature as a result of the biopolymer's functional groups, such as methoxyl, ether, hydroxyl, carboxyl, benzel, etc. Most of the functional groups are polar, which in turn stimulates the interactions between lignin molecules. The weight percentage distribution of key elements in industrial grade lignin is shown in Table 2.

Table 2. Industrial lignin element weight percentage distribution

	H	C	S	N
Kraft lignin	5.8	62.8	0.1	0.9
Organosolv	5.9	61.1	<0.02	0.3
Lignosulfonate	3.7	47.9	2.0	0.2
Soda lignin	5.9	61.9	<0.02	0.9

1.4 Relation to the present state of knowledge in the field

1.4.1 Knowledge Gaps in the Use of Bio-derived Carbon Electrodes

Biomass-derived carbon materials have been used for electrochemical applications owing to their environmental benefits. However, there are serious knowledge gaps for bio-derived carbon made electrodes in terms of causes of poor volumetric energy density, unoptimized pore structure and distribution, and unknown surface chemistry which affect electrochemical performance, retention, stability, and long term usage [46]. Moreover, such unoptimized usage also creates problems of electric wastes, bio-degradability, processing cost, and scalability [47]. These challenges have not only made commercialization of biomass-based electrochemical devices difficult, but also have raised concerns on the potential of biomass materials as a whole for electrode applications. Besides, the source, extraction, and processing steps involved in obtaining bio-derived carbon materials are crucial factors that impact device performance and usability. Accordingly, there is an urgent need to address these knowledge gaps through an innovative and rigorous approach that is consistent with the principles of green chemistry. This research seeks to understand the effects of bio-derived carbon structure on electrochemical performance.

1.4.2 Knowledge Gaps in the Fundamental Chemistry of Bio-derived Carbon Electrodes

The fundamental science of bio-derived carbon reactivity is still a mystery owing to its highly diversified and complicated structure and varied chemical composition. It is not clear how the electrochemical performance is affected by the choice of different functional groups, and related chemistry in biomass. Also, the relation with surface morphology and microstructure with electrochemistry remains vague, which is important to tailor new electrode material design. One big challenge in biomass is to achieve higher porosity for higher pseudocapacitance. But this comes at the cost of sacrificing electrical conductivity because higher porosity leads to lesser electrical conductivity due to pore impedance [48]. Hence, understanding in detail the microstructure and morphologies which can marry higher porosity with higher electrical conductance hold the key to better design. This research seeks to understand the effects of bio-derived carbon morphology on electrochemical performance.

1.4.3 Knowledge Gaps in the Use of Optimal Process for Bio- derived Electrodes

Most existing techniques of producing carbon fibers from biomass like electrospinning, ink-jet printing or spraying use hazardous chemicals, expensive process, and have a high carbon footprint [49]. For instance, Schlee et. al used bio-derived carbon using salt-based oxidation and electrospinning since the widely used PAN fibers use hazardous chemicals and are expensive to obtain [50]. Varied reaction products impart a high degree of impurity to bio-derived carbon for use as electrodes. Bio-derived carbon obtained from the paper and pulp processing yields comparatively fewer impurities. High oxygen content in some bio-derived carbon is very good for pseudocapacitance properties [51]. However, this also limits the electrical conductance. A compromise is thus needed to either go for an expensive process or using bio-derived carbon with the modified process. Jeon et al tried chemical-free activation using a one-step process to control the pores [51]. Going ahead, life cycle analysis is very important to properly evaluate and compare the processing techniques. It is not enough that a process produces high performance. Aspects of carbon footprint, inherent use of less hazardous chemicals, waste minimization, biodegradability are equally important in addition to the process being low cost and reliable for scalable production. This work seeks to address an impending need for understanding the feasibility of a simpler and safe activation process which can yield high performance.

1.4.4 Knowledge Gaps in Functionalization of Bio-derived Carbon with Transition Metal Oxides (TMO)

Transition metal oxides (TMO) have a tendency to exhibit a wide variety of structures. For instance, MnO_2, ZnO, CoO, NiO, RuO_2, and CuO are highly sought candidates for supercapacitor applications. They are generally used in combination with other electroactive materials like carbon, carbon nanotubes (CNTs), carbon fibers, and carbon nanospheres due to their ability to enhance charge transport [52-55]. This leads to higher specific capacitance compared to the conventional electric double-layer capacitor (EDLC) on account of enhanced interfacial Faradic reactions. MnO_2, in particular, is widely favored over others since it is not only cheaper but also readily available and safer [56, 57]. A major drawback of MnO_2 is its poor electrical conductivity (10^{-5} – 10^{-6} S cm^{-1}) which poses a limitation on the bulk utilization of MnO_2 [58]. In order to overcome the drawbacks posed by AC and MnO_2, the proposed research seeks to understand the pseudocapacitance properties of novel class transition metal oxides with bio-derived carbon. Nanosized transition metal oxides, in particular, have the potential of higher substrate permeability, and high surface area to volume ratio, which leads to greater contact area for electrochemical reactions. Due to low cost, facile preparation method, high theoretical specific capacitance, excellent electrochemical reversibility, and abundant availability, nickel-based materials have been considered as one of the most important electrode candidates. As per the recent study, microstructure and configuration have a profound influence on an electrode performance, and this enables to design new electrodes [11, 59-61]. In this work, novel class of Ni based transition metal oxide nanomaterial, is investigated.

CHAPTER II

MOTIVATION AND OBJECTIVES

2.1 Motivation

There are varied literature reports on bio-derived carbon for use in energy storage, particularly supercapacitors. However, a majority of reports are on carbon fibers derived from highly hazardous Polyacrylonitrile (PAN). Some other reports cover the use of bio-derived carbon in supercapacitors through expensive and high carbon footprint processes like electrospinning. There is a knowledge gap in the use of bio-derived carbon and its derivatives in supercapacitor applications. In particular, it is not understood as to how different bio-derived carbon structures and functional groups affect the electrochemical performance of a supercapacitor. This work seeks to bridge this knowledge gap: how the structure and morphology affect the electrochemical performance when bio-derived carbon is used in supercapacitor applications. It also seeks to understand the feasibility of using low cost and easily available bio-derived carbon using a safe, non-hazardous, and a process aligned with the principles of green chemistry for supercapacitor application. Moreover, the design process seeks to address the knowledge gap in achieving high specific capacitance and high electrode conductance at the same time for biomass-derived electrodes.

2.2 Objectives

The research proposed will provide new knowledge in terms of the effects of structure and morphology of bio-derived carbon on its electrochemical behavior when used in solid-state supercapacitor.

Objectives are to test the hypotheses regarding the effects of:

1) varying molecular structure (chemical identity) and

2) morphology on the electrochemical behavior of bio-derived carbon.

For the first objective, bio-derived carbon varying in structural identity (e.g., presence of specific functional groups, bonds, isomers, carbon-chain) will be used to evaluate electrochemical behavior. For the second objective, bio-derived carbon varying in morphology (e.g., spherical, fiber) will be used to evaluate electrochemical behavior. Specific capacitance, retention, impedance, energy, and power density results of each will be compared and analyzed.

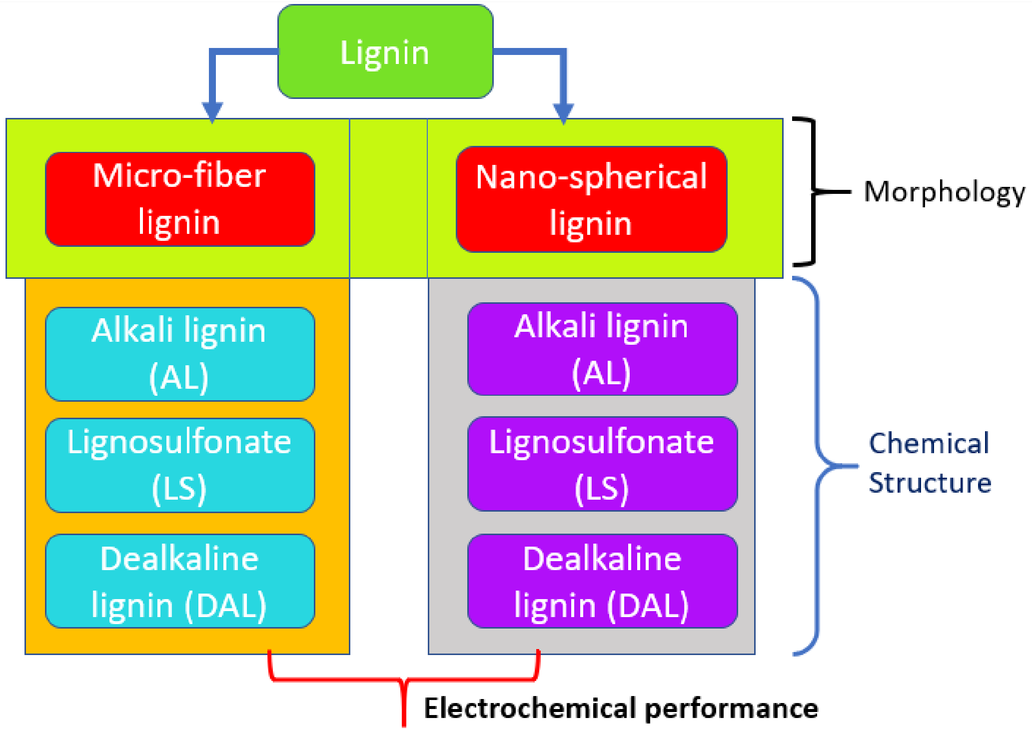

Fig. 2.1 Research plan for investigating structure and morphology of lignin.

2.3 Task-wise research plan

Fig. 2.1 shows the general flow diagram for the proposed work. In Fig. 2.2, the applied aspect of the work is captured. With material design being the focus, the proposed work will use several low-cost synthesis techniques like hydrothermal synthesis, and microwave synthesis. Both material and morphological characterization will be done. Performance tests will comprise of electrochemical, durability, and flexibility tests. The effects of structural and morphological aspects of bio-derived carbon will then be combined into a new understanding for device application. Task-wise research plan is as per below:

1) Identifying different variants of bio-derived carbon differing in structure and functional groups due to processing and pretreatment methods used.

- Carbon derived from plants varies in structure due to various intermediate processing and pre-treatment methods used. This part of the work will decipher various structures and functional groups in AC using experimental methods like spectroscopy (UV-vis, IR, XPS, Raman) chromatography, tomography, etc. It will also detail the molecular and atomic species present and clearly outline the different types of bonding and structural differences based on pre-processing and sources.

2) Carrying out electrochemical tests on different bio-derived carbon variants.

- This task will focus on performing electrochemical tests using bio-derived carbon as an active material. This will have two parts: EDLC tests and pseudocapacitance tests. In the EDLC tests, bio-derived carbon from specific source and processing will be evaluated in supercapacitor performance. In pseudocapacitance tests, bio-derived carbon will be functionalized with transition metal oxides nanoparticles (TMOs) to test in pseudocapacitance based supercapacitor. Several electrochemical tests will be carried out which include-Cyclic Voltammetry (CV), Cyclic charge-discharge (CCD), Electrochemical impedance spectroscopy (EIS), etc.

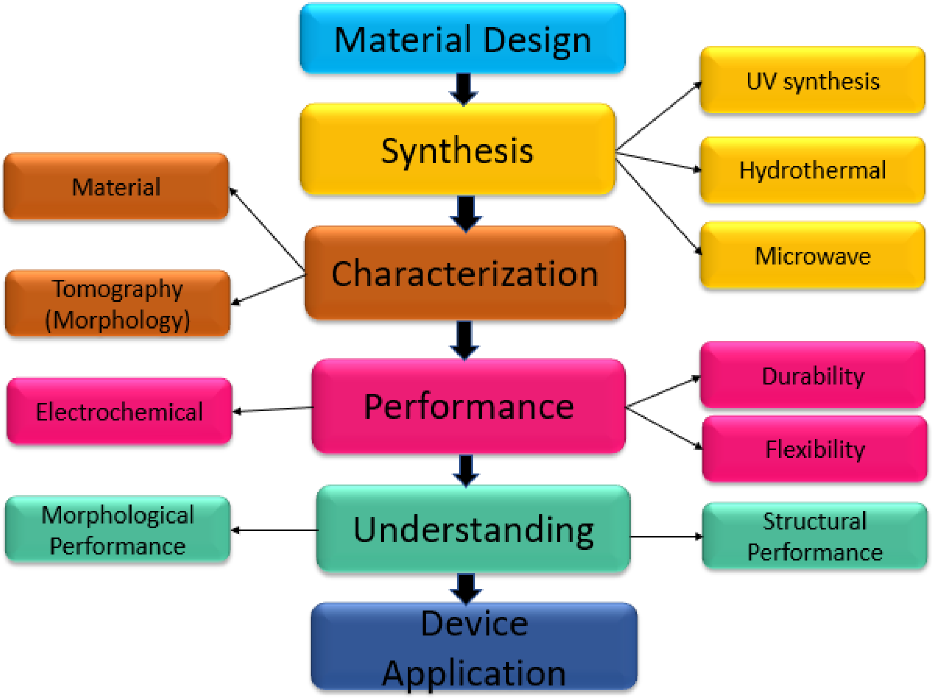

Fig. 2.2. Proposed project flowchart.

3) Analyzing and evaluating of electrochemical performance.

-From the electrochemical tests the voltage-time, current-time, power density, energy density, impedance behavior, coulombic efficiency, current density vs specific capacitance, specific capacitance versus cycles and retention plots will be obtained, evaluated and compared. Structural characterization experiment data will be analyzed and evaluated with corresponding electrochemical performance.

4) Optimization of constituents to obtain the best performance of the supercapacitor.

- Each supercapacitor fabricated will be optimized for performance by running several trials with varying composition of constituents. In this, the composition of AC: binder (EDLC), and AC:TMOs will be varied to arrive at optimal proportions of these constituents.

CHAPTER III

STRUCTURAL INVESTIGATION OF MICRO LIGNIN FIBERS*

Due to the immense demand for flexible supercapacitors, it is important to develop low-cost and smarter solutions. To date, supercapacitors made of eco-friendly materials have been either expensive or of limited use. Herein, we report a solid-state, lightweight, low cost, and plant-based supercapacitor for applications in flexible electronics. The asymmetric supercapacitor is made of MnO_2 deposited on activated carbon and lignin as substrate using hydrothermal deposition. With Al/AC/lig-MnO_2 anode, and Al/AC cathode, the supercapacitor is assembled using PVA/H_3PO_4 gel electrolyte. Morphological characterization is conducted using microtomography and scanning electron microscope. Electrochemical performance is assessed using cyclic charge-discharge, cyclic voltammetry, and Electrochemical Impedance Spectroscopy. A series of compositions of AC:lignin:MnO_2 are optimized for best performance. After 2000 cycles, the specific capacitance obtained at 6.01 mAg^{-1} is 5.52 $mFcm^{-2}$, which is up to 13 times reported. Retention is 98.7% after 1000 cycles, and 97.5% after 2000 cycles. The maximum energy density, power density and coulombic efficiency obtained are 14.11 $Whkg^{-1}$, 1 $kWkg^{-1}$, and 98% respectively. The favorable electrochemical performance makes it useful for a wide variety of electronics. This new approach to fabricate

---

*Reprinted with permission from "Design and Synthesis of Lignin Based Flexible Supercapacitor" by Swarn Jha, Siddhi Mehta, Yan Chen, Lian Ma, Peter Renner, Dilworth Y. Parkinson, Hong Liang, 2020. ACS Sustainable Chemistry & Engineering, 8, 498–511, Copyright [2020] by American Chemical Society.

electrodes from green sources, with constituent optimization and cost-effectiveness, marks an important step towards green energy technology development.

3.1 Background

One of the key challenges facing the world in the near future is that of clean and sustainable sources of energy [1-4]. In this regard, both energy production and storage technologies need to be improved to meet the ever-rising demand for energy technologies. In our recent research, we have studied critical materials for lithium-ion batteries. Environmentally friendly materials are important for sustainability [8, 9, 59]. Batteries and supercapacitors have been widely researched to enhance energy storage, and considerable progress has been made in recent decades [9, 11-15, 59]. Our recent study indicated that the microstructure and configuration have profound influence on the performance of electrodes. This enables us to design new electrodes in the present work [8, 11, 59, 61]. Recently, supercapacitors have gained a lot of attention for their high specific capacitance, energy density and power density which are clearly more advantageous over the conventional dielectric capacitors [16-20, 62]. A supercapacitor (SC) is a high-capacity capacitor with capacitance values much higher than other capacitors (but lower voltage limits) that bridges the gap between electrolytic capacitors and rechargeable batteries [21]. They store 10 to 100 times more energy per unit volume or mass than electrolytic capacitors and deliver charge much faster than batteries. For instance, a 7 μm thick micron size supercapacitor, which used AC electrode and 1 M Et_4NBF_4/propylene carbonate electrolyte, had a specific capacitance of 0.9 $mF \cdot cm^{-2}$ at a scan rate of 100 $V \cdot s^{-1}$ [25]. Liu et al. prepared an electrochemical micro-capacitor with carbon nanotube (CNT) composite electrodes by thin-film technology and making use of photolithography. Specific capacitance reported by them was 36.5 Fg^{-1}, energy density reported was ~0.4 $Wh \cdot kg^{-1}$ while the specific power reported was ~1 $kW \cdot kg^{-1}$ [26]. An all-solid-state supercapacitor is highly sought due to the ease of portability and use. Additionally, the use of solid-state supercapacitors eliminates the safety risk posed by conventional liquid electrolytes which are combustible and bulky [27]. As such, considerable efforts are directed towards the fabrication of solid-state supercapacitors [28]. In the last decade, there is a rising trend to produce flexible supercapacitors due to exponential growth in the flexible electronics industry [29, 30, 32]. Flexible devices offer the advantage of being used in conditions of additional strains without diminished performance. The bandwidth of application of wearable flexible electronics is huge, ranging from human wearable watches and clothing to sensors used in automobiles [33].

As such, a number of research efforts are directed towards the fabrication, design, and synthesis of solid-state flexible supercapacitors [34, 63, 64]. The asymmetric design of supercapacitor is beneficial in extending the potential window by employing one electrode for Faradic reactions, and the other as a capacitor for improved power density. Furthermore, various combinations of electrodes and electrolytes are used in different designs with varied level of success in terms of obtained specific capacitance, energy density, power density, capacity retention, and coulombic efficiency. Nevertheless, most of these works use materials and processes which are relatively expensive and cumbersome which pose challenges for scalability and mass production. Moreover, there is a gigantic problem of unsafe electric wastes which keeps mounting and has become a key cause of concern in recent times. For instance, the increasing use of nanoparticles in these electronic devices poses the problem of environment degradability and bioaccumulation in flora and fauna of the ecosystem they are disposed into. Accordingly, there is a high need to invest and encourage bio-friendly technologies which employ materials which are from green sources and easily bio-degradable.

Transition metal oxides like MnO_2, ZnO, CoO, NiO, RuO_2, and CuO are highly sought candidates to be used in combination with other electroactive materials like carbon, carbon nanotubes (CNTs), carbon fibers, carbon nanospheres due to their ability to enhance charge transport [46, 47, 65, 66]. This leads to higher specific capacitance compared to the conventional electric double-layer capacitor (EDLC) on account of enhanced interfacial Faradic reactions. MnO_2, in particular, is widely favored over others since it is not only cheaper but also readily available and safer [52, 53]. MnO_2 has different crystal structures like α-MnO_2, γ-MnO_2 and has a high theoretical specific capacitance of 1370 Fg^{-1}. These have been investigated in detail for their structures which have different electrochemical properties [54, 55]. Accordingly, a wide variety of processes are available for obtaining a particular crystal form of MnO_2 [52, 56-58, 67-71]. A major drawback of MnO_2 is its poor electrical conductivity (10^{-5} – 10^{-6} S cm^{-1}), which poses a limitation on the bulk utilization of MnO_2 [50]. To overcome this drawback, the approach is to incorporate nanostructured MnO_2 into carbonaceous materials. This provides high electroactive surface area and reliable electrical connection for the maximum utilization of MnO_2.

Of late, several carbon-based materials are used as supercapacitor electroactive material. Some examples include graphene, graphite, activated carbon, carbon nanotubes (CNTs), carbon hollow spheres and carbon fibers [72, 73]. Lignin is naturally found in plants in abundance. It is also a waste product of the paper and pulp industry [74]. Chemically, lignin is a non-toxic, polyaromatic polyol, and a relatively inexpensive sustainable polymer [75]. Of late, carbon fibers have been produced with lignin since it is more advantageous compared to PAN and pitch [76]. It has a high carbon content (60%) and abundant presence of phenyl propane [75]. One notable disadvantage of lignin, however, is its poor mechanical property. It is also a cumbersome task to recover lignin in a pure and clean form [77].

To try and overcome the drawbacks posed by lignin and MnO_2, a new material was synthesized, with major requirements of flexibility, cost-effectiveness and ease of manufacturing being kept in mind. When combined with AC, structural instability and poor mechanical properties of lignin can be overcome to a certain extent. Decoration of MnO_2 ions on this AC/lignin matrix was done to increase the electroactive surface area, and in turn, increase the electrochemical conductivity of the material. In this study, we fabricated, assembled, and tested a solid-state, plant-based flexible supercapacitor for applications in flexible electronics. The supercapacitor is ultra- lightweight, cheap, and made with the simple and inexpensive fabrication process. Our asymmetric supercapacitor is made up of MnO_2 decorated activated carbon (AC) and Lignin (lig) as the active material. With Al/AC/lig-MnO_2 as the anode and Al/AC as the cathode, the flexible supercapacitor was assembled using PVA/H_3PO_4 gel-based electrolyte. A series of composition of AC:lignin:MnO_2 were tested to arrive at the optimal proportions of these constituents for best electrochemical performance. The details of fabrication and assembly are provided in the experiment section. SEM characterization was done to observe the electrode and electrolyte surface and the supercapacitor interface. Additionally, a high-resolution synchrotron tomography imaging of the AC and lignin-based electrode was done to obtain microscopic details of the particle morphology. Electrochemical performance was assessed using cyclic charge-discharge (CCD), cyclic voltammetry (CV), and Electrochemical Impedance Spectroscopy (EIS). Further details of the electrochemical experiment set up are covered in the experimental section. The result and discussion section covers in detail the findings of all characterization results and electrochemical analysis. Electrochemical study through cyclic charge discharge shows that for 2000 cycles, the maximum areal specific capacitance obtained at 6.01 mA g^{-1} is 5.52 mF cm^{-2}, which is up to 13 times higher than reported as shown in Table 2. Retention was 98.7 % after 1000 cycles and 97.5 % after 2000 cycles. The maximum energy and power densities obtained were 14.11 Wh kg^{-1} and about 1 kW kg^{-1} respectively. A high coulombic efficiency of 98 % was obtained after 2000 cycles. Due to the synergistic effect of activated carbon, lignin, and MnO_2, the fabricated AC/lig-MnO_2 supercapacitor has superior performance than reported. Such electrochemical performance of this supercapacitor makes it useful for a wide variety of device applications which employ flexible supercapacitors.

3.2 Experimental Section

Preparation of Al/AC/lignin-MnO_2 Composite Electrode

Four different samples of the Al/AC/lignin-MnO_2 composite electrodes were prepared differing in the relative weight fraction of each component. The samples were named as x:x:y, x:2x:y, 2x:x:2y, and Orig 2x:x:y as per the proportion of AC:ligin:MnO_2 where x = 0.5 g, y = 47.5µmol MnO_2 concentration. For instance, the sample Orig 2x:x:y contained 1 g of AC, 0.5 g of lignin and 47.5 µmol concentration of MnO_2. To prepare the Orig 2x:x:y first, a $KMnO_4$ solution of 47.5µmol was made by adding 0.0003 g of $KMnO_4$ powder (Sigma Aldrich, MW=158.03 gmol^{-1}, size <150 µm) in 50 ml of distilled water. Then 0.5 g of alkaline lignin powder (TCI) and 1 g activated carbon (Sigma Aldrich, MW=12.01 gmol^{-1}) were mixed by weight to obtain a mixture of AC and lignin. This powder mixture was then taken in an autoclave with a Teflon liner, and 50 ml of $KMnO_4$ solution prepared earlier was added to it. Hydrothermal treatment was carried out at 160^0 C for 1 hour. The resultant solution was allowed to cool down at room temperature. The excess liquid was drained, and the slurry was dried in a vacuum oven overnight at 50^{0}C. The powder obtained was mixed with PVDF (Sigma Aldrich, MW = 180,000 by GPC) in the ratio 4:1, and 2 ml of NMP (Sigma. Aldrich, density = 1.028 gml^{-1}, MW= 99.13 gmol^{-1}, > 99 % pure) was added to the slurry. The slurry was coated on an aluminum foil (0.98 mm thick) substrate cut in the form of a circular plate of diameter 4 cm. The adjoining strips of the foil were 1 cm wide and 3 cm long. This design enables flexibility to the supercapacitor since the adjoining Al strip can be flexibly used over a 360^0 angle for electrical connections. The coated foil was heated in a vacuum oven for 4 hours at 100°C to obtain the Al/AC/lignin-MnO_2 composite electrode. Similar procedure was done to prepare the electrodes samples for x:x:y, x:2x:y, and 2x:x:2y by varying the relative compositions of AC, lignin, and MnO_2. Fig. 3.1 shows the general schematic of the process. The mass distribution in the composite electrode were: 0.41µg MnO_2 and 0.045g lignin.

Preparation of PVA/H_3PO_4 Gel Electrolyte

A non-aqueous gel made up of PVA/H_3PO_4 was prepared. To make this gel, 1g of PVA (Aldrich, MW=85,000 – 124,000, > 99 % pure) was added to 10 ml water. The resultant mixture was stirred over a magnetic heater at 80°C for 40 mins. After this, 08.g H_3PO_4 (Sigma Aldrich, MW = 82.0 $gmol^{-1}$) was added to the resultant solution. This was followed by stirring the solution over a magnetic heater at 70°C for 20 mins. Once the required consistency of the resulting gel was obtained, a commercial paper, of the same dimension as the electrode, was dipped in it and used as a separator for the supercapacitor.

Fabrication of Solid-state Asymmetric Supercapacitor

To fabricate the supercapacitor, the electrodes made earlier were used. The Al/AC/lignin-MnO_2 composite electrode was used as the positive electrode and Al/AC was used as the negative electrode. The two electrodes were sandwiched with the gel electrolyte in between.

Materials Characterization

Scanning electron microscope

Scanning electron microscope (SEM) characterization was carried out to study the surface characteristics of the electrodes, the gel electrolyte, and the supercapacitor interface. For this, the

VEGA/TESCAN model SEM, at the Texas A&M Mechanical Engineering Facility, was used. It employed an electron beam accelerated at 5 kV and provided a magnification of 100x.

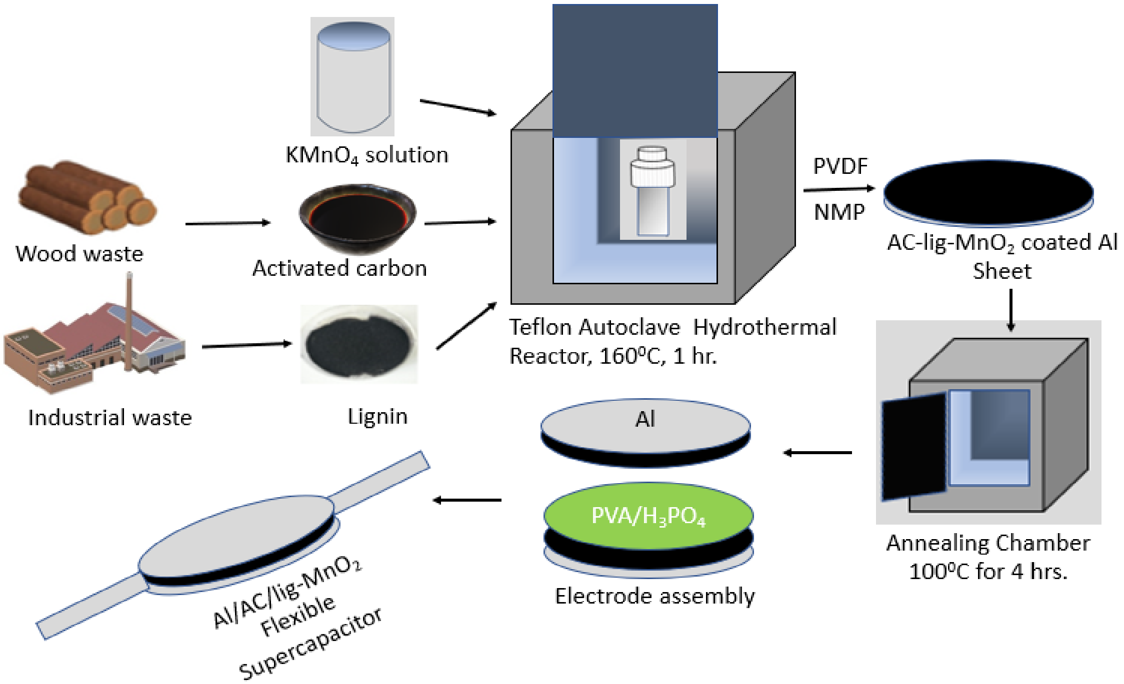

Fig. 3.1 Schematic diagram of the fabrication process and assembly of the Al/AC/lig-MnO_2 supercapacitor. Electrode dimensions: diameter = 4 cm, width of Al strip =1 cm, and length of Al strip = 3 cm.

X-ray diffraction

For XRD of AC and lignin particles of the composite supercapacitor electrode, a 2.2 kW Cu X-ray tube was used as the X-ray source. The tube was maintained at 40 kV and 25 mA. For the X-ray optics, the standard Bragg-Brentano para-focusing mode was employed. A radiation safety enclosure contained the sample holder having two circular goniometers. For data collection, an automated COMMANDER program was used. EVA software was used for data analysis.

FTIR spectroscopy

Fourier Transform InfraRed (FTIR) spectroscopy was performed for the AC and lignin particles of the composite supercapacitor electrode to identify the chemical identity of the particles. A Shimadzu IRAffinity-1 spectrophotometer was used to record the FTIR spectra. The powdered samples were placed on the instrument disc and the wavenumber range used ranged from 4000 to 500 cm^{-1} with a resolution of 500 cm^{-1}.

UV-vis spectroscopy

UV-vis spectra was performed for the MnO_2 particles of the composite supercapacitor electrode. For this, distilled water was used as a reference. 47.5 µmol of $KMnO_4$ solution hydrothermally treated was used. Thermal decomposition of $KMnO_4$ lead to the formation of MnO_2 which shows characteristic spectra under UV. Shimadzu UV-2550 spectrophotometer was used to record the UV-vis spectra.

Synchrotron X-ray tomography

To get detailed information about the electrode morphology, structure, and interface of the supercapacitor, high-resolution synchrotron X-ray tomography was carried out at beamline 8.3.2 at the Lawrence Berkeley National Laboratory at its Advanced Light Source (ALS) facility. This technique presents the advantage of being a non-destructive tool for viewing the inner layers of electrode samples. Analysis of the image data also allows the study of the dependence of electrochemical behavior on surface morphology. Experimentally, 35 KeV X-rays were used, and 360-1800 images were collected while the sample was rotated over 180 degrees. Detection was accomplished with 50 uM Ce: LuAG scintillator, a Mitutoyo 5X lens, and a PCO edge sCMOS camera for a resolution of about 1.3 microns. Xi-CAM and TomoPy software packages were used to reconstruct the volumes [69]. 3D visualization was done using Avizo and FIJI software packages. Each of the sample scans took about 45 minutes to complete. The 2D images were concatenated and contrast enhancement was performed using imageJ [70].

Electrochemical measurements

A Gamry potentiostat version 6.33 was used to perform the electrochemical characterization. For the cyclic voltammetry (CV) experiment, the MnO_2 based electrode of the supercapacitor was used as the working (positive) electrode, and the reference and counter electrode terminals were connected to the AC based electrode of the supercapacitor. To assess the effect of scan rate voltage on the electrochemical performance of the supercapacitor, CV experiment was performed at various scan rates i.e., at 5, 10, 25, and 100 mVs^{-1}. The voltage range for CV was 1-2V and the optimal scan rate was 10 mVs^{-1}. The comparative CV plots are shown in Fig. 3.8. In order to get a detailed understanding of the supercapacitor impedance behavior, electrochemical impedance spectroscopy was also carried out using a frequency range of 10^6 Hz to 0.1 Hz, AC volts of 10 mv and DC at 1 V. The selected frequency range was wisely selected so that all crucial steps namely ion-transfer resistance in the electrolyte, charge transfer resistance in the capacitive double layer, which is high frequency dependent phenomena, are covered along with the low-frequency dependent diffusion kinetics in the electrode. AC volts and DC volts were selected as per EIS guidelines in the Gamry instrument framework applicable for mass transfer and diffusion related process. Nyquist plots were obtained at regular intervals starting at the beginning, and after the end of the 100th, 350th, 1000th, 1300th and 2000th cycle. The results are shown in Fig. 3.10. The cyclic charge-discharge (CCD) experiment was carried out at a current density of 6.01 mAg^{-1} using a Gamry potentiostat. One minute duration was provided each for a charge and discharge cycle. CCD experiment was run for 2000 cycles with the upper limit of voltage being 20 V.

3.3 Results and discussion

Morphology of the samples was studied using SEM. It was used to observe the electrode-electrolyte interface and surface features. Fig. 3.2a shows the SEM images of the PVA/H_3PO_4 based gel electrolyte used in the supercapacitor interface. We see that the surface of the electrolyte appears to be smooth and without any damage. This smooth electrolyte surface ensures there is good interfacial contact with the electrode surface and no unwanted reaction products are generated due to undesirable side reactions due to any impurity. In Fig. 3.2b we see the negative electrode surface showing AC particles. The AC particles are seen evenly distributed throughout the electrode surface. The substrate used was Al foil. An even distribution of AC particles ensures better attachment and higher contact area with the electrolyte. The particles appear clustered in some local regions and elongated. There are also seen regions with high porosity as shown in the yellow rectangle in Fig. 2b. The highly porous structure is helpful for higher contact area for surface reaction.

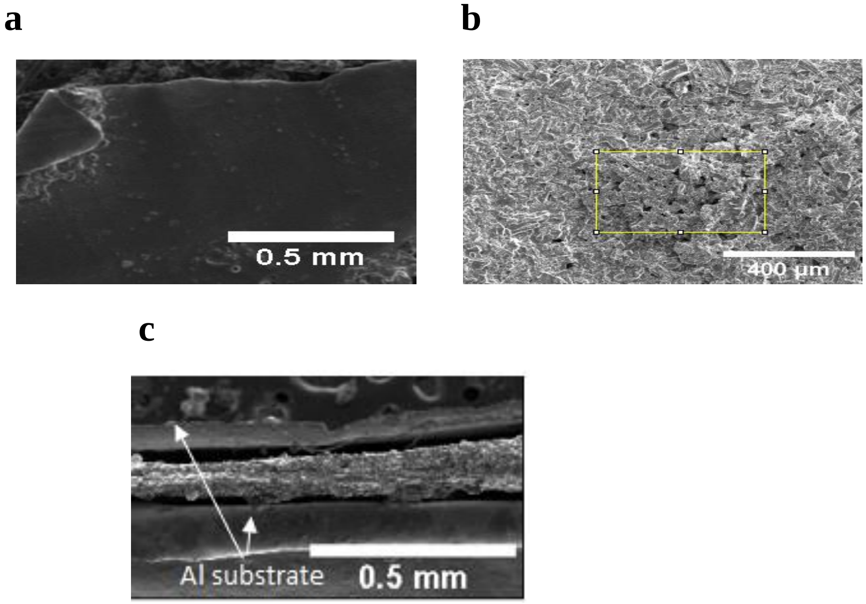

Fig. 3.2 High-resolution Scanning Electron Microscope image of (a) the PVA/H_3PO_4 gel electrolyte; scale bar =0.5 mm, (b) the AC coated electrode, scale bar =400 µm, and (c) supercapacitor interface showing gel electrolyte sandwiched between electrodes with outer Al current collector layer, scale bar =0.5 mm.

Fig. 3.2c shows the supercapacitor interface. The electrolyte gel layer is sandwiched between the outer electrodes with Al as the substrate. The interface thickness is close to 100 microns. The active material of the electrodes seems well attached to the electrolyte layer. The interface is mechanically stable, and the two electrode surfaces are congruent with the electrolyte. This provides a good condition for the electrochemical experiment.

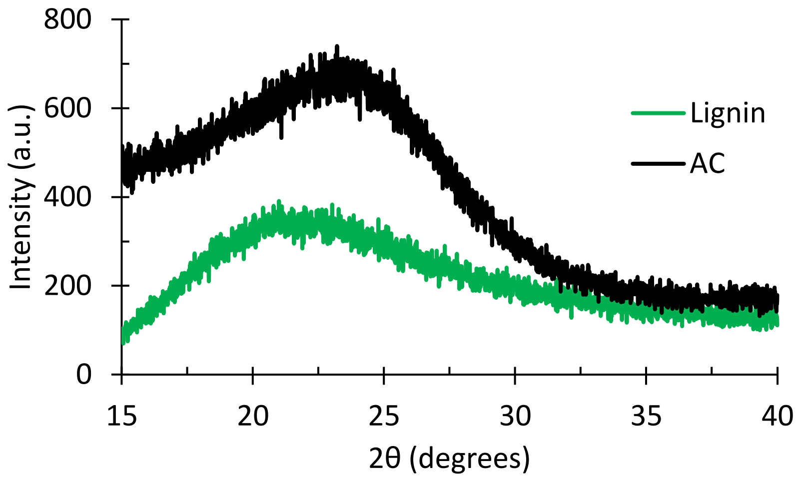

Fig. 3.3 XRD of AC and lignin particles of the composite electrode.

XRD plot for AC (Fig. 3.3) shows broad diffraction peak (002) in the range 2θ = 15-30^0. This is indicative of the amorphous nature of AC particles [78, 79]. Lignin similarly showed a broad peak in the range 2θ = 20-25^0 indicating at its highly amorphous nature [79]. The relative lower intensity in lignin peaks compared to that of AC shows greater departure from crystallinity in lignin particles.

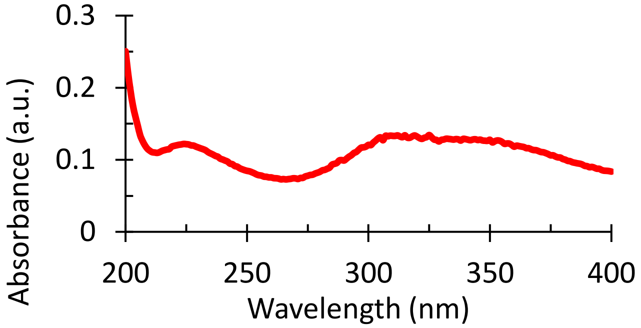

Fig. 3.4 UV-vis spectra of MnO_2.

From the UV-vis plot (Fig. 3.4) a characteristic broad peak in the range 300 – 380 nm confirmed the presence of MnO_2 [80]. At high temperature, thermal decomposition occurs for $KMnO_4$ which leads to peak at about 380 nm indicative of the d-d transition in Mn^{4+} ions indicating the formation of sheet like structure for MnO_2 [81].

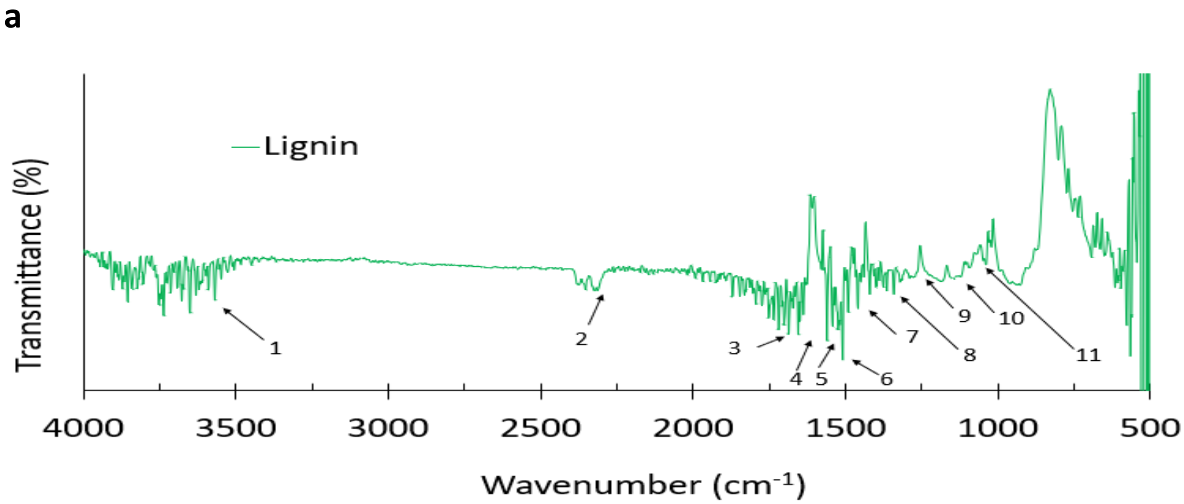

b

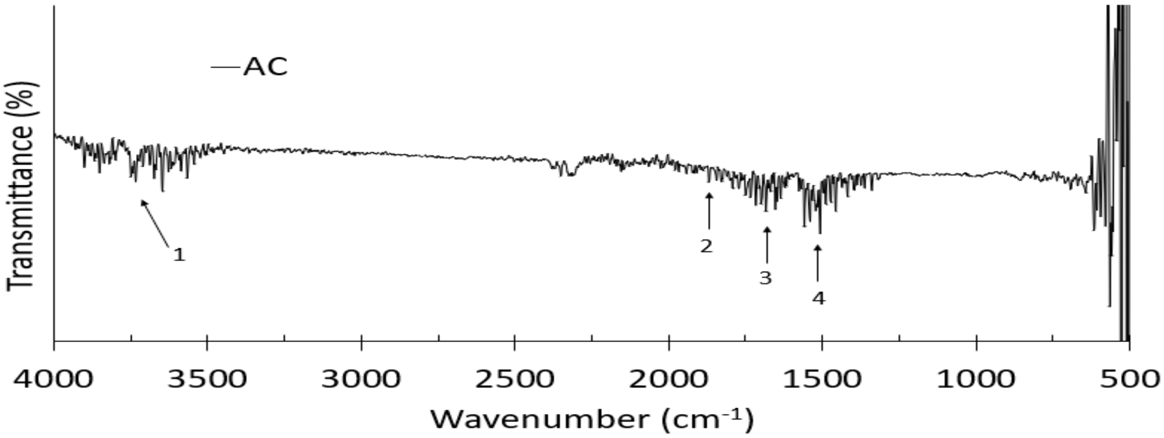

Fig. 3.5 FTIR spectra for the composite electrode materials: (a) lignin and (b) AC.

FTIR analysis was carried out for lignin and AC to ascertain the chemical signature of the molecules present. The peaks were compared to the literature reports for both lignin and AC [82-84]. In FTIR plot of lignin (Fig. 3.5a), the peaks corresponding to 3400-3750 cm^{-1} (peak 1) can be attributed to the O-H bond stretching. C-H bond stretch vibration of methylene and methyl groups correspond to 2310-2350 cm^{-1} (peak 2). C=O stretching in unconjugated carbonyls correspond to the peaks in the range 1705-1724 cm^{-1} (peak 3). Peak 4 at 1635 cm^{-1} signify C=O group stretching in α, β unsaturated aldehydes or ketones and C=C groups in alkanes. Peaks in the range1500-1585 cm^{-1} (peak 5) can be attributed to C-C bond stretch vibration in aromatic rings. Peak 6 at 1506 cm^{-1} correspond to the benzene ring skeleton stretching vibration which is the characteristic absorption peak for lignin. Peak 7 at 1456 cm^{-1} represents the C-H bending vibration in methyl groups. The peak appearing at 1338 cm^{-1} (peak 8) correspond to the rock or bend vibration in alkanes. In lignin it also corresponds to the C-O stretch in the syringol ring breathing mode. Peak 9, 10 and 11 at 1271 cm^{-1}, 1141 cm^{-1}, 1035 cm^{-1}, correspond to C-O stretching vibration in guaiacol rings, C-H vibration stretching in guaiacol rings, and C-O stretch in C-O in ether or alcohol. For FTIR plot of AC (Fig. 3.5b), peak 1 corresponding to 3734 cm^{-1} represents O-H bond stretching. The vibration absorption (non-symmetric) of C=O corresponds to the peak at 1843 cm^{-1} (peak 2). For the range 1635 – 1772 cm^{-1} (peak 3) the stretching vibration absorption of C=O is represented. The stretching vibration of the skeleton of the benzene ring is attributed to peak 4 occurring in the range 1506- 1558 cm^{-1}. The corresponding high intensity for benzene skeleton in lignin signifies that the benzene structure in lignin is on an average more intact.

To understand the morphology of particles of the AC/lignin matrix, it is simpler to first analyze them in separate set up. Corresponding to this, two separate fresh samples of supercapacitors were assembled for experimenting; one made up of AC, and the other made up of lignin.

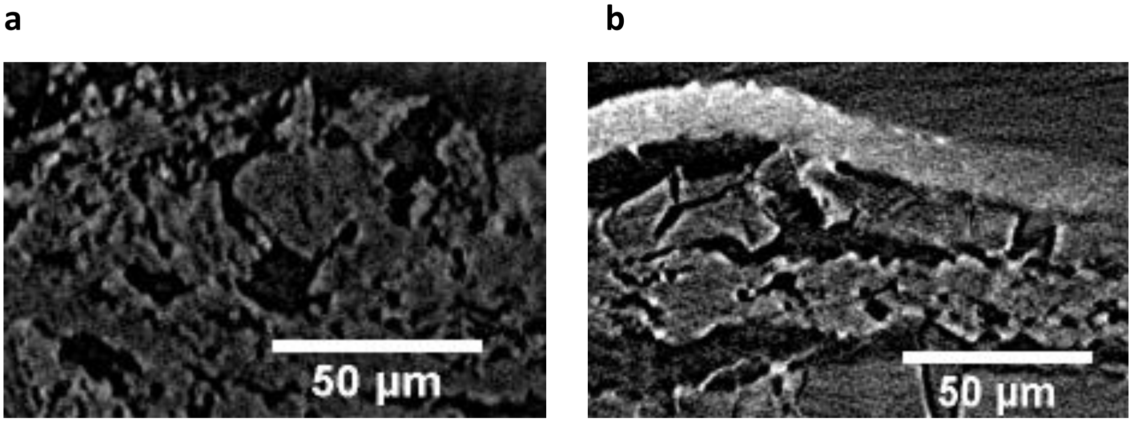

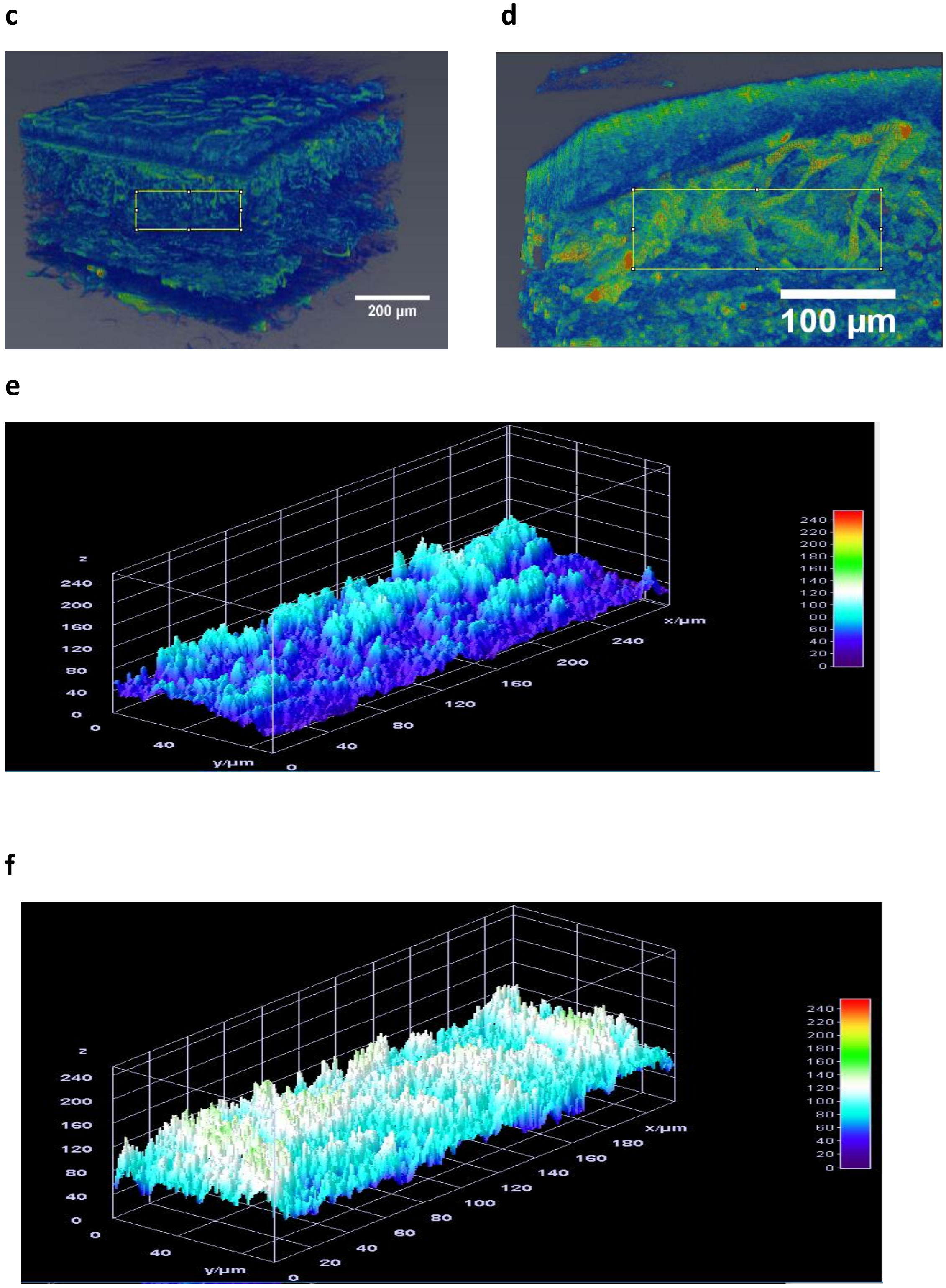
c
d
200 µm
100 µm
e
z
240
200
160
120
80
40
0
0
40
y/µm
0
40
80
120
160
200
240
x/µm
240
220
200
180
160
140
120
100
80
60
40
20
0
f
z
240
200
160
120
80
40
0
0
40
y/µm
0
20
40
60
80
100
120
140
160
180
x/µm
240
220
200
180
160
140
120
100
80
60
40
20
0

g

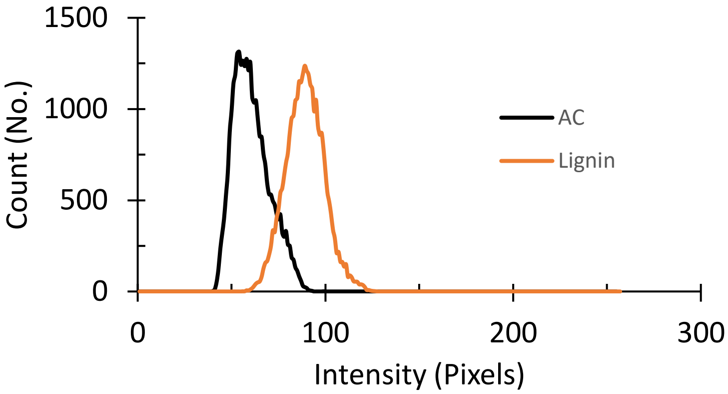

Fig. 3.6 High resolution synchrotron X-ray tomographic image of (a) the AC particles, (b) the Lignin particles, (c) the AC supercapacitor (scale bar = 200 µm), and (d) lignin supercapacitor (scale bar = 100 µm). Yellow rectangle section of dimension 200 × 100 µm is shown in both (c) and (d). X-axis direction is the horizontal line (width) and Y-axis direction is the vertical line (height). 3D interactive surface plot of (e) AC supercapacitor; numbers on the color bar in the right refer to pixel value, (f) lignin supercapacitor, and (g) the comparative histogram plot of count of particles (Y-axis) versus intensity (pixels) for the AC and lignin-based supercapacitors shown in (c) and (d).

Synchrotron tomography was used to observe the composite electrode particles: AC (Fig. 3.6a) and lignin (Fig. 3.6b). As seen from Fig. 3.6a, the AC particles appear in agglomerated clusters with apparently higher number of surface pores than that of lignin (Fig. 3.6b). It also appears the AC particle apparent length is smaller than lignin particles (Fig. 3.6b) which is due to smaller carbon chain linkages in AC as a consequence of the activation process. The lignin material (Fig. 3.6b) has longer particle strands which seems to overlap on each other in a three dimensional set up. Both AC and lignin have amorphous nature with 3D branching of chains and presence of surface voids. There are evidence of localized agglomerations in AC diameter 5-50 µm approximately. The lignin strand lengths as apparent from Fig. 3.6b ranges from 5-150 µm in length. Since, both AC and lignin particles have complex branching in 3D space, it is more reasonable to further observe the 3D features of the electrodes using 3D tomography and image analysis. High-resolution synchrotron X-ray tomography was done to assess the initial morphology of particles of these two supercapacitors. Fig. 3.6c shows the morphology of activated carbon (AC) based supercapacitor, and Fig. 3.6d shows the morphology of lignin-based supercapacitor. The analysis is performed using imageJ. Both in Fig. 3.6c and 6d, a similar 200 × 100 µm rectangular section marked in yellow within the 3D images, is used for detailed morphology study of particles. Specific points of interest include the shape, size, and circularity of the particles; surface packing density, measures of central tendencies, and particle distribution. These values are tabulated in Table 3.

Fig. 3.6e and 3.6f show the interactive 3D surface plots of intensity across the rectangular section. This is done to obtain a visual inspection of the relative surface distribution of particles in both the supercapacitors. The intensity in the 3D plots is indicative of the nature of the particles in the two supercapacitors which directly relate to types of functional groups and bonds present. All of the peaks across the x-y plane in Fig. 3.6e lie below the 120-pixel line. In Fig. 3.6f, all of the peaks across the x-y plane lie below the 160-pixel line. As such, we see a corresponding higher average intensity in the lignin plot (Fig. 3.6f) than that of AC plot (Fig. 3.6e).

The circularity of particles represented by Circ. in Table 3 represents the closeness of the particles to a circle. A value of 1 represents a perfect circle while a value closer to 0.0 represents an increasing elongated shape. In general, the below equation represents circularity (Circ.).

$$Circ. = 4 \times \frac{[Area]}{[Perimeter]^2} \quad (1)$$

Table 3. Particle morphological measurements obtained from the tomography image for the AC and lignin-based supercapacitors (SC).

Parameter	AC SC	Lignin SC
Mean	60.62	87.13
StdDev	9.62	10.17
Min	40	54
Max	99	125
Circ.	0.68	0.59
IntDen	1,606,997	1,874,122
Skew	0.59	0.09
Kurt	-0.39	0.48
AR	3	NaN
Round	0.333	Infinity

The smaller value of circularity of lignin particles (Circ. = 0.59), as seen from Table 3, indicates that the particles of lignin are more elongated in general compared to that of AC (Circ. = 0.68). This could be due to more complex and elongated polymeric chains in lignin molecules.

Fig. 3.6g shows the plot of pixel counts versus the intensity of the pixels for AC (black) based and lignin (orange) based supercapacitors. It can be seen that the peak of the lignin curve occurs at 87 pixels while that of the AC curve occurs at 59 pixels. The mean of the AC curve as seen from Table 3 is 60.62 while that of lignin curve is 87.13 pixels. This implies that on average lignin has a higher intensity which is proportional to the number of functional groups present in lignin with comparatively higher values of K-edge as compared to AC. Also, from Table 3, AC based supercapacitor has both minimum (40 pixels) and maximum (99 pixels) values of intensities lower than that of the lignin-based supercapacitor with corresponding values of 54 and 125 pixels respectively. The right-shifted the curve of the lignin in Fig. 3.6g also indicates this. This is evidence of lignin particles providing higher resistance to the penetrating x-rays compared to AC particles. This is expected because of more elongated and complex nature of lignin polymer chains as compared to that of AC molecules. This fact is also reiterated by the value of the aspect ratio (AR) which is the ratio of major to the minor axis when the particles are fit with an elliptical shape. The AR values from Table 3 for AC and lignin particles are 3 and an extremely small number (NaN) respectively. Thus, a very low value of AR for lignin particles suggest that the particles are very wide or elongated compared to their length i.e., the minor axis is long, and the major axis is minuscule compared to it. This is also seen from the value of Round parameter, which is the inverse of AR in Table 3. Integrated density (IntDen) in Table 3 shows the sum of total pixels in the plots of AC and lignin. A higher value of IntDen is indicative of higher surface packing density of molecules. It is seen from Table 3 that the IntDen value of lignin (187,4122) is higher that of AC (160,6997) by a factor of 16.6 %. Thus, there is more surface mass distribution in the lignin supercapacitor. A positive value of the skewness (skew) parameter indicates that the curve has a tail extending to the right of the center of mass. As seen from Table 3, a higher value of skew for AC (0.59) means it has a longer tail than that of lignin (0.09). Thus, lignin-based supercapacitor has a distribution which is closer to Gaussian distribution than the AC based supercapacitor. Hence, the lignin-based supercapacitor is a better Gaussian surface. This is also seen from a negative value of kurtosis (Kurt) for the AC based supercapacitor. The negative value suggests at a more flatter surface. A positive value of Kurt for the lignin-based supercapacitor is indicative of more peaked distribution. Hence, it can be argued that on an average, the lignin-based supercapacitor has a surface which is rougher than that of the AC based supercapacitor. Higher surface packing density is required for achieving a higher energy density of the supercapacitor while low surface roughness helps in better interfacial contact for improved charge transport. Thus, we observed that using lignin and AC combination in the AC/lig-MnO_2 supercapacitor has a distinct advantage of the higher surface packing density of lignin and low surface roughness of AC. The elongated shape of the lignin fibers imparts added advantage of the reduction in a surface void fraction which further reduces internal resistance to ion transport within the active material.

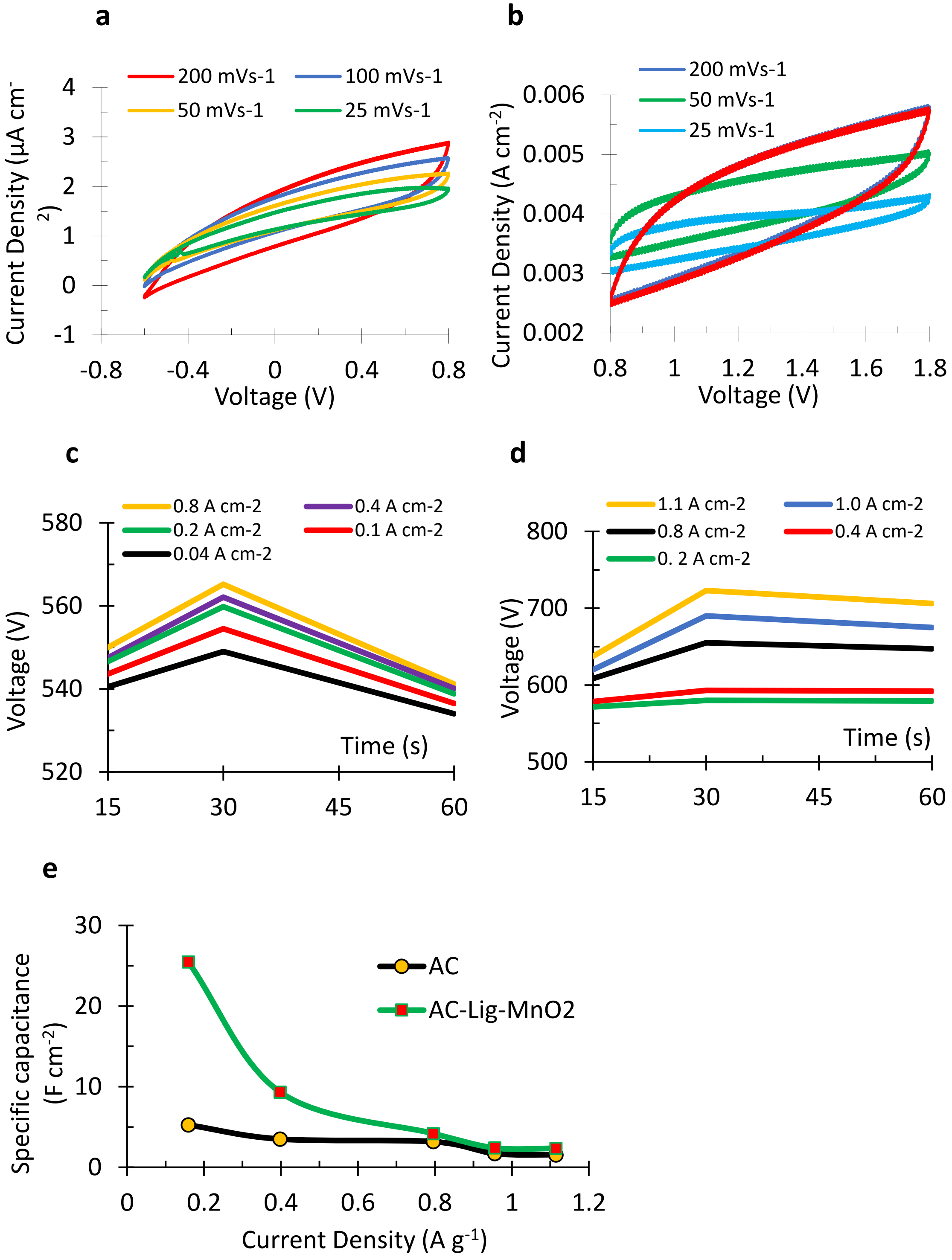

Fig. 3.7 Three electrode tests for the AC and AC/lig-MnO$_2$ electrodes: CV plots for the AC (a) and AC/lig-MnO$_2$ (b) electrodes at varying scan rates. Voltage versus time plots

for the AC (c) and AC/lig-MnO_2 (d) electrodes at varying current densities, and (e) the specific capacitance versus current density plots for the AC and AC/lig-MnO_2 electrodes.

For the three electrode test, the reference electrode used was Ag(s)/AgCl (aq.) and the counter electrode was graphite rod. For the working electrode, either the AC based electrode or the composite AC/lignin-MnO_2 electrode was used in a three electrode electrochemical test set up using H_3PO_4 (85 wt. %) electrolyte. Results are shown in Fig. 3.7. The optimal working electrode potential range for the AC electrode was in the range -0.6 to 0.8 V (Fig. 3.7a). The CV curves showed good cyclability at various scan rates tested (25, 50, 100, and 200 mVs^{-1}). For the composite working electrode i.e. AC/lignin-MnO_2, the optimal potential window was 0.8- 1.8 V (Fig. 3.7b) and it showed good cycle performance for the scan rates tested (25, 50, 100, and 200 mVs^{-1}). Discharge voltage versus time plot for AC electrode (Fig. 3.7c) showed steeper slope for the voltage decline at higher current density. The same was observed for the AC/lignin-MnO_2 electrode (Fig. 3.7d) though the rate of voltage decline was comparatively less steep than that of the AC electrode. Specific capacitance versus current density plot (Fig. 3.7e) showed the tendency of each electrode specific capacity to fall at higher current densities. The corresponding value of specific capacitance at any current density for the composite AC/lignin-MnO_2 electrode was higher than that of the AC electrode. These results suggested to use the AC electrode as the negative electrode and the composite AC/lignin-MnO_2 electrode as the positive electrode when testing for the electrochemical performance of the supercapacitor in two electrode tests.

To test the electrochemical performance of the supercapacitor both cyclic voltammetry (CV) and cyclic charge-discharge (CCD) experiments were performed. In the CV experiment, we cycle the supercapacitor keeping the voltage window (1-2V) and scan rate (10mVs^{-1}) constant. In CCD experiment, we keep the current density (6.01 mAg^{-1}) constant for 2000 cycles. The results from these two experiments give a holistic picture of the electrochemical behavior of the supercapacitor.

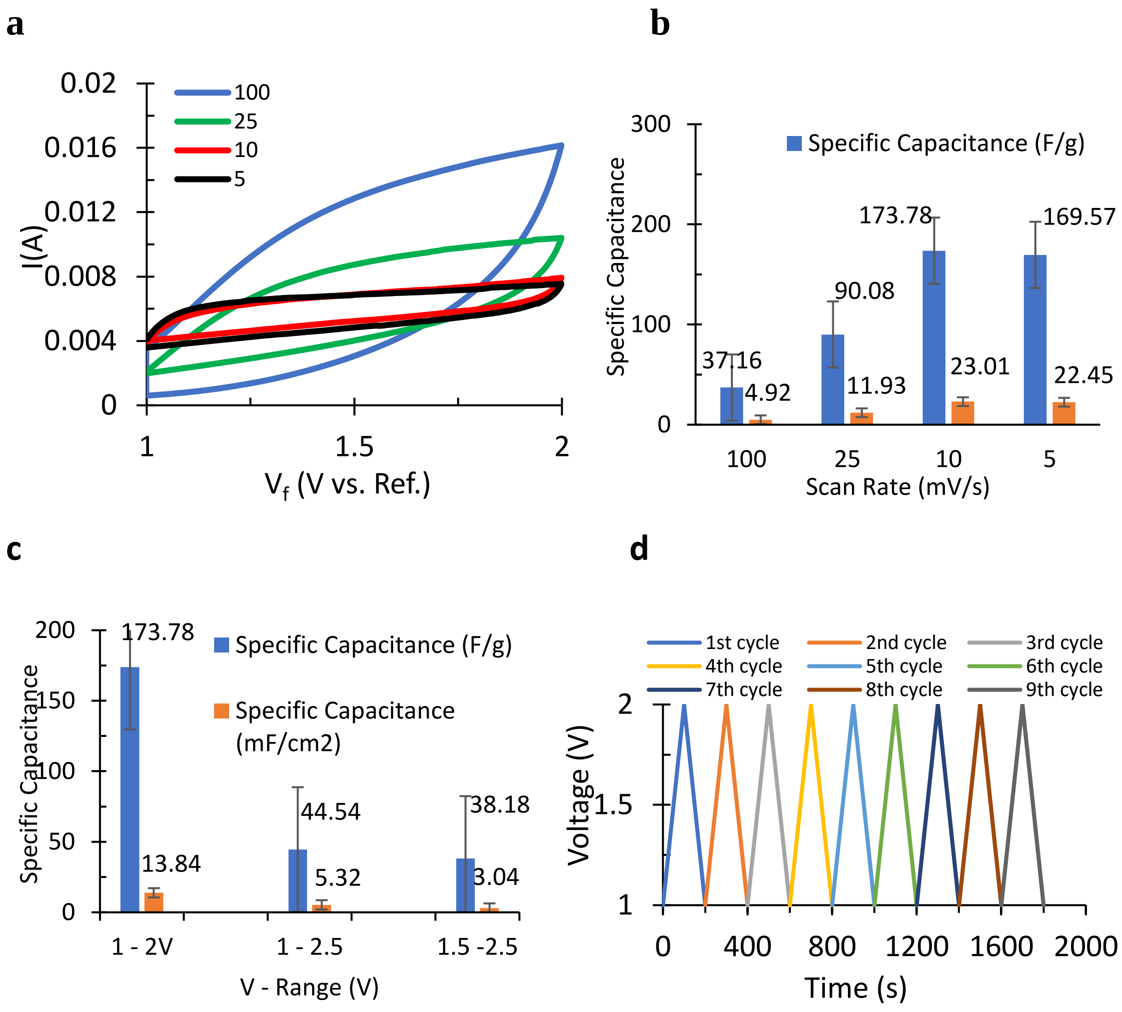

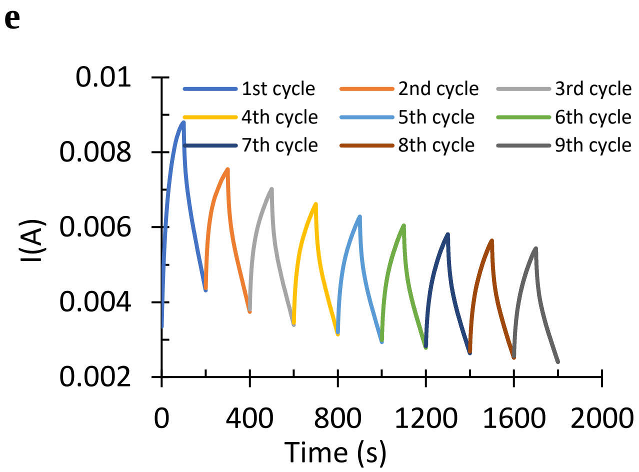

Fig. 3.8 (a) Cyclic voltammetry curve of AC/lig- MnO_2 supercapacitor at various scan rates: 5 (black), 10 (red), 25 (green), and 100 mVs^{-1} (blue); (b) comparative histogram of specific capacitance versus scan rate, (c) comparative histogram of specific capacitance versus voltage range at 10 mVs^{-1}, plots of (d) voltage vs time, and (e) current vs time from the CV experiment for the sample Orig 2x:x:y.

For comparison, the CV curves obtained at scan rates 5, 10, 25, and 100 mVs^{-1} are shown in Fig. 3.8a. The CV characteristics are better at 10 mVs^{-1} than at 5 mVs^{-1} or 100 mVs^{-1} which can be seen by a more rectangular-shaped curved at 10 mVs^{-1}. At scan rates higher than 10 mVs^{-1}, the scan voltage rate is too fast while for scan rate lower than 5 mVs^{-1}, it is too slow for a stable system dynamics. Thus, the ideal scan rate is 10 mVs^{-1} which is selected to perform the cyclic voltammetry for longer runs. This fact is also evidenced by the specific capacitance obtained at varying scan rates and shown in Fig. 3.8b. The average value of specific capacitance for the Orig 2x:x:y sample obtained at 10 mVs^{-1} is 173 F g^{-1} (23.01 mF cm^{-2}) which is the highest while that obtained at 100 mVs^{-1} is 37.16 Fg^{-1} (4.92 $mFcm^{-2}$) which is the least. It is also important to ascertain the operating voltage window for the cyclic voltammetry experiment. Fig. 3.8c shows the obtained specific capacitances at several voltage ranges for a scan rate of 10 mVs^{-1}. It is seen that we obtain the highest average specific capacitance in the voltage range of 1-2V. As part of further analysis, the voltage-time (Fig. 3.8d) and current-time (Fig. 3.8e) are shown for the first few cycles for the supercapacitor as observed in the CV experiment. The voltage variation remains constant with the cycle indicating that the voltage was varied constantly as expected to obtain the current flow in the device. Each cycle starts at a value of voltage equal to 1V, which then goes to 2V. After this, the electrode polarity is reversed, and the voltage tends to decay with a negative slope to the final value of 1V. For each cycle of voltage variation, the corresponding current is developed in the supercapacitor, which is dependent on the electroactive material, electrolyte and the design of the supercapacitor. From Fig. 3.8e we see that the current developed in each cycle follows closely the cyclical pattern of the voltage, however, the curve is not linear with respect to time, unlike the voltage. In general, the discharge part of the current, which is the current recorded after the electrode reverses its polarity for any cycle, is relatively steeper than the charging current. This means that the supercapacitor discharges more quickly than it gets charged. Also, the current in the first cycle is the highest. Current falls gradually below its highest value of the first cycle in subsequent cycles. This is expected with the gradual decay of the active material in the supercapacitor due to electrochemical reactions.

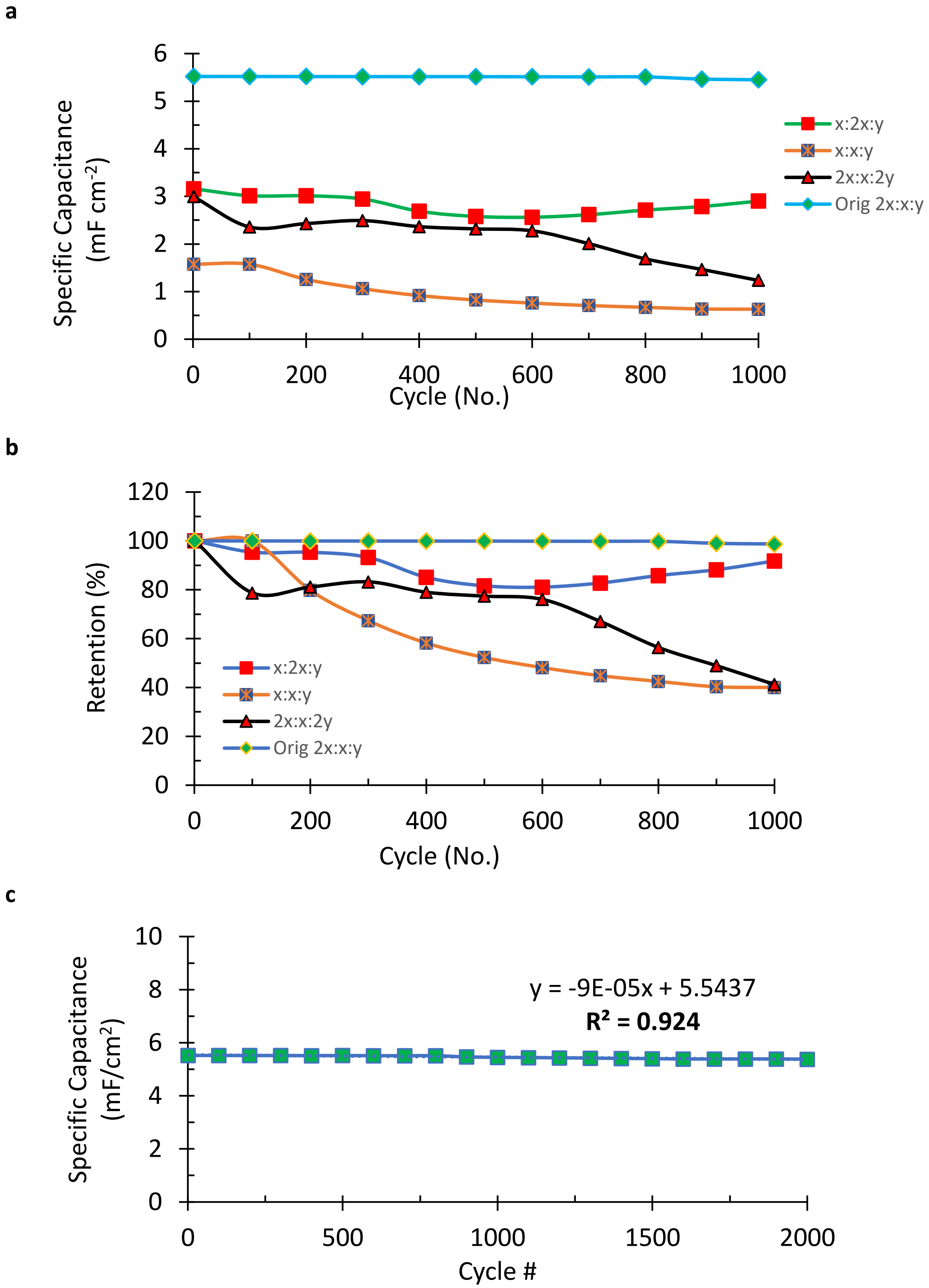

Fig. 3.9 For AC:lignin:MnO$_2$ samples named x:x:y, x:2x:y, 2x:x:2y, and Orig 2x:x:y: a) variation of specific capacitance with cycles, and b) retention; c) specific capacitance

versus cycles for sample Orig 2x:x:y for 2000 cycles for voltage range 1-2 V at 6.01 mA g^{-1}.

To assess the capacitance performance of the supercapacitors with varying AC: lig: MnO_2 proportions, cyclic charge-discharge experiment was carried out at the same current density of 6.01 mAg^{-1} for 1000 cycles each. The samples were named in the order AC:lig:MnO_2, where x = 0.5 g and y = 47.5 µmol concentration of MnO_2. For instance, x:2x:y symbolizes 0.5 g AC, 1g lignin and 47.5 µmol concentration of MnO_2. The variation of areal specific capacitance with cycles is shown in Figure 3.9a. Areal specific capacitance retention is shown in Figure 3.9b. It is seen from Figure 3.9a that the areal specific capacitance for the sample Orig 2x:x:y is the highest throughout (about 5.5 $mFcm^{-2}$) followed by the samples x:2x:y, 2x:x:y, and x:x:y in the order of the greatest to the least. As seen from Figure 3.9c, the order of the final retention also follows the order Orig 2x:x:y, x:2x:y, 2x:x:y, and x:x:y. On comparing samples x:x:y and 2x:x:y, we observe from Figure 3.9a that the latter has a higher specific capacitance and higher retention (Figure 3.9b) than the former throughout. Thus, on increasing the relative ratio of AC, the areal specific capacitance and the retention both increase. Similarly, on comparing the samples x:x:y and x:2x:y, we observe that on increasing the relative ratio of lignin, the specific capacitance increases (Figure 3.9a) and so does the retention (Figure 3.9b). However, this increase in specific capacitance and retention is lesser when AC ratio is increased. For instance, the initial areal specific capacitance for the samples x:2x:y is 3.16 mF cm^{-2} (retention = 91.77 %) as against 5.52 mF cm^{-2} (retention = 98.7 %) for the sample Orig 2x:x:y indicating that the effect of increase of

AC on the specific capacitance and retention is more pronounced than lignin. Comparing samples Orig 2x:x:y and 2x:x:2y, it is seen that increase in MnO_2 concentration has a drastic effect on the areal specific capacitance and as such there is a decrease of about 73 % in the initial value of areal specific capacitance for the 2x:x:2y (specific capacitance = 2.99 mF cm^{-2}) sample compared to the sample Orig 2x:x:y (specific capacitance = 5.52 mF cm^{-2}). Final retention for the sample 2x:x:2y is about 41 % showing that increase in MnO_2 also hampers retention. As a consequence of the above comparison, we found that the sample having the best areal specific capacitance and retention was Orig 2x:x:y. This indicated that a higher relative ratio of AC compared to lignin, and an optimal MnO_2 concentration was necessary to obtain both the highest specific capacitance and the highest retention among the samples. In accordance to this result, the best sample Orig 2x:x:y was further run at a current density of 6.01 mAg^{-1} until 2000 cycles (Figure 3.9c). A regression linear model with negative slope close to zero (-9×10^{-5}), as shown on the plot, indicates at the negligible progressive decline of the areal specific capacitance with cycles. A high value of coefficient of determination, $R^2 = 0.92$ shows good fit of the linear model with the trend of the plot. The initial areal specific capacitance is 5.52 mF cm^{-2} which remains nearly constant throughout the 2000 cycles. The final value is 5.38 mF cm^{-2}. Thus, there is only a marginal decline in the areal specific capacitance. The maximum energy density obtained for this sample was 14.11 Wh kg^{-1} and the power density was 1 kW kg^{-1}.

Table 4. Comparison of the Al/AC/lig-MnO_2 supercapacitor's electrochemical performance with literature reports

Substrate	Materials	Max. Specific Capacitance (SPC)	SPCP /SPCG†	Energy Density (Wh kg^{-1})	Power Density (Wkg^{-1})	Ref.
Al	AC-lignin-MnO_2	5.51 mF cm^{-2} at 6.01 mA g^{-1}, 2000 cycles	1	14.11	1000	This work
Ti	CNT	1.84 mF cm^{-2} at 1 mA, 1000 cycles	3.0	-	-	[73]
Carbon fabric	MnO2//MoO3	4.86 mF cm^{-2} at 0.5 mA cm-2, 3000 cycles	1.13	-	-	[74]
PET	N-Doped rGo	3.4 mF cm^{-2} at 0.5 µA cm^{-2}, 2000 cycles	1.62	-	-	[75]
PET	β-Ni(OH)2/graphene	2.57 mF cm^{-2} at 0.2 Am^{-1}, 2000 cycles	2.14	-	-	[76]
FTCF	rGO/PANI	6.4 mF cm^{-2} at 0.08 mA cm-2, 2000 cycles	0.86	7.07	707	[77]
PET	SnSe2	0.406 mF cm^{-2} at 20 mA m^{-2}, 1000 cycles	13.6	-	-	[68]

A more detailed comparison of the electrochemical performance of the fabricated AC/lig-MnO_2 supercapacitor is shown in Table 4. It is to be noted that electrochemical performance comparison for the exact same material (Al/AC/lignin-MnO_2), in this case, is not possible since it is a new material. However, some reports from literature, for supercapacitors are shown in Table 4 to present a comparison with sources cited in the last column (Ref.). It can be seen from Table 4 that the obtained specific capacitance of present work (SPCP) to the specific capacitance of reported works (SPCG) ratio varies

---

† SPCP/SPCG is the ratio of specific capacitance of present work (SPCP) and specific capacitance of the cited work (SPCG).

from 0.36 – 13.6 which is remarkable. Thus, the supercapacitor sample Orig 2x:x:y has an electrochemical performance which is not only at par with those reported but even better than many others.

Electroimpedance spectroscopy was carried out to understand the impedance behavior of the supercapacitor, and accordingly, the Nyquist plots are obtained and shown in Fig. 3.10. For the sample Orig 2x:xy, as seen from Fig. 3.10a, the total impedance after the 100th cycle (purple) is 558 ohm which is greater than 17.3 ohm, the value at the beginning (dark blue). Similarly, the impedance after the 350th cycle (dotted black) which is 593 ohm is greater than that after the 100th

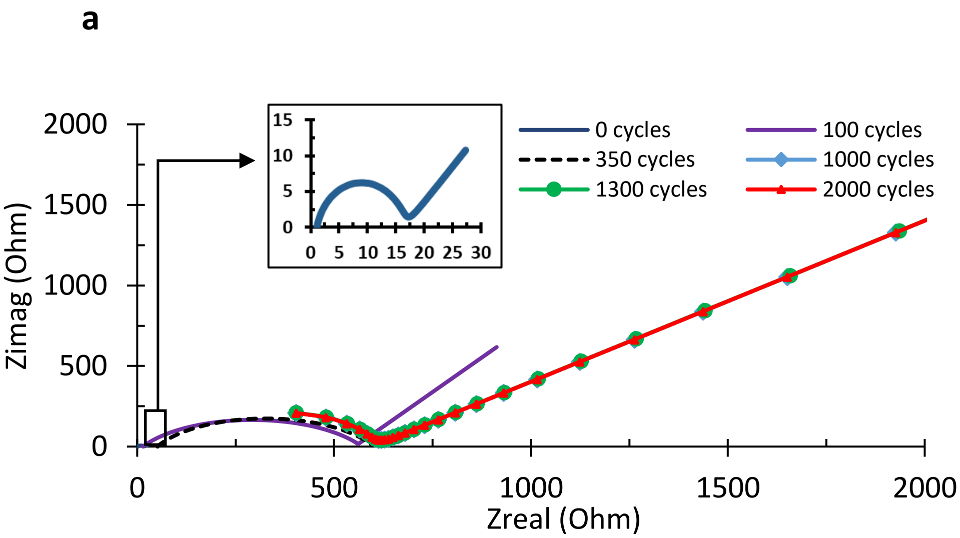

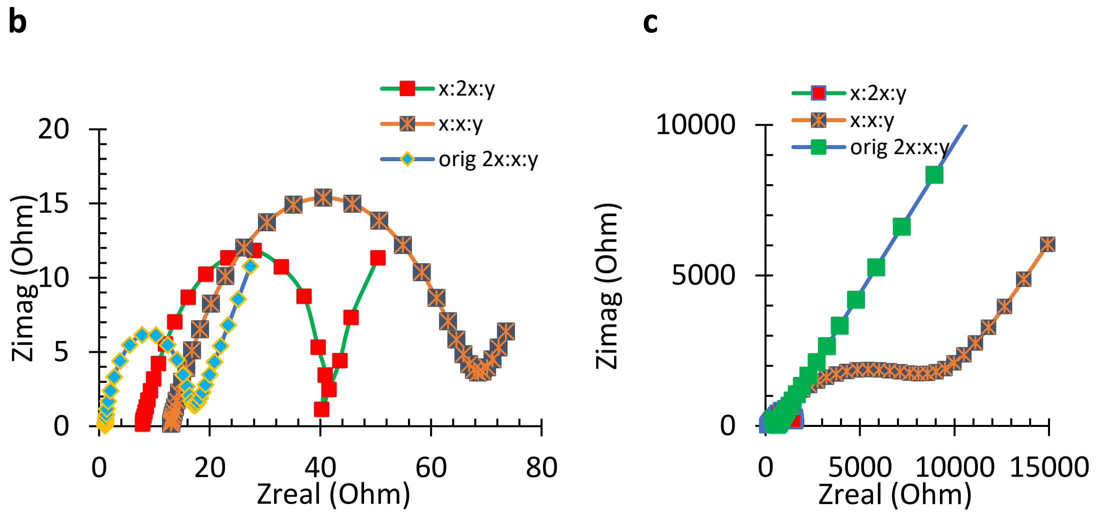

Fig. 3.10 Electrochemical impedance spectroscopy (Nyquist plots) of a) the Orig 2x:x:y sample at the beginning (dark blue), after 100th cycle (purple), 350th cycle (dotted black), 1000th cycle (light blue), 1300th cycle (green), and 2000th cycle (red). Comparative Nyquist plots for the samples x:2x:y, x:x:y, and Orig 2x:x:y at b) the beginning (1st) cycle and c) at the end (1000th cycle).

cycle. The impedance values after the 1000th, 1300th and 2000th cycles recorded were 613 ohm, 628 ohm, and 638 ohm respectively which are interestingly very close and differ only slightly. This indicates that after about 1000 cycles, the cumulative impedance of the electrolyte and the double layer capacitance hits a threshold value and the difference in current occurring is largely due to the kinetic diffusion resistance offered by the electroactive material. Nevertheless, as would be expected, the impedance values follow the trend 0th, 100th, 350th, 1000th, 1300th, and 2000th from the least to the greatest. This indicates that with the progression of cycles, the resistance to current flow increases, and hence it results in lesser current flow and lesser capacity retention towards higher cycle number. The rate at which impedance develops, however, is steeped in the beginning, i.e., from the 1st to the 350th cycle, and then declines rapidly from the 1000th to the 2000th cycle. As can be seen from Figure 3.10b, for the Orig 2x:x:y sample, the total impedance (16.7 ohm), as indicated by the intersection of the semicircle with x-axis, is the least compared to the samples x:2x:y (40.3 ohm) and x:x:y (69.3 ohm) at the beginning (1st cycle). This justifies as to why the corresponding specific capacitance is the highest for the Orig 2x:x:y sample in the beginning (Figure 3.10a) due to the least overall impedance to charge transfer in this sample compared to other samples. The corresponding impedance for the samples at the end of 1000 cycles (Figure 3.10c), follows the trend Orig 2x:x:y (613 ohm), x:2x:y (931 ohm), x:x:y (9020 ohm) from the least to the greatest. This too justifies as to why the corresponding specific capacitance is the highest for the Orig 2x:x:y sample after 1000 cycles (Figure 3.10a) due to the least overall impedance to charge transfer in this sample compared to other samples.

To observe the impact of current density on the resultant discharge voltage in the cyclic charge-discharge experiment, Fig. 3.11a is obtained. The resultant voltage curves are obtained at various current densities of 1.2 mA/g (yellow), 3.01 mA/g (purple), 6.01 mA/g (green) and 9.01 mA/g (red). The key point of interest here is the rate of decline (slope) of the discharge voltage curves at varying current densities. It is seen that the higher the current density steeper is the slope of the voltage-time curve. Thus, at higher current density the voltage drop is at a higher rate. This is expected behavior for any supercapacitor. To obtain the effect of discharge current density on

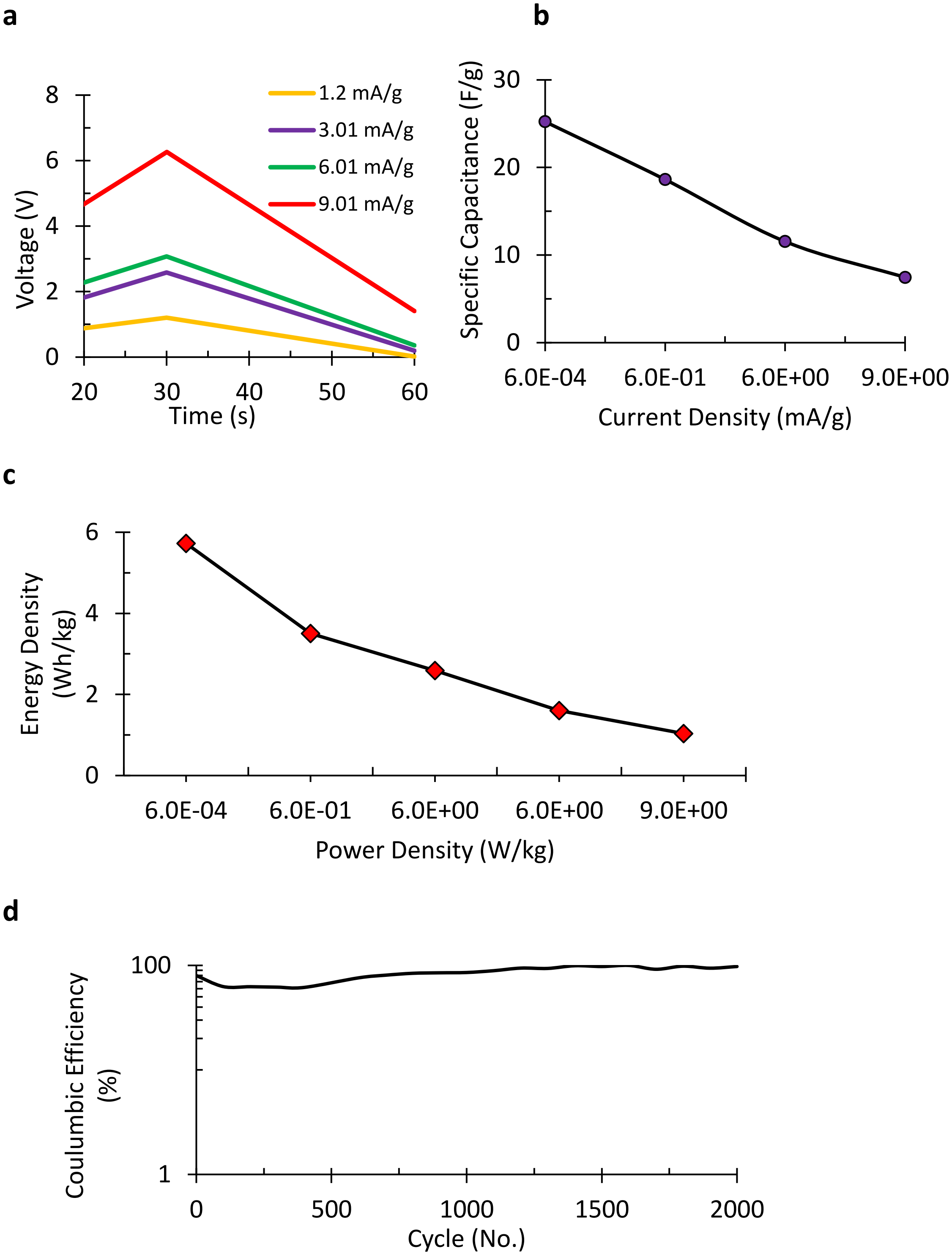

Fig. 3.11 Comparative plots of (a) voltage versus time at different current densities, and (b) specific capacitance versus current density in the cyclic charge discharge experiment

at a charge current of 2 mA. Ragone plot (c) and (d) coulombic efficiency plot of the supercapacitor (Orig 2x:x:y sample).

specific capacitance, Fig. 3.11b is obtained for a constant charge current of 2 mA. As seen from Fig. 3.11b, specific capacitance declines with increasing discharge current density. This too is reflective of the behavior of any supercapacitor.

A Ragone plot (Fig. 3.11c) is shown for the supercapacitor which shows the variation of the energy density with the power density at varying current densities as obtained from the cyclic charge-discharge experiment. The nature of the curve is consistent with those reported for MnO_2 based supercapacitors. Here we have a concave upwards decline instead of the usual convex upwards decline for the energy density. The coulombic efficiency of a supercapacitor, which depicts in general how well the device is transferring charge, is shown in Fig. 3.11d. The initial coulombic efficiency is high around 80%. At around 200 cycles, this value falls to 62%. From 500-1000 cycles, the value gradually rises to a value of 85 %. Such a rise in coulombic efficiency is not surprising and reported for capacitors [85]. Thus, the supercapacitor has good charge transfer characteristic in the beginning with a phase of gradual but slow decay in coulombic efficiency. After 1000 cycles, the coulombic efficiency hits an almost constant value. The value of coulombic efficiency after 1000 cycles is greater than 90 % on average. This is significant since it suggests that the supercapacitor material progressively gains a more stable charge transferability. The value towards the end of 2000 cycles is about 98 % which is both remarkable and desirable for practical applications.

3.4 Summary

A solid-state, lightweight, low cost, and plant-based flexible supercapacitor has been successfully fabricated. With Al/AC/lig-MnO_2 as the anode and Al/AC as the cathode, the flexible supercapacitor was assembled using PVA/H_3PO_4 gel-based electrolyte. Characterization includes micro-CT tomography and scanning electron microscope. The capacitance performance was conducted using an electrochemical setup. A series of composition of AC:lignin:MnO_2 were tested to arrive at the optimal proportions of these constituents for best electrochemical performance. Results are highlighted in the following.

- Use of lignin (anode) in combination with AC (cathode) imparts distinct advantages in terms of: 1) Higher surface packing density- as observed from the higher value of IntDen parameter for lignin in the micro-tomography image analysis. The higher surface packing density of active material helps in achieving higher energy density for the supercapacitor. 2) Stability of the interface-the smoother AC particle surface, as observed by the negative kurtosis value for AC as against positive value for lignin, helps in strong attachment of the cathode layer with the electrolyte layer resulting in better contact for electrochemical reactions. 3) High contact area- the high porosity of AC particles, as seen from SEM image, adds the advantage of enhanced surface area of contact. 4) Strong adhesion-The even distribution of AC particles, as observed from SEM images, adds to better attachment due to adhesion.

- Electrochemical study through cyclic charge discharge shows that for 2000 cycles, the maximum areal specific capacitance obtained at 6.01 mA g^{-1} is 5.52 mF cm^{-2}, which is up to 13 times higher than reported. Retention is 98.7 % after 1000 cycles and 97.5 % after 2000 cycles. The maximum energy and power densities obtained are 14.11 Wh kg^{-1} and about 1 kW kg^{-1} respectively. A high coulombic efficiency of 98 % was obtained after 2000 cycles. Due to the synergistic effect of activated carbon, lignin, and MnO_2, the fabricated AC/lig-MnO_2 supercapacitor has superior performance than reported. Such electrochemical performance of this supercapacitor makes it useful for a wide variety of device applications which employ flexible supercapacitors.
- This work thus not only demonstrates distinct advantage of using lignin in combination with AC but also explores the surface morphology feature of the electrode surface.

Moreover, optimization of all constituents of the supercapacitor is done to quantitatively justify the use of these constituents and to obtain consistent performance. In view of the fact that it is not only cumbersome but also a challenging task to commercialize the use of bio-derived materials for electronics owing to instabilities in electrochemical performance, this work makes a prudent attempt to obtain an enhanced and consistent electrochemical performance through cost effective measures. The two key and essential outcomes emphasized in this work are: i) combination of bio-derived materials in certain specific ratios can have tremendous effect on the capacity performance and retention of supercapacitors, and ii) through optimization of constituent ratios, it is possible to obtain electrochemical performance which is not only at par with many state-of-art devices but even better in many cases.

Due to the simple and cost-effective method used, and raw materials derived from green sources, this work could mark an important step towards green technology development. Besides, this work used a novel fabrication route of using plant-based raw material in solid-state flexible supercapacitors.

CHAPTER IV

NANOPARTICLE DECORATED LIGNIN AS ELECTRODES FOR ASYMMETRIC FLEXIBLE SUPERCAPACITORS[*]

In order to meet our increasing energy demand, a flexible, lightweight, and highly organized energy management strategy is needed for flexible supercapacitors. For that perspective, an anode electrode has been designed and synthesized by depositing $NiWO_4$ nanoparticles on lignin (lig) on an aluminum substrate. A supercapacitor was assembled by using Al/lig-$NiWO_4$ as the anode, Al/AC (activated carbon) as the cathode, and PVA/H_3PO_4 gel as the electrolyte. Superior electrochemical performance was achieved even after 2000 cycles of charge and discharge study. The maximum specific capacitance at 0.13 Ag^{-1} is 17.01 $mFcm^{-2}$, which is more than 42 times of that reported. The capacitance retention maintains at about 97% after 1000 cycles, and 84 % after 2000 cycles. The maximum energy and power densities are 2 Wh cm^{-2} and 100 W cm^{-2} respectively. A series of the composition of lig:$NiWO_4$:PVDF was tested to optimize the electrochemical performance. It was found that the best performance was achieved for the ratio (10:80:10) that had predominantly $NiWO_4$ nanoparticles. The remarkable electrochemical performance of these new class capacitors makes them useful for a wide variety of electronics.

---

[*] Reprinted with permission from "NiWO4 nanoparticle decorated lignin as electrodes for asymmetric flexible supercapacitors" by Swarn Jha, Siddhi Mehta, Yan Chen, Peter Renner, Selvasundarasekar Sam Sankar, Dilworth Parkinson, Subrata Kundu, Hong Liang, 2020. Journal of Materials Chemistry C, 8, 3418-3430, Copyright [2020] by Royal Society of Chemistry.

4.1 Background

Finding new, effective, and sustainable solutions to the challenges posed by the future energy storage technologies are crucial for economy and environment [1-4]. New materials for energy storage, such as in lithium-ion batteries, have been extensively focused in our research [7-9]. Batteries and supercapacitors have been the key focus of enhancing energy storage [7, 9, 11-15]. As per our recent study, microstructure and configuration have a profound influence on an electrode performance, and this enables us to design new electrodes in the present work [11, 59-62].

Supercapacitors made out of bio-wastes present a potentially viable and exciting solution to waste reduction and sustainable energy technology growth. Supercapacitors have the advantage of higher specific capacitance, energy density, and power density over the conventional dielectric capacitors [16-21]. An all-solid-state supercapacitor is highly sought due to the ease of portability and use. Additionally, the use of solid-state supercapacitors eliminates the safety risk posed by conventional liquid electrolytes which are combustible and bulky [25]. Accordingly, solid-state supercapacitors have been widely researched [26]. Due to exponential growth in the demand for wearable electronics, there has been a rising demand for flexible electronics [27-29]. Flexible devices offer the advantage of being used in conditions of additional strains without diminished performance. The bandwidth of application of wearable flexible electronics is huge, ranging from human wearable watches and clothing to sensors used in automobiles [30]. As such, a number of research efforts are directed towards the fabrication, design, and synthesis of solid-state flexible supercapacitors [32-34]. The asymmetric design of a supercapacitor is beneficial in extending the potential window by employing one electrode for Faradic reactions, and the other as a capacitor for improved power density [63-65].

Biomass-derived materials have been used for electrochemical applications for quite some time now owing to their environmental benefits. However, there are serious challenges for biomass made electrodes in terms of poor packing density, unoptimized pore structure and distribution, unknown surface chemistry which affect electrochemical performance, retention, stability, and long term usage [46]. Moreover, such usage also creates problems of electric wastes, bio-degradability, processing cost, and scalability [47]. These challenges have not only made commercialization of biomass-based electrochemical devices difficult but also have raised concerns on the potential of biomass materials as a whole for electrode applications. Besides, the source, extraction, and processing steps involved in obtaining bio-derived carbon materials are crucial factors that impact device performance and usability. Accordingly, there is an urgent need to address these issues through an innovative and rigorous approach that is consistent with the principles of green chemistry. Lignin is a natural bio-polymer abundantly available in plants. It is often produced in huge quantities as a waste of cellulose and paper processing industries. Alkaline lignin, which is produced via alkaline hydrolysis, was directly purchased and used in this study. Lignin is the conductive material used in the composite electrode [66]. Because of its cheap availability, carbon backbone, and conductive nature, it acts as an excellent sustainable substitute to other carbon materials.

Metallic oxide nanoparticles are considered as an important area of intensive research, owing to their unique properties and their potential applications. Due to a high surface to volume ratio compared, these materials exhibit fascinating properties. Considering various types of metals and metal oxides NPs, the transition metal oxides have a tendency to exhibit a wide variety of structures. Transition metal oxide such as MnO_2, ZnO, CoO, NiO, RuO_2, and CuO are widely favored candidates for supercapacitor applications. They are generally used in combination with other electroactive materials like carbon, carbon nanotubes (CNTs), carbon fibers, and carbon nanospheres owing to their remarkable ability to enhance charge transport [52-55]. Such a combination leads to a higher specific capacitance in comparison to the electric double-layer capacitors (EDLC). This is due to the enhancement of the interfacial Faradic type reactions. Due to abundance and safety, MnO_2 is widely used in pseudocapacitor applications [56, 57]. But, utilizing MnO_2 in bulk is limited due to its high electrical resistance (conductivity of MnO_2 is in the range $10^{-5} – 10^{-6}$ S cm^{-1}) [58]. To address this challenge, other novel class of transition metal oxides with higher oxidation states of elements are highly favored for enhancing pseudocapacitance. Nanosized transition metal oxides, in particular, have the potential of higher substrate permeability, and high surface area to volume ratio, which leads to greater contact area for electrochemical reactions. Due to low cost, facile preparation method, high theoretical specific capacitance, excellent electrochemical reversibility, and abundant availability, Nickel-based materials have been considered as one of the most important electrode candidates. Being a transition metal oxide, it possesses pseudocapacitance property and hence is a suitable alternative for pseudocapacitor application. The presence of nickel adds substantially to the conductivity of this transition metal oxide when compared to the traditionally used MnO_2. In addition, the high mechanical stability, a narrow bandgap of conduction, and promising electrochemical properties of divalent metal tungstate like $NiWO_4$ nanoparticles make it an excellent choice for supercapacitor applications [67]. In this work, $NiWO_4$, a novel class of transition metal oxide nanomaterial, is synthesized, and decorated on bio-derived alkali lignin for supercapacitor application.

In this research, a quasi-solid state, plant-based supercapacitor was fabricated, assembled, tested and optimized for the best performance for applications in flexible electronics. The supercapacitor is lightweight, low-cost, and made with an inexpensive fabrication process. The asymmetric supercapacitor is made up of $NiWO_4$ decorated lignin (lig) as the active material. SEM characterization was done to observe the $NiWO_4$ particle size. EDS and XPS characterizations were carried out to confirm the elemental composition and elemental nature of the $NiWO_4$ material. With Al/lig-$NiWO_4$ as the anode and Al/AC as the cathode, the flexible supercapacitor was assembled using PVA/H_3PO_4 gel-based electrolyte. The details of fabrication and assembly are provided in the experiment section. Additionally, a high-resolution synchrotron microtomography (μ-CT) imaging of the AC and the lignin-based electrode was done to obtain microscopic details of the particle morphology. The electrochemical performance was assessed using cyclic charge-discharge (CCD), cyclic voltammetry (CV), and Electrochemical Impedance Spectroscopy (EIS). Further details of the electrochemical experiment set up are covered in the experimental section. The results and discussion section covers in detail the findings of all characterization results and electrochemical analysis. A series of experiments were also carried out to arrive at the optimal constituent ratio for the lignin-NiWO4 samples. After 2000 cycles of charge and discharge, the maximum specific capacitance at 0.13 Ag^{-1} is 17.01 mF cm^{-2}, which is up to 42 times of that reported [68]. The capacitance retention maintains at about 97% after 1000 cycles. The maximum energy and power densities are 2 Wh cm^{-2} and 100 W cm^{-2} respectively. The relatively remarkable electrochemical performance of this plant-based supercapacitor makes it useful for a wide variety of device applications that employ flexible supercapacitors. Due to relatively simple, cost-effective methods used, and raw materials derived from green sources, this work could mark an important step towards green technology development.

4.2 Experimental

4.2.1 Synthesis of Nickel Tungstate nanomaterials ($NiWO_4$)

Nickel tungstate was prepared by a simple wet chemical route at room temperature. For this synthetic route, 0.5 M of nickel acetate tetrahydrate (Sigma-Aldrich, India) was mixed with 100 ml of distilled water until to get a homogeneous solution under magnetically stirred condition. Similarly, 0.2 M of sodium tungstate (Sigma-Aldrich, India) was mixed with a required amount of distilled water. A homogeneous solution of sodium tungstate was added in a dropwise manner into an aforementioned nickel acetate solution. A greenish-blue precipitate was observed. The mixture was maintained under the stirred condition for 1hr and the obtained precipitate was centrifuged and dried. The corresponding synthetic method is portrayed in Fig. 4.1.

4.2.2 Preparation of Al/lignin-$NiWO_4$ Composite Electrode

The $NiWO_4$ nanoparticles were added to lignin (alkaline, TCI, density = 50 g/l, pH = 8-10) and mixed with PVDF in 3 different molecular weight ratios of Lignin: $NiWO_4$: PVDF to form three sample mixtures. The 3 ratios chosen were 80:10:10 (L-80), 45:45:10 (L-45), and 10:80:10 (L-10). After this, 2 ml of NMP (Sigma. Aldrich, density = 1.028 gml^{-1}, MW= 99.13 $gmol^{-1}$, > 99 % pure) was added to each of the aforementioned sample mixtures to form the slurry. The slurry was coated on an aluminum foil (0.98 mm thick) substrate cut in the form of a circular plate of diameter 4 cm. The adjoining strips of the foil were 1 cm wide and 3 cm long and could be flexibly used over a 360^0 angle thus imparting flexibility feature to the supercapacitor. The coated foil was heated in a vacuum oven for 4 hours at 100°C to obtain the Al/lignin-$NiWO_4$ composite electrode.

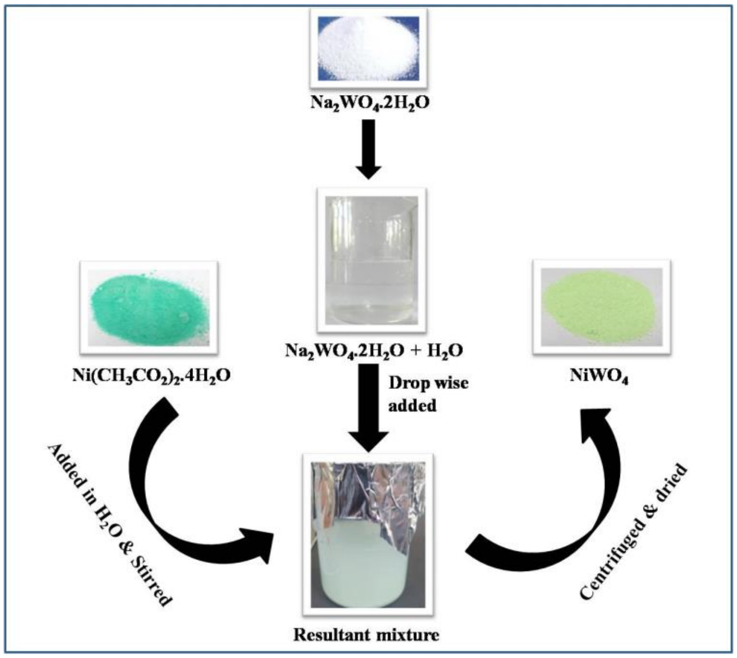

Fig. 4.1. Schematic representation of $NiWO_4$ synthetic procedure.

4.2.3 Preparation of PVA/H_3PO_4 Gel Electrolyte

A gel-like electrolyte of PVA/H_3PO_4 was prepared by adding 10 ml water to 1 g PVA (Aldrich, MW=85,000 – 124,000, > 99 % pure). It was mixed at 80 ^{0}C for 40 mins. Subsequently, 0.8g H_3PO_4 (Sigma Aldrich, MW = 82.0 gmol^{-1}) was added and stirred for 20 mins at 70°C. For the supercapacitor separator, a commercial paper (Sterlitech, 3×3”, W33, nitrogen-free, white) dipped in the gel, was used. It had the same dimensions as the electrode.

4.2.4 Fabrication of Quasi-solid state Asymmetric Supercapacitor

To fabricate the supercapacitor, the electrodes made earlier were used. The Al/lignin-$NiWO_4$ composite electrode was used as the positive electrode, and Al/AC was used as the negative electrode. The asymmetric supercapacitor was then constructed by sandwiching the two electrodes with the electrolyte gel. It should be noted that since H_3PO_4 is used indirectly but in a blended gel form with PVA, the gel- polymer-based PVA/H_3PO_4 electrolyte has less potency to corrode the aluminum substrate. Moreover, aluminum has dense native oxide that further protects the aluminum metal underneath from any corrosive effects of the less potent acid of the gel electrolyte.

4.2.5 Material Characterization

Nickel acetate tetrahydrate and sodium tungstate were procured from Sigma-Aldrich, India. The XRD analysis was done with a scanning rate of 5° min^{-1} in the 2θ range 10-90° using a Bruker X-ray powder diffractometer (XRD) with Cu K_α radiation (λ = 0.154 nm). X-ray photoelectron spectroscopic (XPS) analysis was performed by using a Theta

Probe AR-XPS system (Thermo Fisher Scientific, UK). Scanning Electron Microscopy (SEM) analysis with Electron dispersive X-ray spectroscopy (EDS) was done using Hitachi, Japan make model S-3000H having magnification 30X to 300 kX with the accelerating voltage ~ 0.3 to 30 kV.

4.2.6 Synchrotron X-ray Tomography (μ-CT)

Synchrotron X-ray tomography was carried out at beamline 8.3.2 at the Lawrence Berkeley National Laboratory at its Advanced Light Source (ALS) facility. This was done to obtain details of electrode morphology, structure, and the interface of the supercapacitor. Using this non-destructive tool, the inner layers of electrode samples can be viewed. With the sample being rotated over 180 degrees, 3600-1800 images were taken. X-rays at 35 KeV was used. For detection, a 50 uM Ce: LuAG scintillator, a Mitutoyo 5X lens, and a PCO edge sCMOS camera were used. with a resolution of 1.3 microns. For reconstructing the volumes, Xi-CAM and TomoPy software packages were used [69]. Avizo and FIJI software packages were employed for 3D visualization. The sample scans took 45 minutes for each sample. After the 2D images were concatenated, contrast enhancement was done using imageJ software [70]. Image data analysis was carried out to understand the dependence of electrochemical performance on the morphology of the particles of the electrodes.

4.2.7 Electrochemical experiments

Electrochemical characterization was performed using a Gamry potentiostat version 6.33. The $NiWO_4$ based electrode of the supercapacitor was used as the working (positive) electrode For the cyclic voltammetry (CV) experiment. The AC based electrode of the supercapacitor was connected to the reference and counter terminals of the potentiostat. CV experiment was performed at various scan rates i.e. at 10, 25, 50 and 100 mVs^{-1} to assess the effect of scan rate on the supercapacitor's electrochemical performance. The voltage range 1-2V and the scan rate of10 mVs^{-1} was found to be optimal for the CV experiment (.plots are shown in Fig. 4.6). To assess the supercapacitor impedance behavior, electrochemical impedance spectroscopy was carried out (using a frequency range of 10^6 Hz to 0.1 Hz, AC volts of 10 mv, and DC at 1 V). In the frequency range selected, all crucial high frequency-dependent steps such as the ion-transfer resistance in the electrolyte and the charge transfer resistance in the capacitive double layer are covered. The low-frequency dependent diffusion kinetics in the electrode is also covered in the selected frequency range. Nyquist plots were obtained in the beginning, and after 500th, 1000th, 1500th, and the 2000th cycle (Fig. 4.7c). For the cyclic charge-discharge (CCD) experiment a current density of 130 mAg^{-1} was used. For each charge and discharge cycle, a one-minute duration was provided. with 20 V being the upper limit of voltage.

4.3 Results and discussion

a

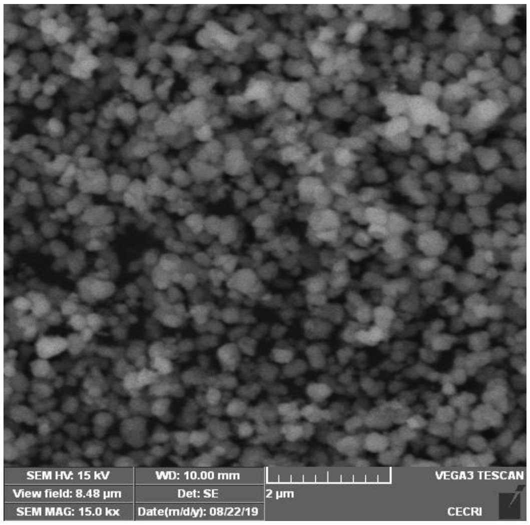

b

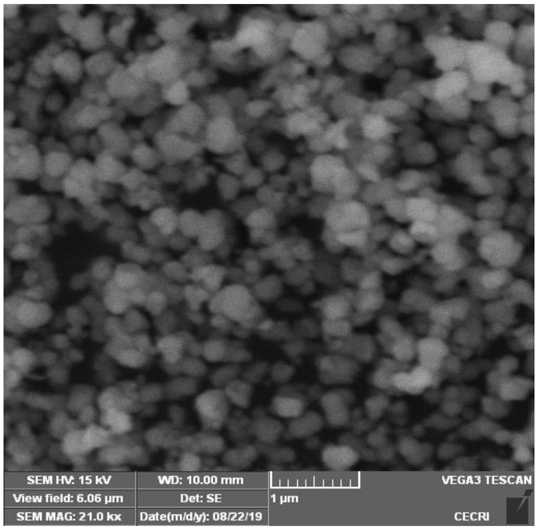

c

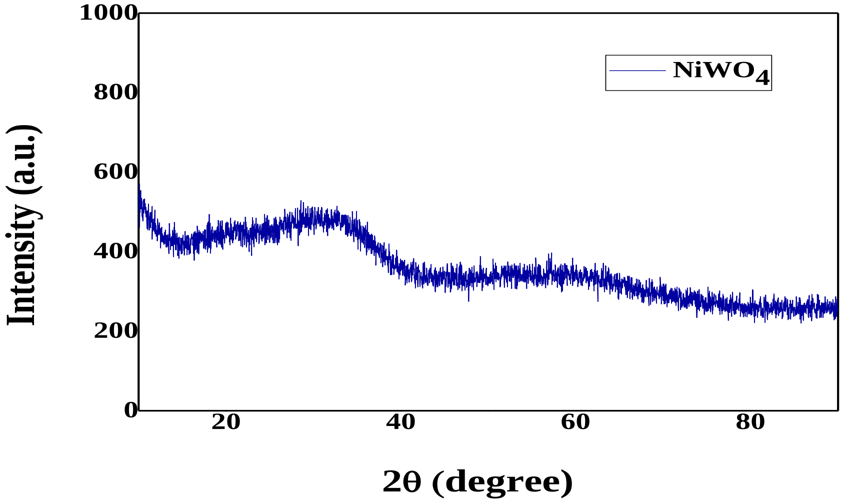

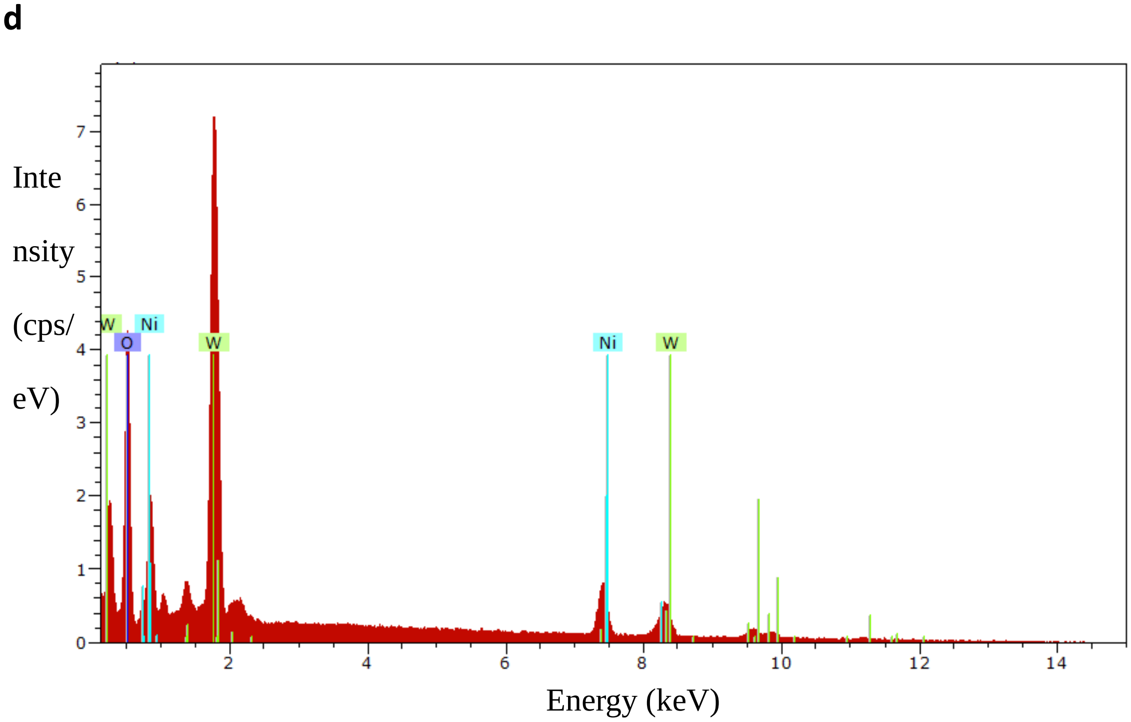

Fig. 4.2 (a-b). The low and high magnification SEM analysis of the $NiWO_4$ nanomaterials. Scale bar is 2 µm for (a) and 1 µm for (b). X-ray diffraction analysis (XRD) of $NiWO_4$ nanoparticles (c), and the EDS spectrum of the $NiWO_4$ nanomaterials (d).

4.3.1 $NiWO_4$ nanoparticle characterization results

To understand the morphological aspects of $NiWO_4$ particles, scanning electron microscopy (SEM) images were taken. Fig. 4.2(a-b) are the low (Fig. 4.2a) and high (Fig. 4.2b) magnification SEM images of $NiWO_4$. From these images, uniform distribution and size of the material can be clearly visualized. To verify the existence of $NiWO_4$ particles, XRD was performed and the corresponding XRD spectrum is shown in Fig. 4.2c. No sharp peaks are observed. From this observation, we concluded that the

$NiWO_4$ nanomaterials are amorphous in nature. Corresponding energy dispersive spectroscopy (EDS) analysis was carried out in order to find out the elemental composition of the synthesized material and the corresponding EDS spectrum is shown in Fig. 4.2d. As seen in Fig. 4.2d, the observed elemental compositions are Nickel, Tungsten, and Oxygen with a weight percentage of 15.87, 54.96 and 29.16 % respectively. High-resolution X-ray photoelectron spectroscopy (XPS) was utilized to find the elemental nature of the $NiWO_4$ material. The corresponding XPS spectrum is shown in Fig. 4.3(a-d). Fig. 4.3a shows the survey spectra of $NiWO_4$ where the peaks for Ni 2p, O 1s, and W 4f are observed at the binding energy values of 856.6, 532.2 and 36.6 eV respectively. Fig. 4.3b shows the high-resolution spectrum of Ni 2p where the peaks of Ni 2p 3/2 and Ni 2p 1/2 are observed at the binding energy values of 856.3 and 874.1 eV respectively. This characteristic doublet was observed due to the spin-orbit coupling effect. The shake satellite peaks appeared for Ni 2p 3/2 and Ni 2p 1/2 at 826.1 and 880.1 eV respectively. It was confirmed that Nickel present is of oxidation state +2. The high-resolution spectrum of W 4f is shown in Fig. 4.3c. The observed binding energies of 34.66, 36.83, and 40.65 eV was corresponding to W 4f 7/2, W 4f 5/2, and W 5p 3/2 respectively. Thus, it was concluded that tungsten exhibits an oxidation state of +6 in the synthesized $NiWO_4$ particles. As seen in Fig. 4.3d, the O 1s high-resolution spectrum with binding energies of 529.8 and 531.4 eV implies the formation of metal oxide in $NiWO_4$.

4.3.2 Synchrotron tomography

To understand the structure and interface of the electrode composite, we conducted a tomographic study. Literature reports on using tomography have been mostly focused on observing the material structure, morphology, and pore distribution [50, 71]. This works not only helps to observe the structural and morphological details of the complex 3D network of active materials but also details on electrode surface features like surface packing density, roughness, void fraction, nanoparticle distribution across interface all of which directly impact a supercapacitor's energy density and mechanical stability.

3D features of alkali lignin-NiWO4 have been detailed for the first time along with corresponding effects on the electrochemical behavior of the supercapacitor. Fig. 4.4a shows the tomography image of the lignin-$NiWO_4$ supercapacitor electrode with lignin particles seen in the dark blue shade while the $NiWO_4$ particles are seen in red and orange colors distributed across the interface. Fig. 4.4b shows the $NiWO_4$ particles alone dispersed across the supercapacitor interface. Such a scan was possible due to the high K-edge of $NiWO_4$ [72]. To understand the morphology of particles of the AC and lignin-based electrodes, two fresh and separate samples of supercapacitors were assembled.

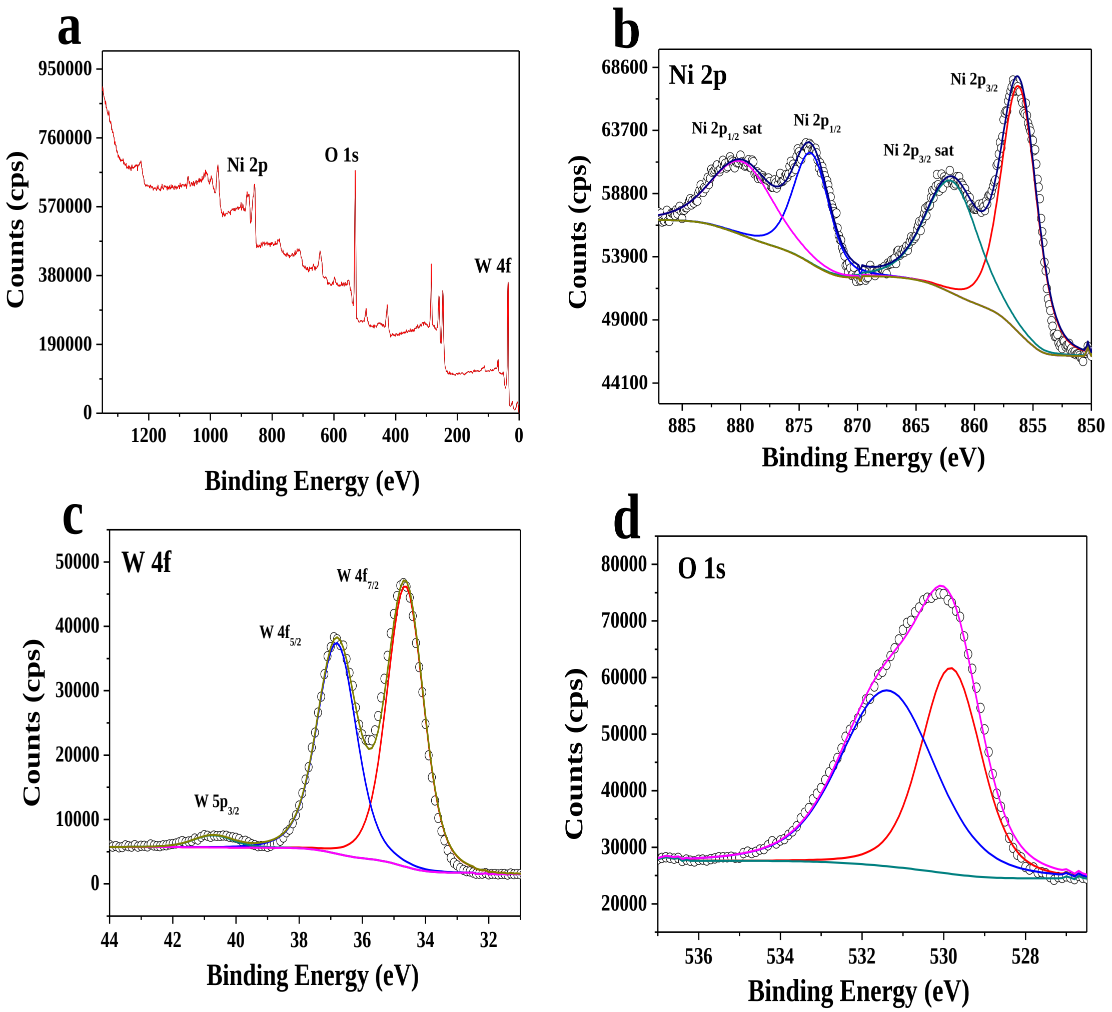

Fig. 4.3. (a-d) are the High-resolution XPS spectrum of $NiWO_4$ nanomaterials, 'a' is the survey spectrum of $NiWO_4$ nanomaterials. (b-d) are the high-resolution spectrum of Ni 2p, W 4f, and O 1s respectively.

One of the supercapacitors was made up of AC while the other was made up of lignin particles. In order to get detailed information on the morphology of each particle, high-resolution synchrotron X-ray tomography was conducted on two supercapacitors. Fig. 4.4c shows the dispersed morphology of the lignin-based supercapacitor. The morphology of the activated carbon (AC) based supercapacitor is shown in Fig. 4.4d. imageJ was used for analysis. For studying the detailed particle morphology, a similar 150 × 50 µm section (marked yellow) was selected in both Fig. 4.4c and Fig. 4.4d. Table 5 shows the parameters of interest which include size, shape, surface packing density, particle circularity, particle distribution, and the measures of central tendencies.

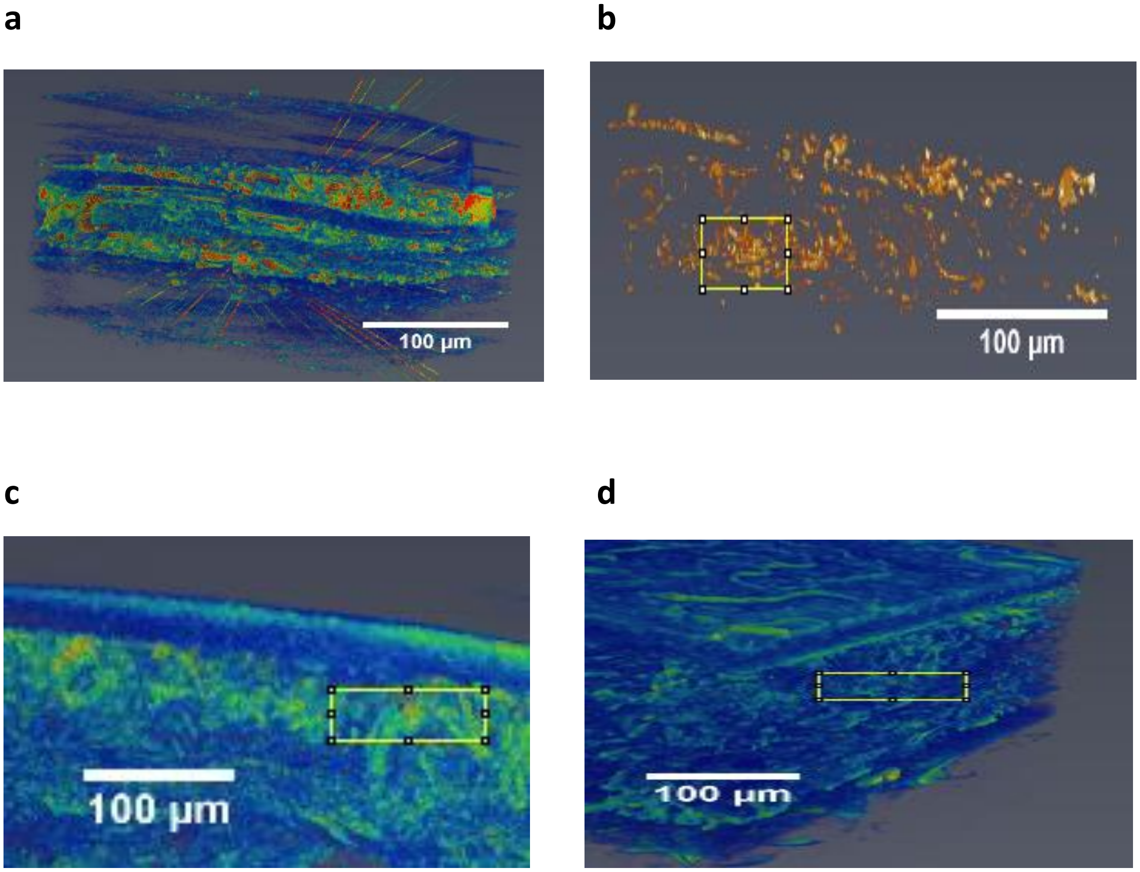

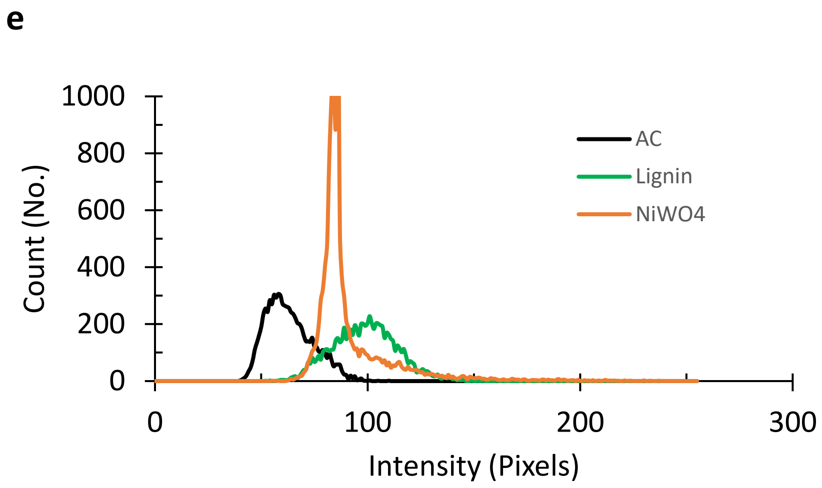

Fig. 4.4. High-resolution synchrotron X-ray tomographic image of (a) the lig-$NiWO_4$ supercapacitor electrode (scale bar = 100 µm), (b) K-edge image of $NiWO_4$ nanoparticles as distributed in the lig-$NiWO_4$ supercapacitor interface (scale bar = 100 µm); c) lignin-based supercapacitor electrode, (d) AC supercapacitor electrode, and e) the comparative histogram plots of count of particles (Y-axis) versus intensity (pixels) for the AC, lignin-based supercapacitor electrodes and the NiWO4 nanoparticles shown in (a), (b), and (c). Yellow rectangle section of dimension 50 × 30 µm is shown in (b) and of dimension 150 × 50 µm is shown in (c) and (d). X-axis direction is the horizontal line (width) and the Y-axis direction is the vertical line (height).

Circularity (Circ.) is represented by equation 1. As seen from Table 5 circularity of lignin (0.6) is smaller than that of AC (0.7). This indicates lignin particles, on average, are more elongated than AC particles. This is on account of a more elongated carbon chain structure and a more complex 3D orientation of chains in lignin compared to AC.

$$Circ. = 4 \times \frac{[Area]}{[Perimeter]^2} \qquad (1)$$

The pixel counts versus the intensity of the pixels for AC based (black), lignin-based (orange) supercapacitor electrodes, and the $NiWO_4$ nanoparticles is captured in Fig. 4.4e. It can be seen that the peak of the lignin curve occurs at 104 pixels while that of the AC and $NiWO_4$ curves occur at 60 pixels and 83 pixels respectively.

As seen from Table 5 the mean of the AC curve is 60.96 while that of the lignin curve and $NiWO_4$ particle curves are 82.83 pixels and 91.26 pixels respectively. This indicates lignin has a higher number of functional groups with higher K-edge values compared to AC. $NiWO_4$ particles have the highest intensity of the three which is typical of a metal oxide displaying higher K-edge in X-ray tomography.

Table 5. Particle morphological measurements obtained from the tomography image for the AC, lignin-based supercapacitors (SC), and $NiWO_4$ nanoparticles.

Parameter	AC SC	Lignin SC	$NiWO_4$
Mean	60.96	82.83	91.267
StdDev	9.29	10.09	18.557
Min	40	53	55
Max	92	124	237
Circ.	0.7	0.6	0.741
IntDen	311232	417224	141242
Skew	0.26	-0.02	3.072
Kurt	-1.08	0.85	11.188
AR	2.941	3.92	1.621

As for intensity, the AC based supercapacitor has a minimum of 40 pixels and a maximum of 92 pixels (Table 5). These values of intensities are lower than the intensity values of the lignin-based supercapacitor (min= 53, max = 124 pixels). This is also indicated by the right shift in the lignin curve (Fig. 4.4e). This suggests that compared to the AC particles, the penetrating X-rays face a higher resistance from the lignin particles. This indicates the presence of more complex and elongated carbon chains in lignin compared to AC. The more elongated nature of lignin particles is also evidenced by the value of the aspect ratio (AR). When particles are fit with an elliptical shape, the ratio of major to the minor axis is depicted by the aspect ratio. AR values for AC and lignin particles are 2.941 and 3.92 respectively (Table 5). The $NiWO_4$ particles have the least aspect ratio of the three implying that the major and minor axis is somewhat closer to each other in length which is characteristic of a circle. The sum of total pixels in the curves of AC, lignin supercapacitors, and $NiWO_4$ particles is represented by Integrated density ('IntDen' parameter in Table 5). A higher surface packing density of particles translates into a corresponding higher value of the 'IntDen' parameter. The IntDen value of lignin (417,224) is higher that of AC (311,232) by a factor of 25.40 % (Table 5). Thus, the lignin supercapacitor has more surface mass distribution. $NiWO_4$ particles have the least IntDen value (141,242) implying it has the least surface mast distribution of the three. It is also indicative of the fact that the $NiWO_4$ particles are more spread out through the substrate. If a distribution curve has a tail extending to the right of the center of mass, it is indicated by the positive skewness (skew) parameter. A higher positive value of skew (Table 5) for AC (0.26) indicates at a longer tail compared to lignin (-0.02). This means that the surface of the lignin-based supercapacitor is a better Gaussian surface. A negative kurtosis (Kurt) value for AC suggests that the AC electrode's surface is flatter compared to that of the lignin electrode ('kurt' value is positive). Lignin electrode has more peaked distribution as indicated by the positive ‘kurt’ value, thus, substantiating that the lignin electrode surface is rougher than that of AC. For achieving a higher energy density of the supercapacitor, a higher surface packing density is required. For better interfacial contact and enhanced charge transport, a low electrode surface roughness is desirable. Therefore, it is seen that using lignin and AC combination in the Al/lig-NiWO$_4$//AC/Al supercapacitor has distinct advantages. The combination helps in attaining both a higher surface packing density (lignin electrode) and low surface roughness (AC electrode) for the supercapacitor. Within the active material, a reduction in the surface void fraction, due to the elongated lignin molecules, further reduces internal ion transport resistance. This synergistic approach of supercapacitor fabrication thus addresses the issue of the low surface packing density of material observed with other biomass fabricated electrodes [46].

4.3.3 Electrochemical performance

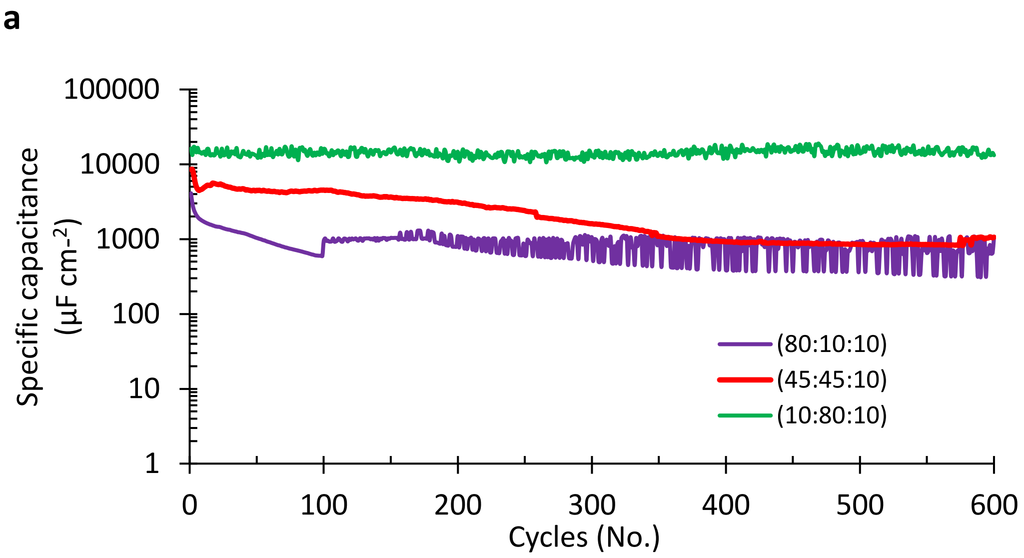

b

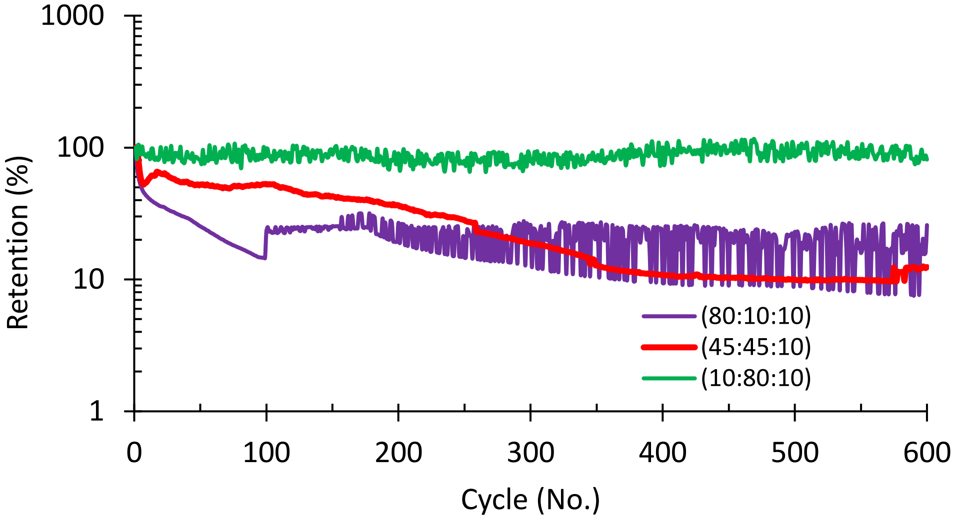

Fig. 4.5. Plots for the (a) variation of specific capacitance with cycles for the CCD experiment at a current density of 0.13 Ag^{-1} for 600 cycles, and (b) the retention comparison for the samples with different Lignin:NiWO4:PVDF ratios.

To assess the capacitance performance of the supercapacitors with varying lig:$NiWO_4$: PVDF ratios, a cyclic charge-discharge (CCD) experiment was carried out at the same current density of 0.13 Ag^{-1} for 600 cycles each. The samples were named in the order lig:$NiWO_4$:PVDF ratio, the numbers indicate the weight percentage for each component. For instance, 10:80:10 symbolizes 10 % lignin, 80 % $NiWO_4$ and 10 % PVDF by weight. The variation of areal specific capacitance with cycles is shown in Fig. 4.5a for the first 600 cycles. Areal specific capacitance retention is shown in Fig. 4.5b. It is seen from Fig. 4.5a that the areal specific capacitance for the sample 10:80:10 is the highest throughout (about 17.01 mF cm^{-2}) followed by the samples 45:45:10, and 80:10:10 in the order of the greatest to the least. As seen in Fig. 4.5b, the order of the final retention, however, follows the order 10:80:10 > 80:10:10 > 45:45:10. Therefore, it is observed that on increasing the weight % of $NiWO_4$, the areal specific capacitance and the retention both increase. This indicates the remarkable influence of the $NiWO_4$ nanoparticles in providing not only higher capacitance but also stability to the supercapacitor. The lignin-$NiWO_4$ supercapacitor reported here is a pseudocapacitor. The lignin is the conductive carbon material and $NiWO_4$ is the transition metal oxide that imparts the pseudocapacitance property to the supercapacitor. If only $NiWO_4$ with PVDF is used, the device will not act like even a supercapacitor since $NiWO_4$ (as with any transition metal oxide by itself) cannot have the level of conduction required for a supercapacitor. The role of $NiWO_4$ is restricted to only imparting pseudocapacitance property to the supercapacitor (due to oxidation-reduction reactions). If only lignin is used, the fabricated capacitor will mimic an EDLC type capacitor (like that of a graphite-based material). Due to several and highly complex nature of functional groups in lignin, an EDLC type capacitor fabricated with lignin alone will show extreme instability and poor retention in the absence of any pseudocapacitor material ($NiWO_4$ in this case). A glimpse of such behavior is observed in sample 80:10:10, which has predominantly lignin. As such it shows high instability, poor retention, and low specific capacitance compared to the other samples. Based on the above understanding, it is reasonable to present results for three samples with varying lignin:$NiWO_4$:PVDF compositions.

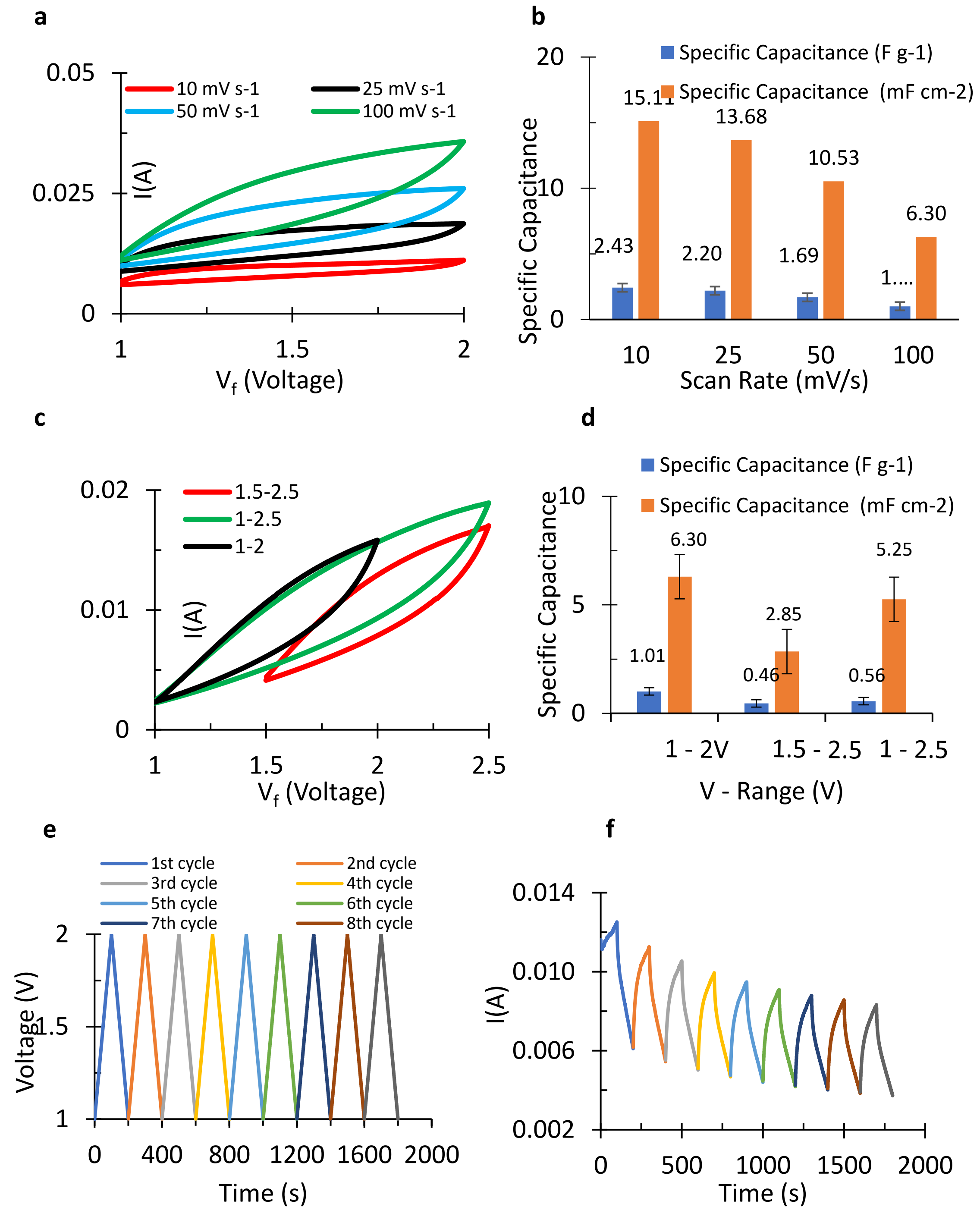

Fig. 4.6. For the lig-$NiWO_4$ supercapacitor (sample 10:80:10): (a) cyclic voltammetry curve at various scan rates, (b) comparative histogram of specific capacitance versus scan rate, (c) cyclic voltammetry curves for different voltage ranges, (d) comparative

histogram of specific capacitance versus voltage range at 10 mVs^{-1}, (e) voltage vs time plots, and (f) current vs time plots for the first nine cycles.

In accordance with this result, the best sample 10:80:10 was selected for further tests. For comparison, the CV curves obtained at scan rates 10, 25, 50, and 100 mVs^{-1} are shown in Fig. 4.6a. It was found that at scan rates higher than 10 mVs^{-1}, the scan voltage rate was too fast. For scan rates lower than 5 mVs^{-1}, it was too slow for stable dynamics of the system. Thus, 10 mVs^{-1} was selected to perform the cyclic voltammetry for longer runs. The specific capacitances obtained at varying scan rates (Fig. 4.6b) reiterates this fact. The average value of specific capacitance for the 10:80:10 sample obtained at 10 mVs^{-1} is 15.11 mF cm^{-2} which is the highest while that obtained at 100 mVs^{-1} is 6.3 mF cm^{-2} which is the least. For the cyclic voltammetry experiment, it is important to determine the operating voltage window. For the scan rate of 10 mVs^{-1}, Fig. 4.6c shows the obtained CV curves at several voltage ranges. The highest average specific capacitance (6.3 mF cm^{-2}) was obtained in the voltage range of 1-2 V (Fig. 4.6d). Further as observed in the CV experiment, the voltage-time (Fig. 4.6e) and current-time (Fig. 4.6f) curves are shown for the 10:80:10 ratio supercapacitor, for the first few cycles. The variation of voltage remains constant with cycles. This indicates that the voltage was varied constantly (Fig. 4.6e). For each cycle to the starting voltage is 1V, which climbs to 2V and then the voltage tends to decay with a negative slope to 1V after the electrode polarity is reversed. The current developed in the supercapacitor depends on the electroactive material, the electrolyte, and the design of the supercapacitor. The current developed follows closely the cyclical pattern of the voltage in each cycle (Fig. 4.6f). However, unlike the voltage, the curve is non-linear with respect to time. The supercapacitor discharges more quickly compared to charging. This is depicted by the steeper slope of the discharge part of the current-time curve (Fig. 4.6f). Due to gradual decay of the active material owing to electrochemical reactions in the supercapacitor, the current declines gradually in subsequent cycles below the highest value of the first cycle.

a

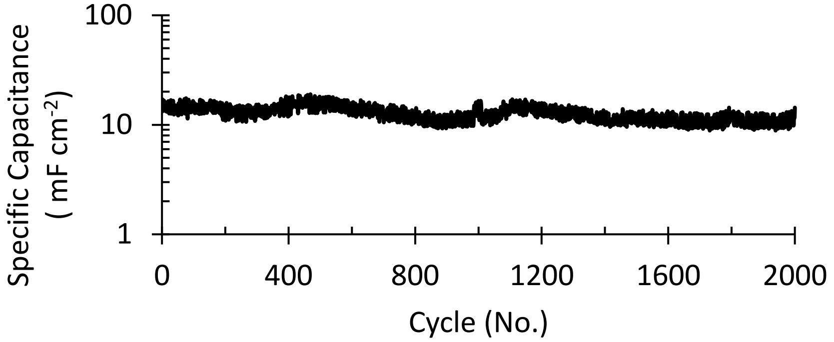

b

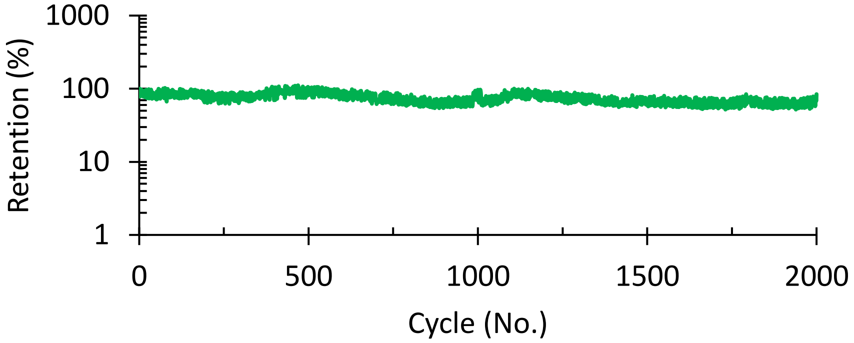

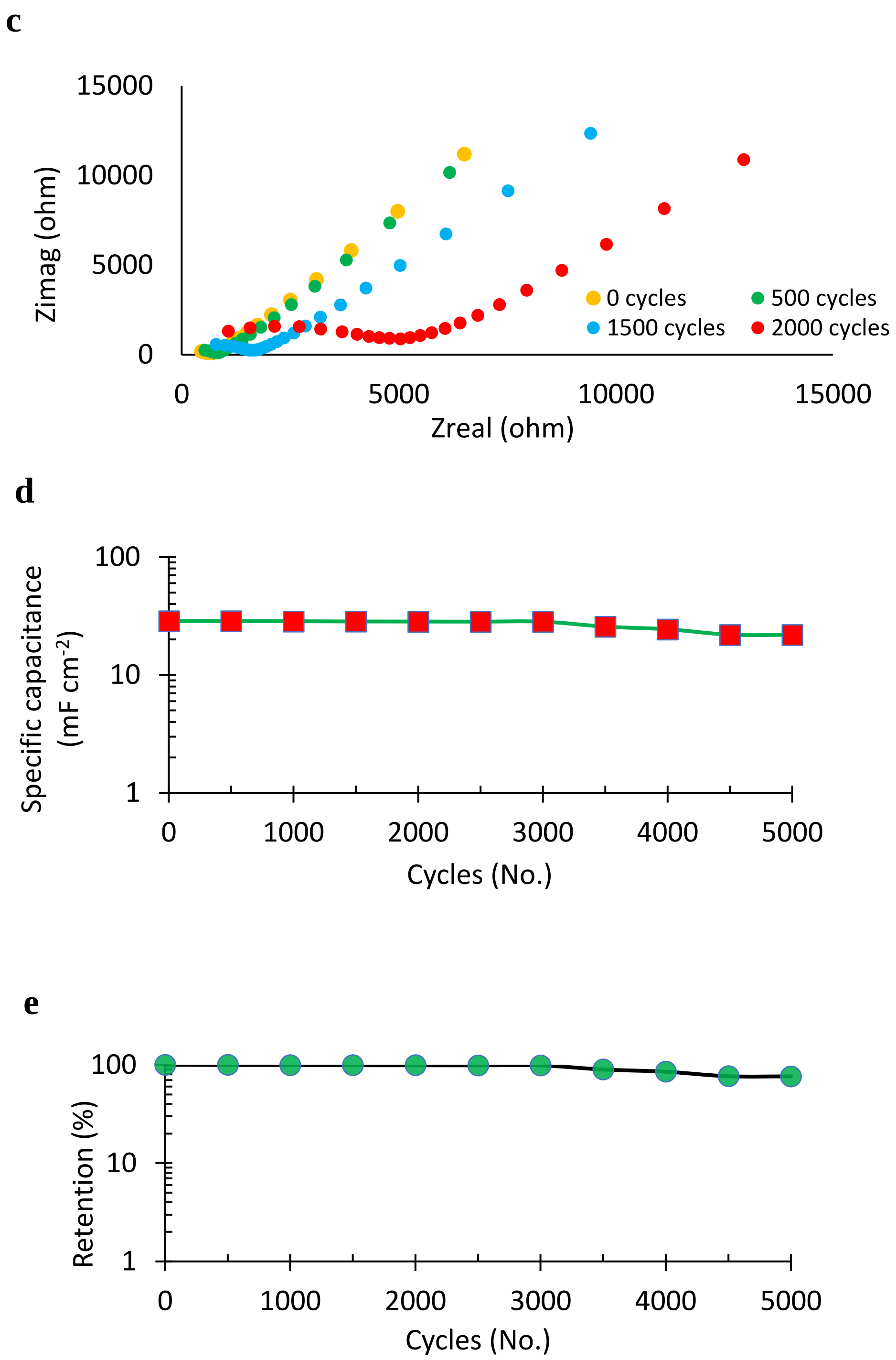

Fig. 4.7. Plots for the Lignin:NiWO4:PVDF ratio of 10:80:10, (a) specific capacitance vs cycles, (b) retention, (c) Electrochemical impedance spectroscopy (Nyquist plots), (d)

specific capacitance vs cycles for 5000 cycles, and (e) retention vs cycles for 5000 cycles.

To study the cycling life of the supercapacitor, the 10:80:10 sample was run at a current density of 0.13 Ag^{-1} until 2000 cycles (Fig. 4.7a). The initial areal specific capacitance is 17.01 mF cm^{-2} which remains nearly constant throughout the first 1000 cycles with a value of 16.5 mF cm^{-2} after 1000 cycles (97 % retention, Fig. 4.7b). The final value after 2000 cycles was 14.29 mF cm^{-2} (84 % retention, Fig. 4.7b). Thus, there is only a marginal decline in the areal specific capacitance. The maximum energy density and power density obtained were 2 Wh cm^{-2} (8.49 Wh kg^{-1}) and 100 W cm^{-2} (509.48 W kg^{-1}) respectively (Table 6). A fresh supercapacitor sample of the ratio 10:80:10 was tested for 5000 cycles as part of further work. The supercapacitor shows similar specific capacitance (Fig. 4.7d, the maximum specific capacitance of 28.66 mF cm^{-2}) and retention behavior (Fig. 4.7e, retention 76.38%) even after 5000 charge-discharge cycles. The electrochemical performance of the fabricated Al/lig-$NiWO_4$ supercapacitor is compared

in detail with the literature reports and is shown in Table 6. Notably, the electrochemical performance comparison for the exact material (Al/AC//Al/lignin-$NiWO_4$)is not possible because it is new material. However, some reported works for supercapacitors are shown in Table 6 to compare with sources cited in the last column (Ref.). The obtained specific capacitance (Table 6) of the present work (SPCP) to the specific capacitance of reported works ranges from 2.65 – 41.89 which is noteworthy and remarkable. Therefore, the supercapacitor sample 10:80:10 has an electrochemical performance that is not only at par with those reported but even better than many others.

Electroimpedance spectroscopy was done to study the impedance behavior of the supercapacitor. For this, the Nyquist plots are obtained and shown in Fig. 4.7c. For the sample 10:80:10, as seen in Fig. 4.7c, the total impedance at the beginning (dotted orange) is about 500 ohm which is smaller than 1000 ohm, the value after the 500th cycle

Table 6. Comparison of the Al/AC//lig-$NiWO_4$/Al supercapacitor's electrochemical performance with literature reports.

Substrate	Materials	Max. Specific Capacitance (SPC)	SPCP/ SPCG ‡	Energy Density (Wh cm^{-2})	Power Density (Wcm^{-2})	Ref.
Aluminum	lignin-$NiWO_4$	17.01 mF cm^{-2} at 0.13 A g^{-1}, 2000 cycles	1	2	100	This work
PET	β-Ni(OH)2/graphene	2.57 mF cm^{-2} at 0.2 Am^{-1}, 2000 cycles	6.62	-	-	[76]
FTCF	rGO/PANI	6.4 mF cm^{-2} at 0.08 mA cm-2, 2000 cycles	2.66	-	-	[77]
PET	$SnSe_2$	0.406 mF cm^{-2} at 20 mA m^{-2}, 1000 cycles	41.89	-	-	[68]
PET	N-Doped rGo	3.4 mF cm^{-2} at 0.5 µA cm^{-2}, 2000 cycles	5.0	-	-	[75]
Titanium	Carbon nano tube	1.84 mF cm^{-2} at 1 mA, 1000 cycles	9.24	-	-	[73]
Carbon based fabric	MnO_2//MoO_3	4.86 mF cm^{-2} at 0.5 mA cm^{-2}, 3000 cycles	3.5	-	-	[74]

---

‡ SPCP/SPCG is the ratio of specific capacitance of present work (SPCP) and specific capacitance of the cited work (SPCG).

(dotted green). Similarly, the impedance after the 1500th cycle (dotted sky blue) is 1620 ohm which is smaller than that after the 2000th cycle (dotted red). The impedance values follow the trend 0th, 500th, 1000th, 1500thand 2000th cycle from the least to the greatest. This provides evidence that with the progression of cycles, the impedance to current flow increases. Due to increasing impedance, the current flow decreases, and a lesser capacity retention occurs towards the higher cycle numbers. The rate at which impedance develops, however, is steeped towards the end, i.e., from the 1500th to the 2000th cycle.

To observe the impact of current density on the resultant discharge voltage in the cyclic charge-discharge experiment, Fig. 4.8a is obtained. The resultant voltage curves are obtained at various current densities of 0.01 A/g (green), 0.03 A/g (sky blue), 0.06 A/g (orange), and 0.1 A/g (red). The slope of the discharge voltage, which represents the rate of decline of voltage at varying current densities, is the key point of interest. It is seen that the higher the current density, the steeper is the slope of the voltage-time curve. Therefore, the voltage drops at a higher rate at a higher current density that is expected behavior a supercapacitor. To obtain the effect of discharge current density on specific capacitance, Fig. 4.8b is obtained for a constant charge current of 2 mA. As seen in Fig. 4.8b, specific capacitance declines with increasing discharge current density i.e. the specific capacitances at 0.013, 0.026, 0.064, 0.128 A g^{-1} are 129.7, 32.94, 12.63, and 6.39 mF cm^{-2} respectively thus depicting the characteristics of a supercapacitor.

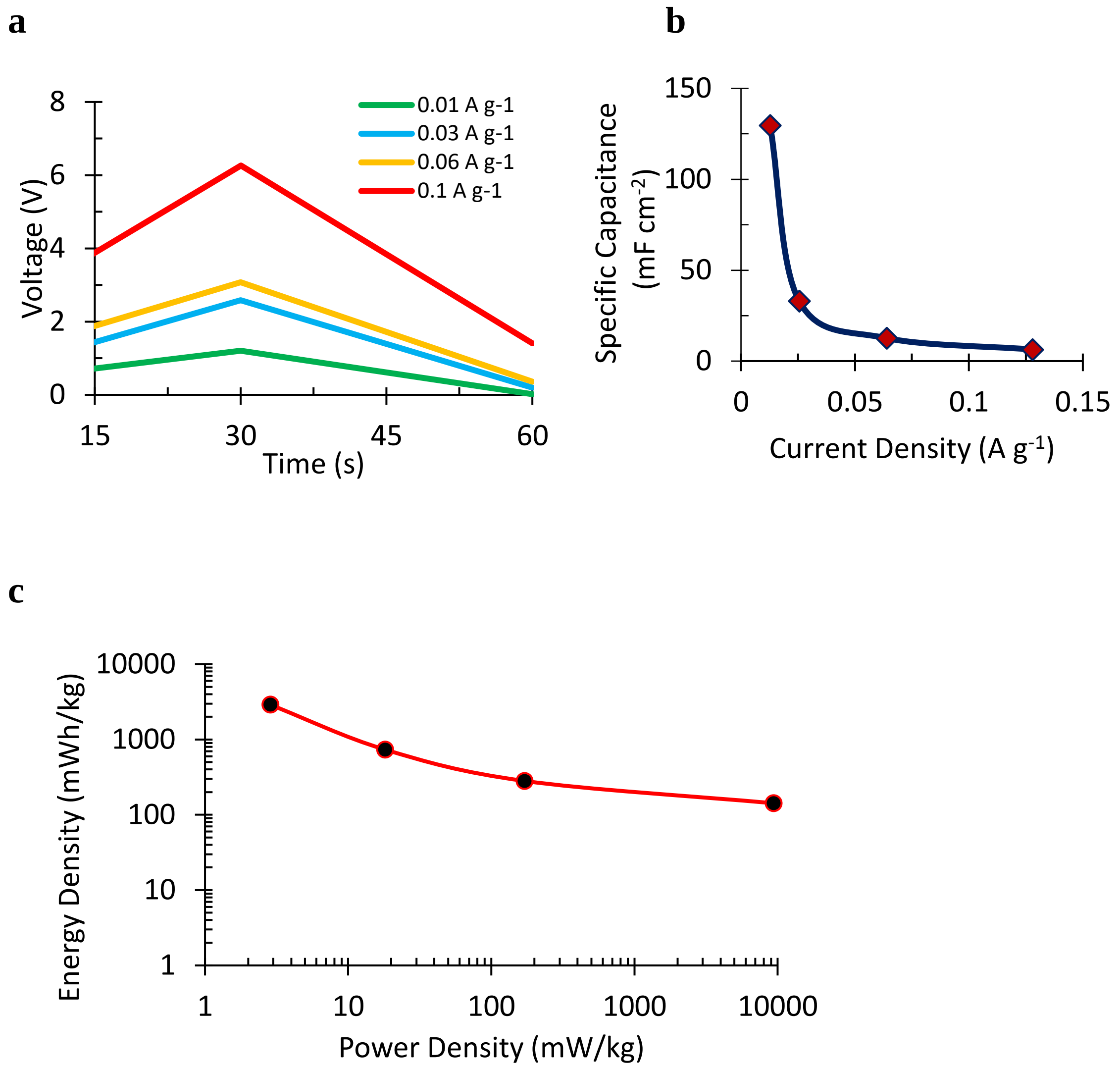

Fig. 4.8. Comparative plots of (a) voltage versus time at different current densities, and (b) specific capacitance versus current density in the cyclic charge-discharge experiment at a charge current of 2 mA, and (c) Ragone plot of the lig- NiWO$_4$ supercapacitor.

As obtained from the cyclic charge-discharge experiment, a Ragone plot (Fig. 4.8c) is shown for the supercapacitor. It shows the variation of the energy density with the power density at varying current densities. The trajectory of the curve is consistent with those reported for metal oxide-based supercapacitors. There is a concave upwards decline for the energy density instead of the usual convex upwards decline.

4.4 Summary

Nanoparticle $NiWO_4$ was used to decorate lignin (lig) in order to enhance the electrochemical reaction. Utilizing Al/lig-$NiWO_4$ as an anode and Al/AC as a cathode, we designed and fabricated a new class of supercapacitors with PVA/H_3PO_4 gel as an electrolyte. The maximum specific capacitance achieved at 0.13 Ag^{-1} is 17.01 $mFcm^{-2}$. The capacitance retention maintains about 97% after 1000 cycles. The maximum energy and power densities obtained are 2 Wh cm^{-2} (8.49 Wh kg^{-1}) and 100W cm^{-2} (509.48 W kg^{-1}) respectively. This remarkable electrochemical performance enables us to utilize them in a wide variety of electronic applications. A series of the composition of lig:$NiWO_4$ was tested to arrive at the optimal proportions of these constituents for the best electrochemical performance. The contribution of each constituent was studied by varying their compositing ratio. The first ratio (80:10:10) had predominantly lignin, the second ratio (45:45:10) had equal amounts of lignin and $NiWO_4$, while the third ratio (10:80:10) had predominantly $NiWO_4$ nanoparticles. Results showed that a higher proportion of the $NiWO_4$ nanoparticles compared to lignin imparted both high specific capacitance and retention to the supercapacitor. It is both cumbersome and a challenging task to commercialize the use of bio-derived materials for electronics because of instabilities in electrochemical performance. In this work, a prudent attempt is made to obtain an enhanced and consistent electrochemical performance of bio-derived lignin through cost-effective measures. Key outcomes of this work are i) bio-materials such as lignin when combined with novel transition metal oxides such as $NiWO_4$ can show tremendous improvement in areal specific capacitance performance and retention in supercapacitor application and ii) through constituent optimization of biomaterials and nanoparticles, it is possible to obtain electrochemical performance of supercapacitors which is not only at par with the state-of-art but, in several cases, even better. This work marks an important step towards the development of green technology due to the usage of green sources for the raw materials and a method that is cost-effective.

4.5 Bimetallic Tungstate Nanoparticle-decorated-lignin Electrodes for Flexible Supercapacitors[*]

Bimetallic tungstates ($M_2M_1WO_4$; M= transition metal) are promising candidates for electrochemical energy applications. However, the effects of the secondary metal (M_2) on the pseudocapacitance behavior of bimetallic tungstates have not been well understood. We report, for the first time, the effects of secondary metal (Ni) on the pseudocapacitance of a bimetallic tungstate ($NiWO_4/CoWO_4$ composite called as $NiCoWO_4$ hereafter) when used in a quasi-solid-state supercapacitor. Nanoparticles of $NiCoWO_4$ and $CoWO_4$ were prepared using a wet chemical synthesis technique and characterized using SEM, XPS, XRD, EDX, and XPS. Lignin/$NiCoWO_4$//AC and lignin/$CoWO_4$//AC supercapacitors were electrochemically tested using Electrochemical Impedance Spectroscopy, cyclic charge-discharge, and cyclic voltammetry. After 2000

---

[*] Reprinted with permission from “Bimetallic tungstate nanoparticle-decorated-lignin electrodes for flexible supercapacitors” by Swarn Jha, Siddhi Mehta, Eugene Chen, Selvasundarasekar Sam Sankar, Subrata Kundu, Hong Liang, 2020. Materials Advances, 1, 2124-2135, Copyright [2020] by Royal Society of Chemistry.

charge-discharge cycles, the bimetallic tungstate ($NiCoWO_4$) functionalized lignin supercapacitor shows a specific capacitance (862.26 mF cm^{-2}, 96.12% retention) that is 141 times that of monometallic tungstate ($CoWO_4$) functionalized lignin supercapacitor. The lignin/$NiCoWO_4$ supercapacitor has very high power and energy densities of 854.76 kW kg^{-1} and 5.75 Wh kg^{-1} respectively due to a synergistic effect of bimetallic tungstate nanoparticles encapsulated in lignin. The supercapacitor design explored detailed aspects of composite electrode constituent optimization, and the effects of discharge time, lignin carbonization, and cathode material on the supercapacitor's performance. For an optimal mass ratio of lignin:$NiCoWO_4$:PVDF (15:75:10), the retention was 100% even after 2000 cycles. In addition to the cathode material's permittivity and surface area, the supercapacitor's electrochemical performance heavily depended on the dominant charge storage regime: an electric double-layer capacitor or pseudocapacitor dominant regime. This work provides new knowledge to design bimetallic tungstates based high-performance bioelectronics for advancing green technology.

4.5.1 Background

To meet the rising demands in energy storage and sustainability, there are impending needs to discover new high-performance eco-friendly materials [46, 86-89]. Electrochemical energy storage systems, like batteries and supercapacitors, are considered to be excellent options [9, 11, 12, 90-93]. Supercapacitors exhibit high performance using bio-derived materials and nanomaterials [94-96]. Recently, oxides/hydroxides based transition metals have garnered extensive attention in electrochemical applications [97-100]. But, these materials have poor cyclic stability, electroconductivity, and rapid capacitance degradation. The corrosion resistance and exceptional physiochemical properties of tungsten, combined with the non-toxic and stable multi-functional properties of the metal, make tungsten compounds an attractive choice [101]. Metal tungstates find applications in various fields, for instance, in optical fibers, photoluminescence, and microwave applications, which make them an integral part of the metal oxide family [102]. Metal tungstates with the empirical formula MWO_4 (M=Ni, Cu, Co, Mn) are particularly versatile and have found uses in Li-ion batteries and dielectric ceramics as well [103]. $CuWO_4$ crystals are frequently used in a variety of applications such as photo-electrocatalytic water oxidization or magnetism [104]. Precision in the bandgap energy of MWO_4 is highly crucial for several applications like the detectors used in the Large Hadron Collider at CERN and Raman lasers which are safe for eyes [105]. $CuWO_4$ nanoparticles (NP) were synthesized using a sonochemmagnetisical method which showed that the copper crystals are a favorable material for photocatalytic applications [106]. Feng et al., 2017 studied the electrochemical behaviors of $CoWO_4$, $NiWO_4$, and $CoWO_4$@$NiWO_4$-A and suggested that these metal tungstate compounds could be considered as good electrode materials for energy storage applications [107].

In the design of metal tungstates based electrodes, several aspects are crucially important for consideration: chemical structure, conductivity, charge transport mechanism, nature of transition metals, size, and temperature range of operation. Tungstates of transition metals such as Co, Ni, Cu, and Zn of the form MWO_4 (M = metal), except for $CuWO_4$, are found to possess the monoclinic wolframite-type structure. Wolframite structures (with Zn, Mg) have shown promising electrode material for dye-sensitized solar cells, while the scheelite structure (with Ca, Sr) operated with a lower electron transfer rate [108]. Hoang et al., 2018 carried out a hybrid density-functional analysis of the electronic structure and established that polaron formation of the underlying mechanism for the existence of p-type semiconductivity in $CoWO_4$ [109]. The conductance of $CuWO_4$ is attributed to the hopping of small polarons. In 2017, Hoang et al., 2017 conducted a first-principles study of Iron tungstate ($FeWO_4$) and manganese tungstate ($MnWO_4$) to attain a detailed understanding of their properties such as lattice parameters, static dielectric constants, and band gaps [110]. In their study, it was found that highly mobile polarons with low energy are formed near the band edges due to localized transition-metal d states. As a result, these materials exhibit high p-type conductivity. Also, WO_4 type transition metal tungstates (TMT) are associated with magnetic ordering due to which the conduction electrons have modified energy spectrum. This leads to a higher electrical resistivity in TMT than metals [111]. Montini et al., 2010 found that the nature of transition metal determines the photocatalytic and optical properties in MWO_4 type compounds. Despite having a huge bandgap, $ZnWO_4$ showed the highest photocatalytic activity possibly due to the hybridization of partially empty 3d orbitals with W5d orbitals that is in the lower level of the conduction band [112]. Perales et al., 2008 determined the bandgap energy (5.26 eV) in some tungstates (MWO_4) and reasoned that hybridization of p, d, and f electronic states of M^{2+} with the

O2p and W5p orbitals lowered the bandgap energy [105]. The size of the cation in the MWO_4 type determines the dielectric permittivity [113]. Nagirnyi et al. found that excitons were created as a result of the transition to W5d orbital in $CdWO_4$ at 6-300K and 3.5-3.0 eV. At energies, 1-2 eV higher than the conduction band energy, holes and free electrons were created due to the cation state transition [114]. The temperature range of application plays a fundamental role in the type of transition metal selection for electrodes. Below 455 K, hopping mechanism by small polarons lead to extrinsic type conduction behavior in $CoWO_4$, while, above 455 K, intrinsic behavior was observed due to large polaron hopping [111]. The A.C. and D.C. electrical conductance of manganese tungstate ($MnWO_4$) was measured in the given temperatures ranging from 300 K – 1250 K, and it was established that $MnWO_4$ showed a p-type behavior [115]. $NiWO_4$ is p-type under 660K, n-type between 660K to 950K and p-type above 950K. The dielectric constant of the observed $NiWO_4$ decreased with temperature from 300 K until 350 K. It increased slowly with temperature until about 700 K and increased rapidly after that [116].

Co and Ni are well complemented by each other, Co provides good rate capability and cyclic stability while Ni shows high specific capacitance (SPC). A hybrid tungstate of Ni-Co also shows better conductivity due to the incorporation of W atoms. Rajpurohit et al., 2019 prepared bimetallic Co-Ni tungstate NP and a composite with P-S co-doped graphene by hydrothermal synthesis and used as an electrode for supercapacitor [103]. Nickel-based materials possess high theoretical specific capacity but their low rate capability limits their use in supercapacitor applications. On the contrary, Cobalt-based materials possess good rate capability but possess a low specific capacity. Hence, a combination of these materials would possess the desired characteristics for use as positive electrodes in hybrid supercapacitors. In various studies of $NiWO_4$ and $CoWO_4$ electrodes, high SPC and retention were obtained. In one study, nanocomposites of $NiWO_4/CoWO_4$ were synthesized which showed high capacitive performance [101]. Co^{2+} was incorporated into the $NiWO_4$ lattice via a chemical co-precipitation method to manufacture monoclinic wolframite nanosheets of Ni_1-xCo_xWO_4. In comparison to $NiWO_4$, the surface area and the electrical conductivity of Ni_1-xCo_xWO_4 increased considerably. However, the $NiWO_4$ electrode exhibited better cycle stability. Based on the results obtained so far, it is predicted that the performance can be boosted by mixed transition metal oxides (MTMO) [101, 117]. Wang et al., 2016 used this reasoning to synthesize a mesoporous $NiWO_4$@$CoWO_4$ nanocomposite with different Co/ Ni molar ratios using a chemical co-precipitation method. It was determined that the supercapacitor fabricated by using this composite exhibited a high energy storage density of 30.1 Wh/kg and a higher power density of 200 W/kg [118]. A recent review focused on mixed transition metal oxides advancements and their hybridization with graphene sheets makes active materials for electrodes [119]. Critical factors affecting the electrochemical performance, as well as the low electroconductivity and other limitations of these oxides were highlighted. Graphene sheets hybridized with mixed transition metal oxides resulted in a high specific surface area and good electroconductivity. The mixed transition metals oxides (MTMO’s), in comparison to transition metal oxides (TMO), exhibit better electrochemical properties. This can be attributed to the combined effect of multiple oxidation states in transition metal oxides which give an ideal pseudocapacitance due to the diverse redox reactions. The number of electroactive sites and electrolyte ion accessibility plays a major role in the performance of the electrochemical system along with the porosity, specific surface area, and morphology of the active material [120]. The combined effect of two different TMO's increase the number of electroactive sites as well as the potential window. Combined with their low-cost, abundant availability and eco-friendliness, make MTMO's excellent candidates for active electrode materials. Despite the superior electrochemical performance, MTMO's have several limitations as well. These include poor cyclic stability, rate capability as well as intense volume expansion during the reversible charge-discharge process. To improve this, MTMO are customized into nanostructures [119].

Over the years there have been significant advancements in the synthesis of metal tungstates and tungsten oxides. $CuWO_4$ was synthesized by the chemical precipitation method and the parameters were optimized using a Taguchi robust design. The method did not use templates or catalysts which made it very simple and fast in comparison to other methods [121]. Zawawi et al., 2013 executed the synthesis of three separate metal tungstate phases through the sucrose templated method. The phase achieved by each metal tungstate, and the relationship between bivalent cation size and the structural properties were dependent on the divalent cation has been used [122]. Priya et al., 2011 used a co-precipitation method to synthesize $CdWO_4$ crystals. Increasing temperature and frequency was found to have a positive correlation on the electrical conductivity, thus, demonstrating the semiconducting nature of the material [102]. One notable and simple process is the microwave synthesis of a nano-crystalline metal tungstate, investigated through the use of radiation from a cyclic microwave and the organic compound propylene glycol [123]. Parhi et al., 2008 used a microwave to synthesize metal tungstates using a solid-state metathetic (SSM) method [124]. It was found that reaction time, pH, and temperature strongly influenced the synthesis of the single-crystal nanowire of silver tungstates using hydrothermal re-crystallization [125]. Talebi et al., 2016 synthesized $NiWO_4$ NP using the ultrasound method and used it to study the photocatalytic degradation of methyl orange [126]. Shinde et al., 2020 explained the pH-and potential dependent behavior of tungsten in an aqueous medium, as well as the tungsten oxide crystal structures [127]. Various tungstate trioxide-based materials have been synthesized and tested extensively. However, tungstate trioxide has a low energy density and surface area. Therefore, more research is required to enhance their performance as active electrode materials [127]. Wet chemical synthesis is one of the widely used techniques for the synthesis of NP, which commonly deals with the chemical reactions occurring in its solution phase. Of the many methods available for the synthesis of NP such as solvothermal and template synthesis, oriented attachment, self-assembly, etc., the wet chemical synthesis method offers a high degree of material reproducibility and controllability. The uniformity of the produced compounds is also ensured by this route [128, 129]. Recently, lignin-based carbon materials have shown promising activity in supercapacitors [62, 92]. However, challenges exist in terms of achieving high power and energy densities, cyclic stability, and long term cyclic stability for application purposes. Besides, the state-of-art use of lignin emphasizes the use of hazardous processes such as using polyacrylonitrile (PAN) based fibers, or expensive and unsafe techniques like electrospinning. As such, there is a need to design and develop new lignin-based material and process that is efficient, safe, and reliable for use.

The objectives of this research are: 1) to understand the effect of the secondary metal (Ni) in the bimetallic tungstate composite ($NiCoWO_4$) in affecting its electrochemical behavior, 2) to assess and optimize the performance, and layout design strategy for a synergistic design of the bimetallic tungstate NP functionalized lignin-based supercapacitors based on green chemistry principles. To attain these objectives, a bimetallic tungstate NP functionalized alkali lignin (lignin/$NiCoWO_4$) based supercapacitor is designed. It is then compared for electrochemical performance with a metallic tungstate nanoparticle functionalized alkali lignin (lignin/$CoWO_4$) based supercapacitor. The $NiCoWO_4$ and $CoWO_4$ NP were prepared by using a wet chemical synthesis technique. NP characterization was done using XRD, XPS, EDX, and SEM. A supercapacitor study was done by using the electrochemical tests mentioned earlier. Effects of the secondary metal (Ni) in the bimetallic tungstate, discharge time, carbonized alkali lignin, and cathode material were investigated. The design strategy explored in detail the aspects of composite electrode constituent optimization, and the effects of discharge time, lignin carbonization, and cathode material on the super capacitance performance.

4.5.2. Experimental

Synthesis of $CoWO_4$

For this synthesis procedure, a simple wet chemical route was opted. 0.05 M of cobalt acetate salt was added to distilled water (50 ml) and stirred for 15 min; this solution was denoted as the solution A. Likewise, 0.1 M of Na_2WO_4 salt is mixed with 100 ml of DI water, which was then stirred for 30 min which was labeled as solution B. After that, solution A was added dropwise to solution B, followed by stirring it for 6 h. A pink colored precipitate was formed which was centrifuged and dried.

Synthesis of Ni-$CoWO_4$

The mixture of Ni, Co bimetallic tungstate was prepared via a wet chemical approach. Wherein, 0.9 g of nickel acetate was mixed with 50 ml of water (distilled) and the solution was stirred for 15 min until the homogeneity was observed. This solution was denoted as Solution A. 0.3 g of cobalt acetate was added to 50 ml of DI water in a beaker and stirred for 15 min. This solution was denoted as solution B. Likewise, 0.1 M Na_2WO_4 was added to DI water (100 ml) and then stirred for 30 min. This was labeled as solution C. Finally, solutions A and B were mixed dropwise on to solution C simultaneously. The resultant solution was stirred for 6 h under magnetically stirred condition. After that, the solution was centrifuged and dried. The final product was collected and annealed at 600 ºC for 2 h with a temperature ramping rate of 5º C min^{-1}. The end product was denoted as Ni-CoWO$_4$.

Fabrication of the lignin/Ni-CoWO$_4$ and CoWO$_4$ Composite Electrodes

To study the novel NP, three ratios of varying wt.% were synthesized and analyzed via electrochemical testing. The ratios were prepared in the form Lig:Ni-CoWO$_4$:PVDF. The first sample was prepared in the ratio of 80:10:10. 0.015 g of novel Ni-CoWO$_4$ NP were added to 0.12 g alkaline lignin (TCI Chemicals). A slurry of the obtained compound was made by using polyvinylidene difluoride (PVDF) as the binder and 3 ml of NMP (N-Methyl-2-Pyrrolidone) as the solvent, both obtained from Sigma Aldrich. An aluminum foil of diameter 40 mm, 0.98 mm thick, and with adjacent strips of 10 mm × 30 mm was used as the substrate. The slurry obtained earlier was coated on the Al substrate. The coated substrate was thermally treated at 70˚C in a vacuum environment of -21 Hg vacuum pressure. Similarly, the other two samples of the ratios 75:15:10 and 15:75:10 were made and studied to arrive at the optimal performance. The same method was implemented to synthesize the CoWO$_4$ electrode of the ratio 80:10:10 and NiWO$_4$ electrode of ratio 10:80:10 [92]. Regarding the fabrication of the electrolyte, the PVA/H$_3$PO$_4$ electrolyte gel was prepared in the same manner as explained in our recently published work [92, 130]. For carbonized lignin, a carbonization procedure was done: alkali lignin was heated at 300-400^{0}C in an argon atmosphere for 24 hours. The remaining fabrication process was the same as for the alkali lignin-based supercapacitor.

Assembly of the asymmetric supercapacitors

Two supercapacitor assemblies with different negative electrodes were prepared as shown in Fig.-4.9. The negative electrodes were Al foil coated with activated carbon (AC) and a graphene sheet. Porous commercial paper was used as a separator in the supercapacitor assembly. The paper was completely immersed in the PVA/H_3PO_4 electrolyte gel. The separator was then placed on the lignin-based composite electrode. The negative electrode was placed over the separator, effectively sandwiching the separator between the two electrodes to form the asymmetric supercapacitor assembly. The schematic is shown in Fig. 4.9.

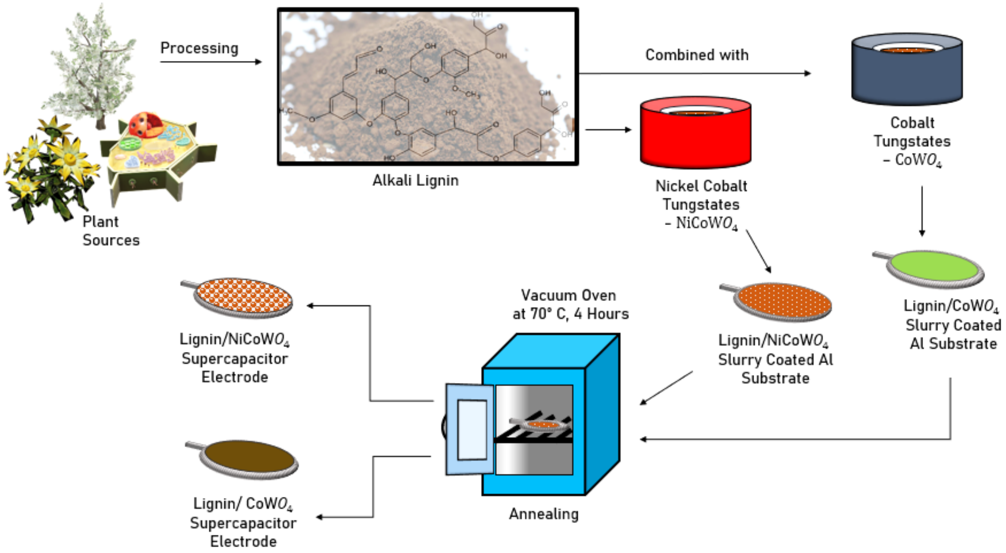

Fig. 4.9 Schematic for the fabrication of the composite electrodes.

Characterizations

XPS was studied using a Theta Probe AR-XPS system (Thermo Fisher Scientific, UK). For the XRD evaluation, a Bruker X-ray diffractometer was used. A sweeping rate of 5° min^{-1} (2θ range 10-90°) and λ = 0.154 nm (Cu K_α radiation) was implemented. The

Hitachi model S-3000H with a 30X to 300 kX magnification and an accelerating voltage ~ 0.3 to 30 kV was used for the EDS as well as SEM evaluation. The Olympus Leco PMG3 optical microscope (OM) at the Texas A&M Materials Science Engineering Facility was used to obtain high contrast images. The interferometer model was a Zygo NewView 600 type (Zygo Corporation, CT). All electrochemical characterizations were performed with a Gamry version 6.33 potentiostat (Gamry Instruments, USA). EIS was carried in the frequency range 10^6 - 0.1 Hz, and AC of 1V.

4.5.3 Results and discussion

X-ray diffraction (XRD) pattern of nanoparticles

To understand the nature exhibited by the materials, XRD studies were carried out. XRD studies reveal that $CoWO_4$ exhibits semi-crystalline in nature. There are some sharp peaks observed and these peaks correspond with the JCPDS number 00-015-0867 which reveals the formation of $CoWO_4$. The distinct peak observed at the position of 35.7º corresponds to the oxide of tungsten. The corresponding XRD spectrum is shown in Fig. 4.10(a).

The synthesized Ni-$CoWO_4$ powder was subjected to X-ray diffraction studies (XRD). The subsequent XRD spectrum is shown in Fig. 4.10(b). The sharp peak reveals the

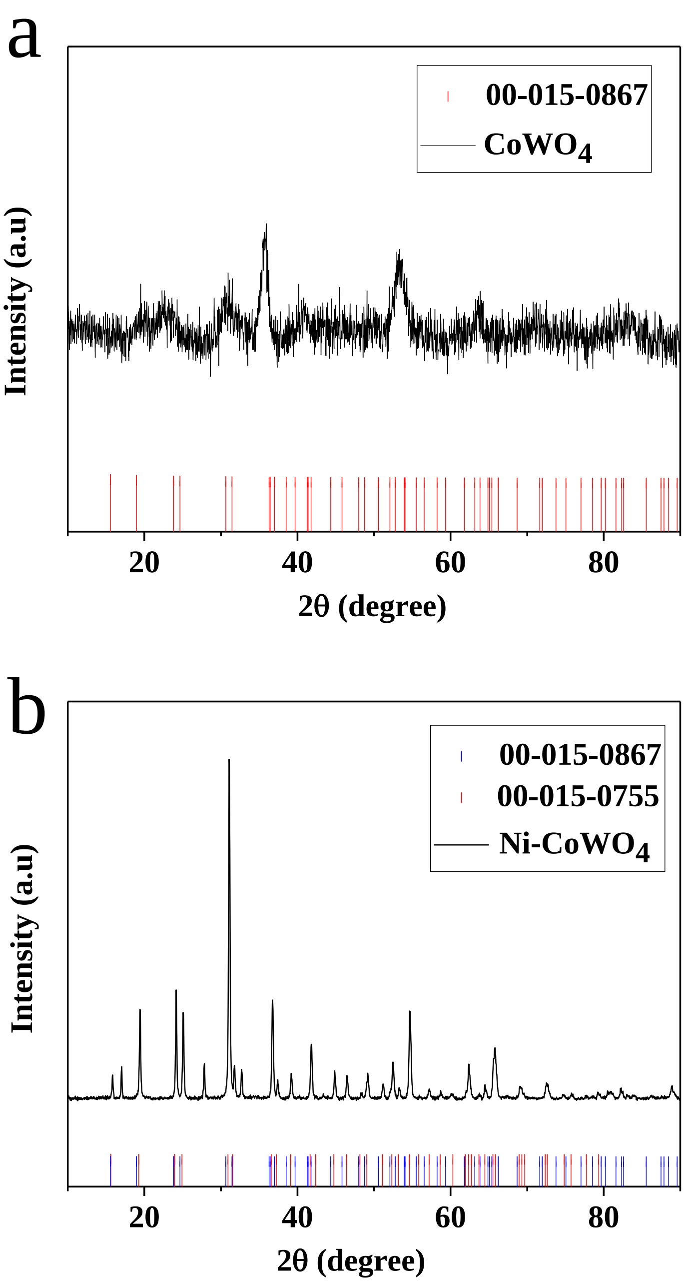

Fig. 4.10 XRD plots for the composite electrodes: (a) $CoWO_4$, and (b) Ni-$CoWO_4$.

formed materials are crystalline. This pattern exactly matches the JCPDS reference number of 00-015-0867 and 00-015-0755 which corresponds to a mixture of cobalt and nickel tungstate respectively. Other distinct peaks of 17.09, 27.88, and 32.73º correspond to tungsten oxides (W_xO_y) which is a match with the PDF number of 00-005-0392.

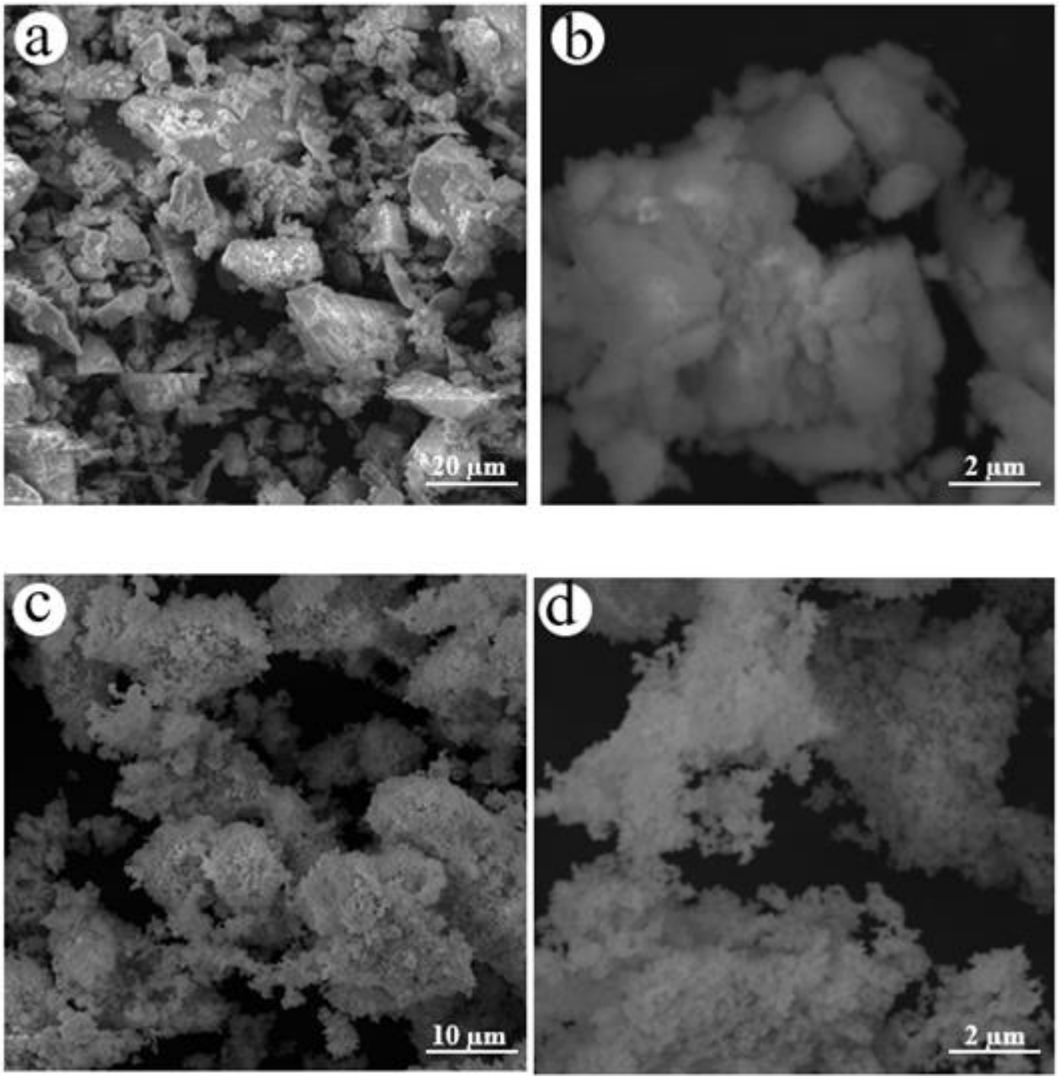

Fig. 4.11 SEM images for (a) $CoWO_4$ (low magnification), (b) $CoWO_4$ (high magnification), (c) $NioCoWO_4$ (low magnification, and (d) Ni-$CoWO_4$ (high magnification).

Scanning electron microscope (SEM) images of nanoparticles

To know the morphological aspects, scanning electron microscope (SEM) analysis was performed and the subsequent images are displayed in Fig. 4.11(a-d).

The high and low magnification images of $CoWO_4$ (Fig. 4.11(a-b)), shows a disordered plate-like morphology. The high magnification and low magnification images of Ni-$CoWO_4$ can be seen in Fig. 4.11(c-d) respectively. In both cases, the observed materials are uniformly distributed all over the surface.

a

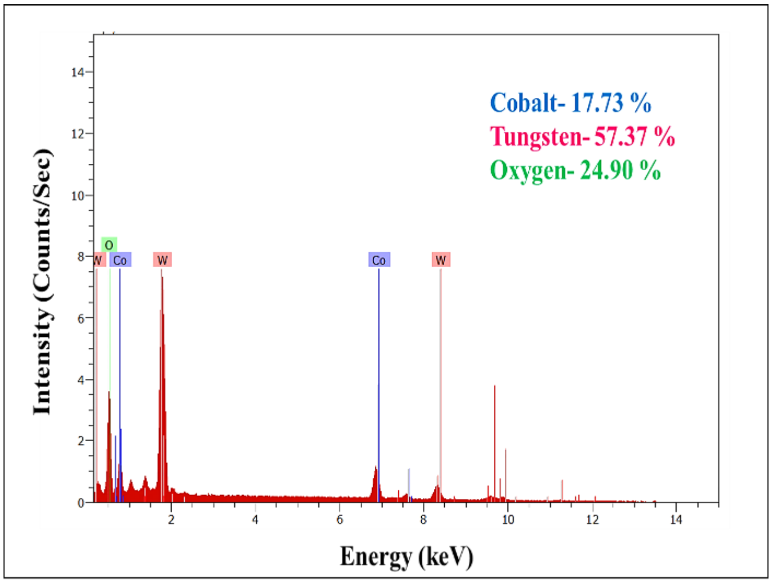

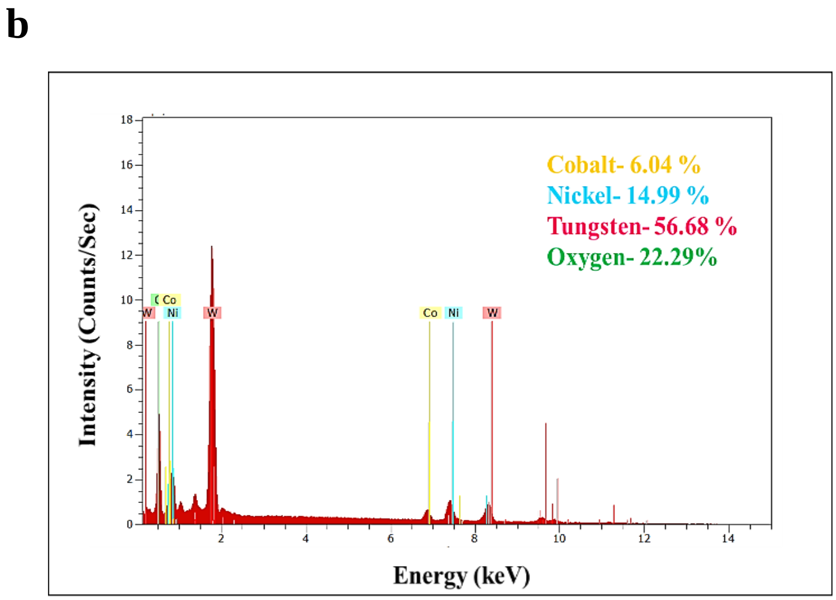

Fig. 4.12 EDS analysis for (a) $CoWO_4$, and (b) Ni-$CoWO_4$ nanoparticles.

Energy-dispersive X-ray (EDS) spectroscopy analysis of nanoparticles

To confirm the elemental composition, EDS was carried out. The corresponding plots are shown in Fig. 4.12(a-b). The observed elements like cobalt, tungsten, and oxygen in $CoWO_4$ have been confirmed in Fig. 4.12a. The presence of elements in $NiCoWO_4$ such as nickel, cobalt, tungsten, and oxygen have been confirmed; the corresponding EDS spectrum is shown in Fig. 4.12b.

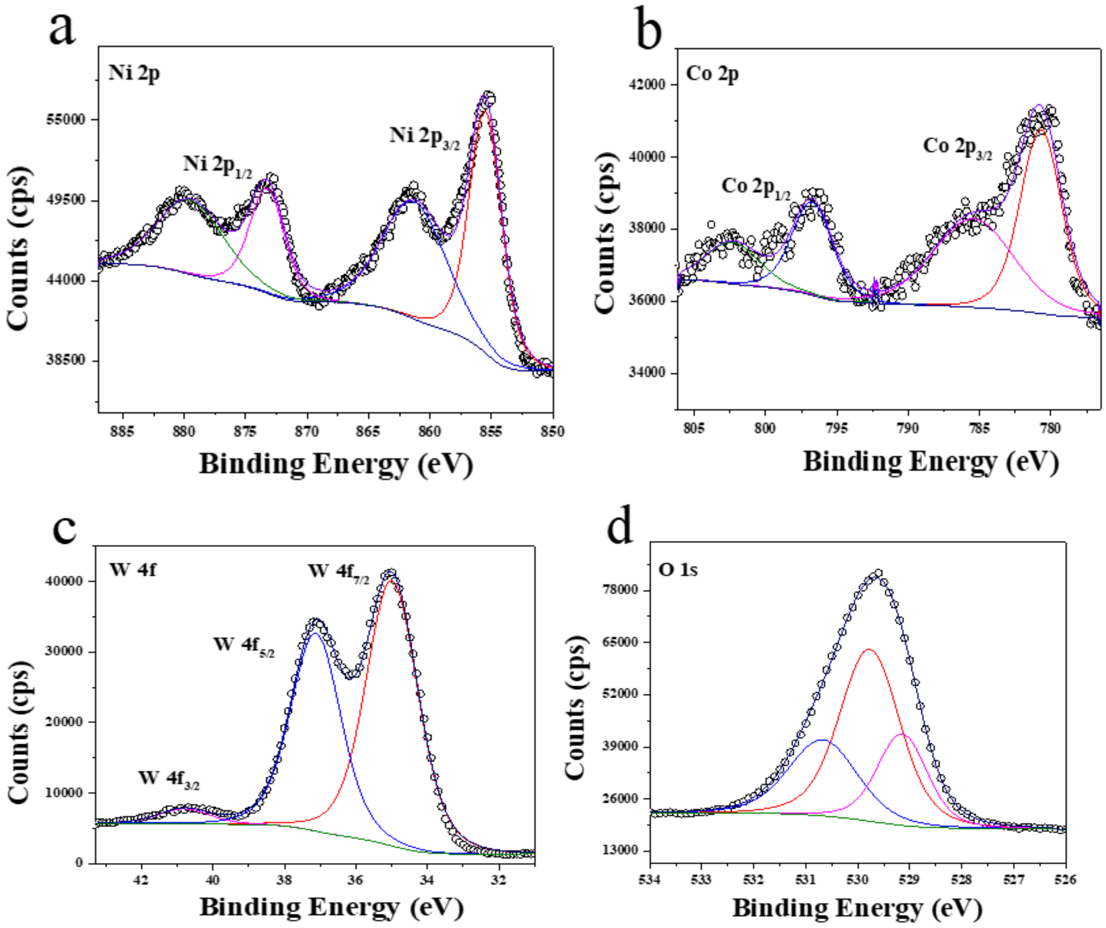

Fig. 4.13. XPS Spectrum for (a) Ni 2p, (b) Co 2p, (c) W 4f, and (d) O 1s.

X-ray photoelectron spectroscopy (XPS) of nanoparticles

For identifying the nature of the elements, X-ray photoelectron spectroscopy (XPS) was carried out. Fig. 4.13a shows the high-resolution XPS spectrum of Ni 2. Herein, the binding energy values are observed at 873.3, 855.5 eV and 879.7, 861.54 eV corresponding to Ni 2p1/2, and Ni 2p3/2 and the corresponding satellite peaks respectively. Similarly, Fig. 4.13b the high-resolution spectrum of Co 2p shows the binding energy values of 796.74, 780.86 eV, and 802.46, 785.64 eV, corresponds to Ni

2p1/2 and Ni 2p3/2 and corresponding satellite peaks respectively. Both nickel and cobalt possess an oxidation state of +2. Fig. 4.13c is the high-resolution spectrum of W 4f where the observed binding energies are 40.82, 35.02, and 37.15 eV corresponding to W 4f 3/2, W 5p 7/2, and W 4f 5/2 respectively. The high-resolution spectrum of O 1s shows corresponding peaks at 529.17, 529.7, and 530.7 eV which signifies the metal oxide bond and the lattice oxygen of the material. The corresponding spectrum is shown in Fig. 4.13d.

Electrochemical performance

To understand the effect of the secondary metal (M_2) of a bimetallic tungstate on its pseudocapacitance behavior, the electrochemical performance of a bimetallic tungstate ($M_2M_1WO_x$, M_2= Ni, M_1= Co, X= 4) was compared to that of a metal tungstate (M_1WO_x, M_1= Co, X= 4). For this, two cyclic charge-discharge (CCD) experiments (current density = 0.8 mA cm^{-2}, 2000 cycles, AC cathode) were performed: one having lignin/$NiCoWO_4$ as the composite anode, and the other having lignin/$CoWO_4$ as the composite anode. As observed in Fig. 4.14(a-b), the initial and final areal SPC for the lignin/$NiCoWO_4$ pseudocapacitor (1st cycle SPC = 862.26 mF cm^{-2}, 2000th cycle SPC = 828.82 mF cm^{-2}) are 141 and 1726 times higher, respectively, than that of lignin/$CoWO_4$ pseudocapacitor (1st cycle SPC = 6.1 mF cm^{-2}, 2000th cycle SPC = 0.48 mF cm^{-2}). Thus, it is observed that the areal SPC of lignin/$NiCoWO_4$ is consistently higher than that of lignin/$CoWO_4$ pseudocapacitor. Also, the final retention (Fig. 4.14b) for the lignin/$NiCoWO_4$ supercapacitor (96.12%), is 12.16 times of the lignin/CoWO4 supercapacitor (7.90%). Similarly, the SPC of lignin/$NiWO_4$ supercapacitor for the best ratio (10:80:10), is 32.90 mF cm^{-2} (98.2% retention, 2000 cycles), that is 26.20 times smaller than that of lignin/$NiCoWO_4$ supercapacitor. Thus, the secondary metal (Ni) of the bimetallic tungstate ($NiCoWO_4$), has a tremendous effect in enhancing both the SPC and retention. This enhanced performance can be attributed to a synergistic effect of a highly disordered plate-like morphology (Fig. 4.14(c-d)) of the bimetallic tungstate NP, obtained through our wet chemical synthesis approach, that provides enhanced surface area for electrochemical reactions; multiple available oxidation states of the transition metals (Ni and Co) resulting in a range of redox reactions leading to higher electronic conduction and charge transport; higher access of electrolyte ions and electroactive sites due to inherent defects in lignin matrix; and a high surface area (S) to volume (V) ratio (S/V) of the NP due to nanostructuring. These results overcome the limitations of poor cyclability and performance stability of earlier works [119].

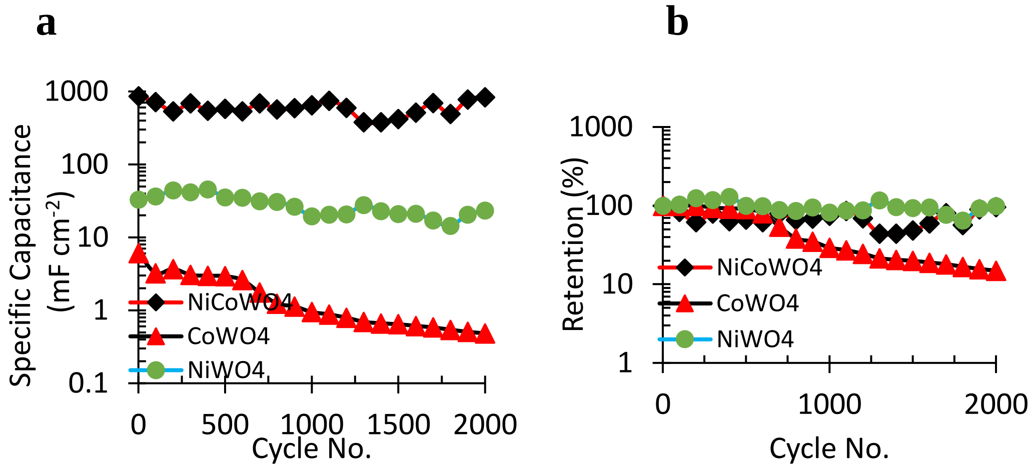

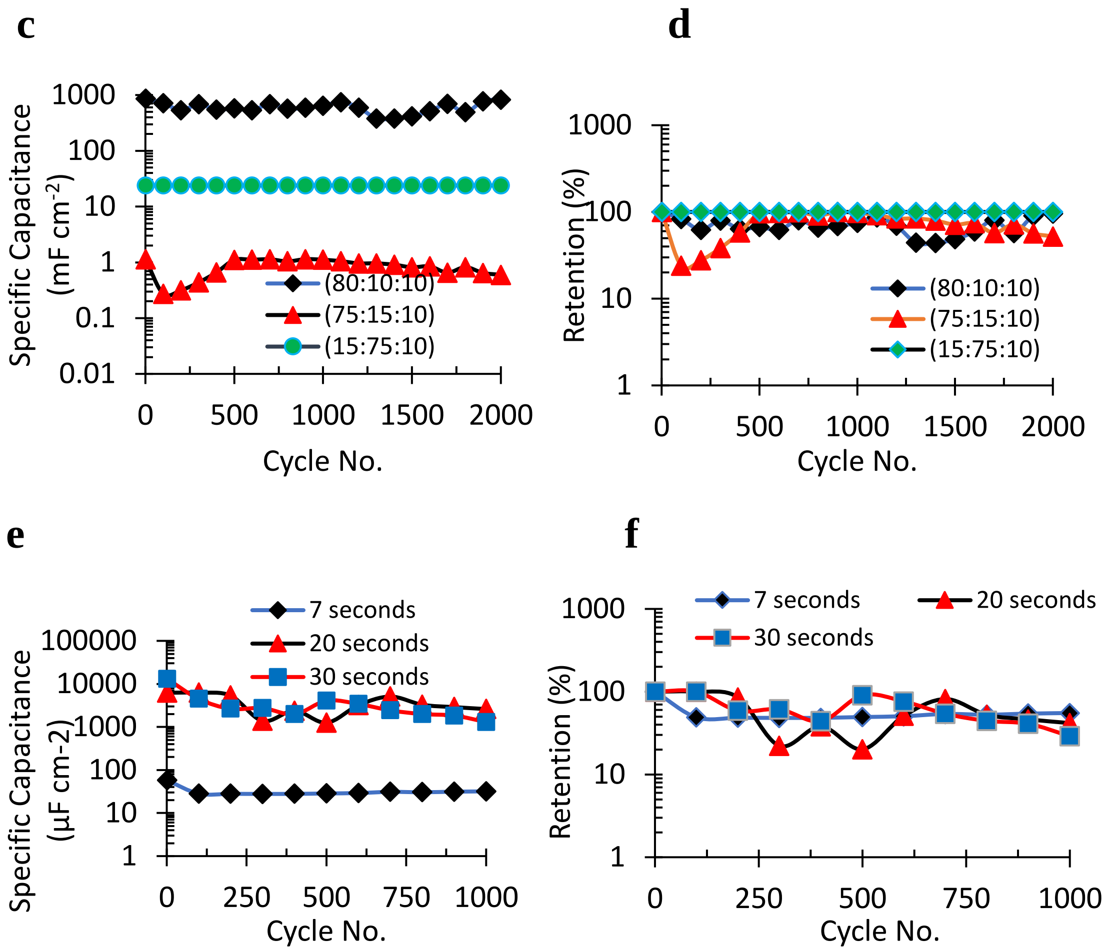

Fig. 4.14. CCD plots for: the specific capacitance (a) and retention (b) for the lignin/NiCoWO$_4$ and the lignin/CoWO$_4$ supercapacitors with a constituent ratio of 80:10:10 in each and the best ratio 10:80:10 of lignin/NiWO$_4$; specific capacitance (c) and retention (d) under varying mass loadings for the lignin/NiCoWO$_4$ supercapacitor; the specific capacitance (e) and retention (f) under varying discharge times for the lignin/NiCoWO$_4$ supercapacitor with a constituent ratio 75:15:10.

The effects of different constituent mass ratios of the lignin/NiCoWO$_4$ composite electrode on the electrochemical performance of the pseudocapacitor were studied. This is important to ascertain the contribution from individual constituents (in this case: lignin, $NiCoWO_4$ NP, and PVDF) to the electrochemical performance which enables the effective design of pseudocapacitor. Accordingly, three different constituent weight ratios of the composite electrode in the order lignin:$NiCoWO_4$:PVDF were used and tested in cyclic charge-discharge experiments for 2000 cycles (Fig. 4.14(c-d)). Of the three samples, sample 80:10:10 has the consistently highest SPC with a maximum value of 862.26 mF cm^{-2}. When the relative percentage of lignin was reduced (sample 75:15:10), compared to sample 80:10:10, the SPC dropped by 416 times (1.14 mF cm^{-2}). On the other hand, when the relative percentage of $NiCoWO_4$ NP was significantly increased to 75% by weight (sample 15:75:10), compared to sample 75:15:10, the SPC increased by 21 times (23.87 mF cm^{-2}). Thus, the effect of lignin is predominant in affecting the SPC of the pseudocapacitor; and the SPC reduces on reducing the relative weight percent of lignin. This is so because, with a reduction in lignin, the number of active sites is reduced which lowers the charge storage capability of the electro-active material. In comparison, when the relative percentage of NP is increased, there is an enhancement in the pseudocapacitance due to an increased oxidation-reduction site leading to enhanced charge storage by the active material. However, this change in SPC due to the NP is less pronounced than due to lignin. The retention plot (Fig. 4.14d) reveals that with a high percentage of NP (sample 15:75:10), capacitance retention is the highest (100%). This is on account of the pseudocapacitance property of the NP. Retention of other samples drops since the active sites on lignin get consumed with the progression of cycles. Thus, the mass ratio experiment reveals that while a higher percentage of lignin is required for achieving high SPC, a high relative percentage of NP is required for attaining high capacitance retention. An optimal value of these constituents can meet the requirement for a high SPC and retention.

The electrochemical performance of a supercapacitor, against varying discharge times (Fig. 4.14(e-f)), gives an indication of its usability under varied load conditions. The conventional discharge time of a supercapacitor may lie in the range of 1-30 s [131]. To maximize the energy density of a supercapacitor, it is desired that a supercapacitor can deliver sustained high performance for a longer discharge time. But, at higher discharge times, the cycle life of a supercapacitor is curtailed. This is due to the more rapid consumption of the active sites and a faster generation of decomposition side products that adversely affect its charge storage ability. Thus, the challenge is to obtain a high and sustained electrochemical performance for a longer discharge time. To this effect, the capacitance performance of lignin/$NiCoWO_4$//Graphene supercapacitor was evaluated corresponding to the discharge times of 7, 20, and 30 s. The constituent weight ratio (lignin:$NiCoWO_4$: PVDF) was 75: 15:10 in each case. It was observed that the average SPC at 7 s (Fig.-4.14(e-f)) was the least, and for 30 s, it was the highest of the three. At the end of 1000 cycles, the SPC for 20 s (2.6 mF cm^{-2}) was twice that at 30 s (1.3 mF cm^{-2}). Also, the final retention followed the trend 30s < 20s < 7s. However, the difference in the retention between the highest (7 s) and the lowest (30 s) was only about 11%. Thus, the bimetallic tungstate NP supercapacitor can perform appreciably well even at high discharge times. When the supercapacitor is made to discharge for a longer time, it engages more redox-active sites leading to a larger charge transfer accountable for a higher SPC (as at 30 s). However, higher engagement of the redox-active sites, at longer discharge times, also leads to a faster depletion of newly available redox sites due to reaction products. Thus, at longer discharge times (as at 30 s), the supercapacitor has, gradually, a lower ability to store or transfer charge due to lower availability of new redox-active sites for charge transfer. This leads to poor retention at higher cycles.

The 3D network of carbon chains in lignin molecules plays a big role in impacting its capacitance property. It is intriguing to know how electrochemical performance is affected when these molecular chains are broken into smaller fragments. The carbonization of lignin breaks the long carbon chains in lignin into smaller fragments. It also induces some degree of oxidation. To understand the effect of smaller fragments of lignin structure and partially oxidized lignin on its capacitance performance, the electrochemical performance of carbonized lignin/$NiCoWO_4$ was assessed with graphene cathode. It is observed, in Fig. 4.15a, that the SPC of carbonized lignin/$NiCoWO_4$ (1^{st} cycle SPC = 38.09 mF cm^{-2}, 2000th cycle SPC = 5.08 mF cm^{-2}) is consistently low compared to non-carbonized lignin/$NiCoWO_4$ (1^{st} cycle SPC = 474.68 mF cm^{-2}, 2000th cycle SPC = 456.68 mF cm^{-2}). Thus, the initial and final values of SPC of the carbonized lignin/$NiCoWO_4$ are only 8% and 1.2% of that of non-carbonized lignin/$NiCoWO_4$ respectively. The final retention of carbonized lignin/$NiCoWO_4$ in Fig. 4.15 b is 29% of that of non-carbonized lignin. Thus, the electrochemical performance of carbonized lignin is inferior to that of non-carbonized lignin. This can be explained by the fact that with the fragmentation of larger lignin chains into smaller chains in carbonized lignin, there is a considerable increase in disorder in chain structure and arrangement. This leads to a greater impedance to charge transfer resulting in a lesser charge storage ability by the carbonized lignin. Also, carbonized lignin has a greater number of unreactive constituents which do not contribute to any capacitance. This results in a faster fading of capacitance.

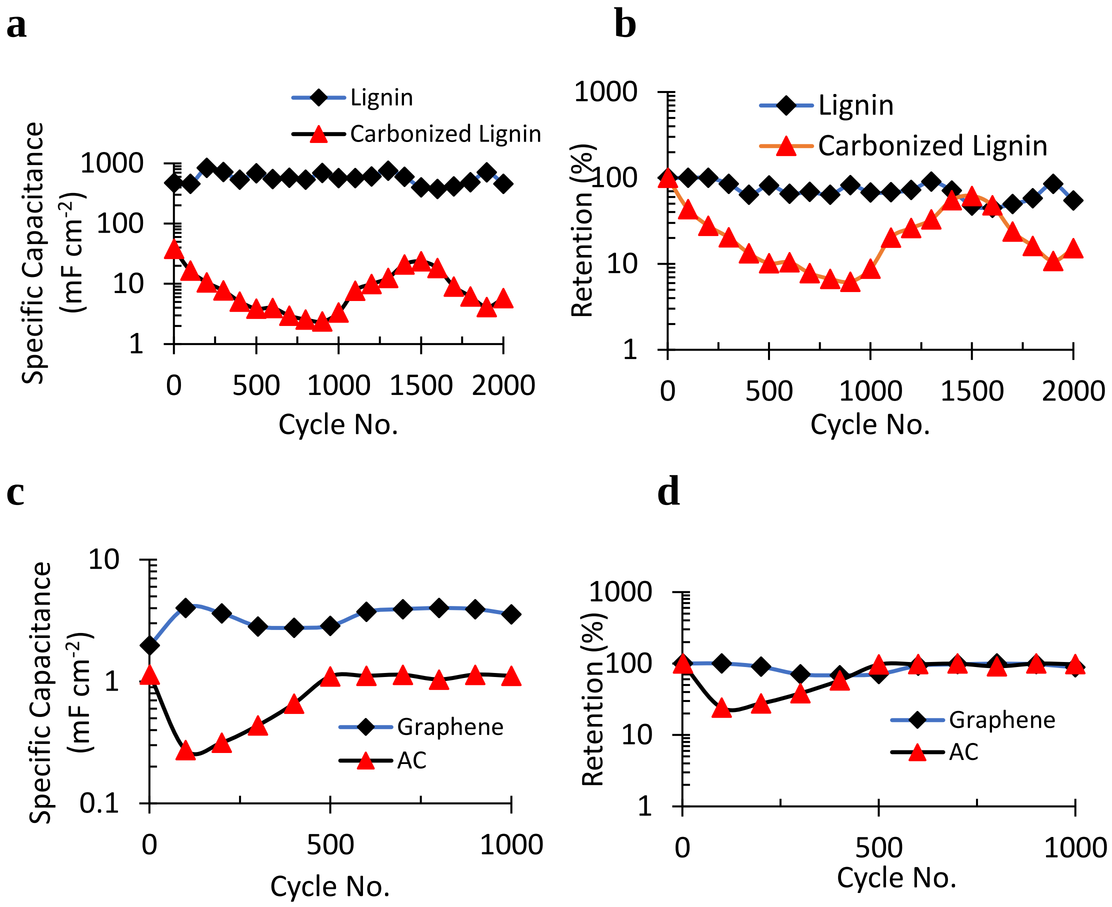

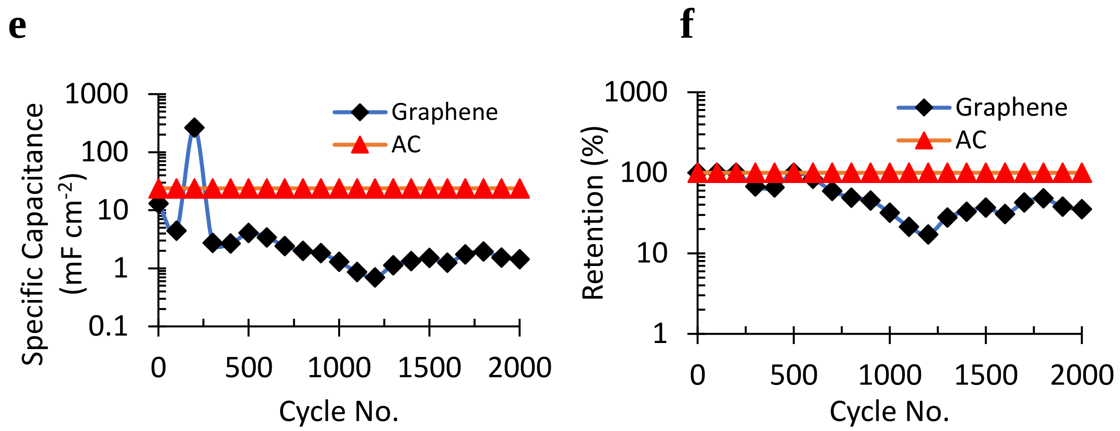

Fig. 4.15. CCD plots for the effect of carbonization on the specific capacitance (a) and retention (b) of the 75:15:10 supercapacitor; the effect of the negative electrode on the specific capacitance (c) and retention (d) of the 75:15:10 supercapacitor; the effect of the negative electrode on the specific capacitance (e) and retention (f) of the 15:75:10 supercapacitor.

The type of cathode material, its conductivity, and surface characteristics play a critical role in a supercapacitor design. The influence of the negative electrode on the electrochemical performance of the bimetallic tungstate supercapacitor was analyzed (Fig. 4.15 (c-f)) and it revealed some interesting trends. Two sets of experiments were done: in experiment set I (Fig. 4.15 (c-d)), lignin:$NiCoWO_4$:PVDF mass ratio was 75:15:10, while in the experiment set II (Fig. 4.15 (e-f)), it was 15:75:10. Thus, in experiment set I, the capacitance was electric double-layer capacitor (EDLC) type dominated (due to higher proportion of lignin) and it was pseudocapacitance dominated in experiment set II (due to a higher proportion of $NiCoWO_4$) [132]. It was observed that in the EDLC dominated regime (experiment set I), the SPC of the supercapacitor, with graphene as the negative electrode (4.03 mF cm^{-2}), was 3.5 times that with AC as the negative electrode (1.14 mF cm^{-2}). This can be explained based on a higher value of the dielectric constant of graphene [133, 134] compared to that of AC [135] which accounts for a higher SPC (Capacitance, $C = \epsilon A/d$, A= contact surface area, ϵ = dielectric constant, d= distance between electrodes) [136] in an EDLC dominated regime. On the contrary, in the pseudocapacitance dominated regime (experiment set II), there is a greater degree of charge transfer and storage due to the pseudocapacitance behavior of the $NiCoWO_4$ NPS, in addition to the EDLC behavior of lignin. The pseudocapacitance charge transfer heavily depends upon the available contact surface area of the electrode-electrolyte at both electrodes of the supercapacitor. Since the AC electrode has a much higher available surface area (A) than the graphene electrode, therefore, there is 1.8 times higher charge transfer and storage in case of AC electrode (23.88 mF cm^{-2}) compared to the graphene electrode (13.13 mF cm^{-2}) in the experiment set II. In this case, the higher pseudocapacitance charge transfer contribution in the AC electrode, due to its higher surface area, overpowers the effect of a greater dielectric constant of the graphene electrode. Thus, the electrochemical performance of the bimetallic tungstate supercapacitor was found to be heavily dependent not only on the choice of the negative electrode but also on the type of dominant regime of charge storage i.e., EDLC dominated or pseudocapacitance dominated regime.

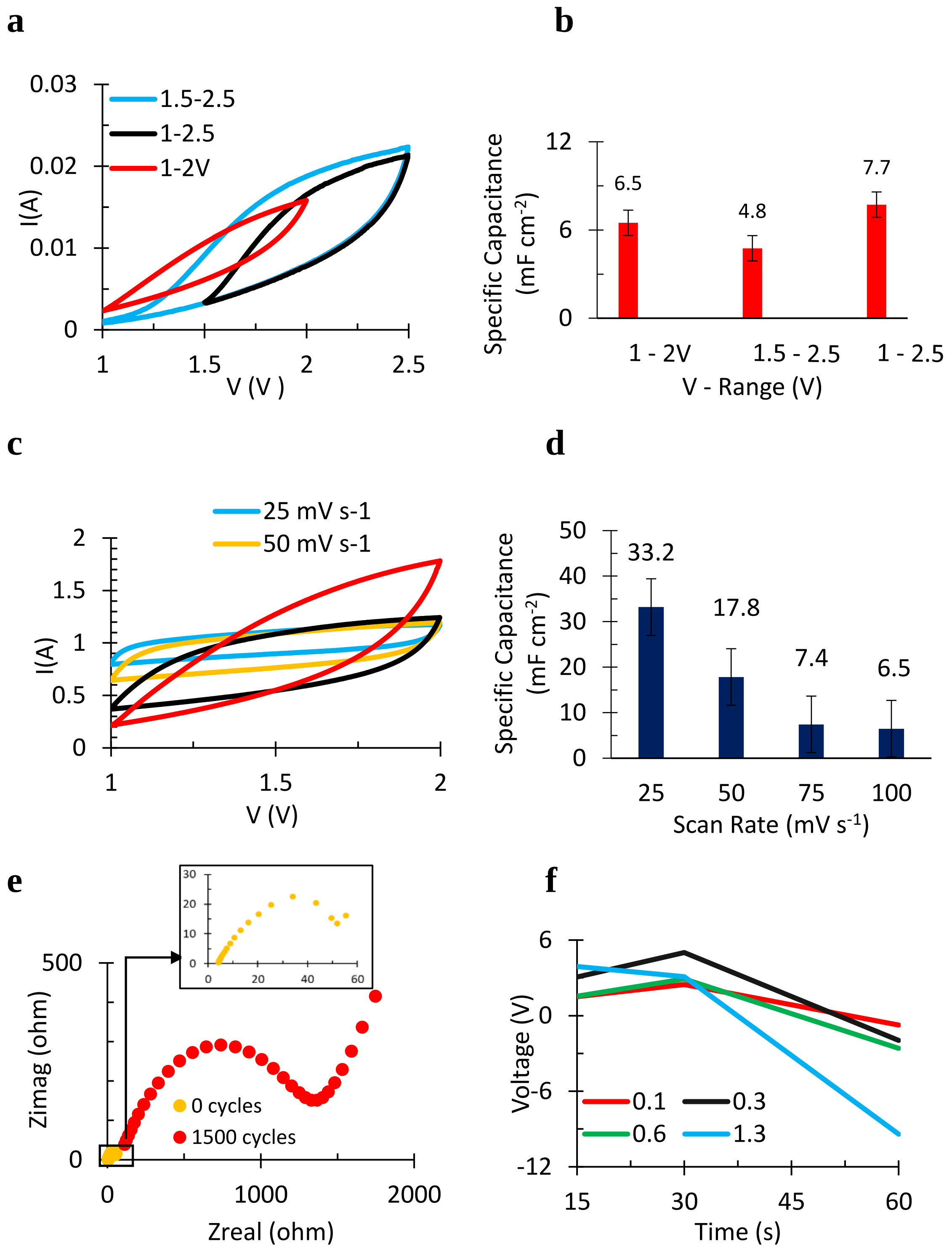
a
0.03
0.02
0.01
0
I(A)
1.5-2.5
1-2.5
1-2V
1
1.5
2
2.5
V (V)
b
12
6
0
Specific Capacitance (mF cm^{-2})
6.5
4.8
7.7
1 - 2V
1.5 - 2.5
1 - 2.5
V - Range (V)
c
2
1.5
1
0.5
0
I(A)
25 mV s-1
50 mV s-1
1
1.5
2
V (V)
d
50
40
30
20
10
0
Specific Capacitance (mF cm^{-2})
33.2
17.8
7.4
6.5
25
50
75
100
Scan Rate (mV s^{-1})
e
500
0
Zimag (ohm)
30
20
10
0
0
20
40
60
0 cycles
1500 cycles
0
1000
2000
Zreal (ohm)
f
6
0
-6
-12
Voltage (V)
0.1
0.3
0.6
1.3
15
30
45
60
Time (s)

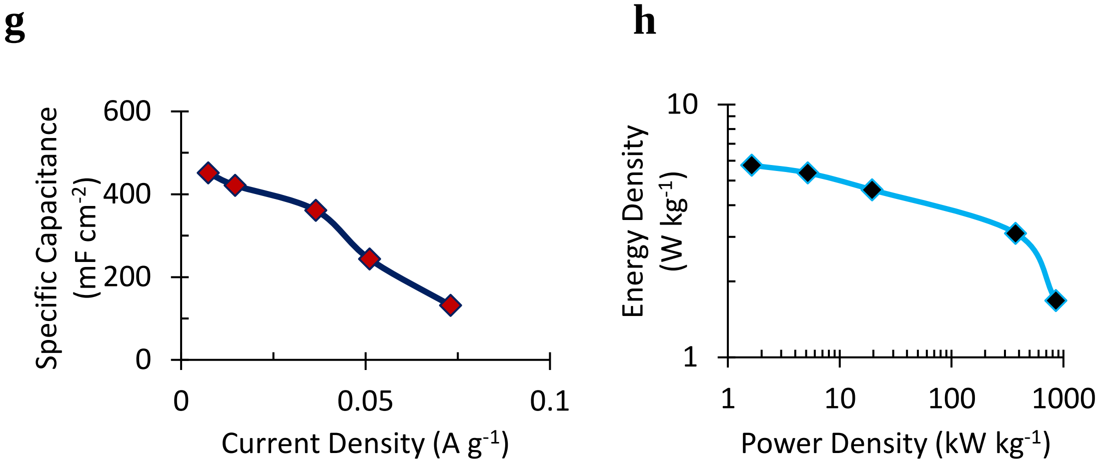

Fig. 4.16. For the lig-Ni-$CoWO_4$, CV plots for different potential windows (a) and at different scan rates (c); specific capacitance variation with voltage windows (b) and scan rates (d); Nyquist plot (e); V vs. T plot (f) at varying current density (A g^{-1}); variation of specific capacitance with current density (g); and the Ragone plot (h).

To determine the optimal voltage window for the lignin/$NiCoWO_4$ supercapacitor (15:75:10), it was subjected to cyclic voltammetry (CV) as seen in Fig. 4.16 a. The CV curves in the range 1-2 V and 1.5 – 2.5 V are more rectangular compared to the 1- 2.5 V curve, thus, resembling a capacitor behavior more closely. A larger SPC (Fig. 4.16 b) value of 6.5 mF cm^{-2} (for 1-2V) compared to 4.8 mF cm^{-2} (for 1.5-2.5V), suggests that 1-2V is an optimal voltage range of operation. Accordingly, the supercapacitor was cycled at varying scan rates in the 1-2V voltage range (Fig. 4.16 c) to evaluate capacitance response (Fig. 4.16 d) under dynamic voltage conditions. SPC followed the order 25 >50>75>100 mV/s from the greatest (33.2 mF cm^{-2}) to the least (6.5 mF cm^{-2}). This is consistent with the fact that at lower scan rates, there are more instances of reversible charge transfer at the electrode-electrolyte interface that leads to a higher SPC. To account for the loss of capacitance at higher cycles, Electro Impedance Spectroscopy (EIS) was done and Nyquist plots are obtained in Fig. 4.16 e for the 80:10:10 sample. The total impedance of the supercapacitor at the beginning (0^{th} cycle) is about 50 ohm while it is about 1.5 kilo-ohms after 1500 cycles as seen by the intersection of the semicircle on the X-axis. A higher impedance to charge transfer at a higher cycle number accounts for diminishing charge storage ability. The slope of the V-t plot in Fig. 4.16 f reveals that at a higher applied discharge current density, the decay of voltage is steeper which is a typical characteristic of a supercapacitor. The negative slope of the SPC vs current density plot in Fig. 4.16 g reveals that at a higher discharge current density, the SPC decreases. This too is a typical supercapacitor behavior. Ragone plot (Fig. 4.16 h) shows very high values of energy and power densities due to the synergistic effect of bimetallic tungstate NP encapsulated in lignin.

4.5.4 Summary

In this research, we studied the roles of the secondary metal (M_2) in pseudocapacitance of bimetallic tungstate type compounds ($M_2M_1WO_4$, M_2=Ni, M_1=Co). It was discovered that the bimetallic tungstate ($NiCoWO_4$) functionalized lignin supercapacitor displayed a high SPC value of 862.26 mF cm^{-2} that was 141 times higher than that of the monometallic tungstate $CoWO_4$ (6.1 mF cm^{-2}) functionalized lignin supercapacitor. The secondary metal M_2 in the bimetallic tungstate ($M_2M_1WO_4$, M_2=Ni, M_1=Co) significantly enhances the pseudocapacitance due to a higher available oxidation state leading to high electronic conduction. The lignin/$NiCoWO_4$ supercapacitor also shows a very high-power density of 854.76 kW kg^{-1} and a maximum energy density of 5.75 Wh kg^{-1} due to a synergistic effect of bimetallic tungstate NP encapsulated in lignin. With a higher proportion of the bimetallic tungstate NP in the composite electrode, the capacitance retention increased. For an optimal mass ratio of lignin:$NiCoWO_4$:PVDF (15:75:10), the retention was 100% even after 2000 cycles. Supercapacitor discharge time study showed a high SPC at higher discharge times while higher retention at lower discharge times. Thus, the rate of consumption of electroactive sites of the pseudocapacitance nanomaterial ($NiCoWO_4$) was linear with discharge time. Carbonization breaks down the lignin molecular structure which creates a high impedance to charge transport and diminished electrochemical performance. The capacitive performance of the bimetallic tungstate supercapacitor was found to heavily depend on the choice of the negative electrode's dielectric permittivity and surface area, and on the type of dominant regime of charge storage i.e., EDLC dominated or pseudocapacitance dominated regime. Thus, this work provides a new knowledge base for the effective use and design of bimetallic tungstate-based nano-bioelectronic devices which will promote green technology.

CHAPTER V

DESIGN AND SYNTHESIS OF HIGH PERFORMANCE FLEXIBLE AND GREEN SUPERCAPACITORS MADE OF MANGANESE-DIOXIDE-DECORATED ALKALI LIGNIN*

State-of-the-art flexible supercapacitors suffer from electrochemical and environmental performance issues including manufacturing expense limitations. Therefore, a highly effective and low-cost strategy to develop supercapacitors is needed. To address this, a plant-based, high-performance, lightweight, low-cost, quasi-solid state, and composite electrode for flexible supercapacitors has been synthesized using the hydrothermal method. The composite electrode is made of alkali lignin and is decorated with MnO_2 particles including an Al substrate. An Al/lig/MnO_2 based anode and an Al/AC (activated carbon) based cathode were sandwiched using an inorganic polymer gel-type electrolyte made of PVA/H_3PO_4 in order to assemble the supercapacitor. Synchrotron tomography and SEM are employed to study the detailed electrode morphology. Electrochemical impedance spectroscopy (EIS), Cyclic charge-discharge (CCD), and cyclic voltammetry (CV) have been used to assess electrochemical performance. Optimization is carried out using a series of lignin:MnO_2 samples with varying constituent ratios. After 3000 charge-discharge cycles, the highest specific capacitance value achieved at 40 mA g^{-1} reached 379 mF cm^{-2}, (900 times reported). The capacitance

---

* Reprinted with permission from “Design and synthesis of high performance flexible and green supercapacitors made of manganese-dioxide-decorated alkali lignin” by Swarn Jha, Siddhi Mehta, Yan Chen, Raj Likhari, Weston Stewart, Dilworth Parkinson, Hong Liang, 2020. Energy Storage, 2, e184, Copyright [2020] by Wiley.

retention, maximum energy density, and maximum power density are 80%, 6 Wh kg^{-1}, and 355 W kg^{-1} respectively. Due to the superior electrochemical performance, the supercapacitor shows exceptional potential for future sustainable and green electronics.

5.1 Background

A sustainable environment is necessary in order to meet increasing energy demands [3, 137]. This is especially important for materials and their structures [7, 11, 12, 59, 138-141] in energy storage devices such as lithium-ion batteries, capacitors, and supercapacitors. In comparison to commercial capacitors, a supercapacitor has higher energy density, power density, and longer discharge time. These advantages make supercapacitors essential for a large number of applications which require sustained high power for a longer duration [16, 24]. To eliminate the potential combustion risk of traditionally used liquid electrolytes, and for the ease of use and portability, a supercapacitor that is an all-solid-state is greatly desirable [50, 142, 143]. In recent years, flexible electronics have attracted great attention, there are many reports about the design, fabrication, and manufacturing of flexible solid-state and portable supercapacitors [4, 21, 47, 48, 50, 62, 92, 142-145]. An asymmetric supercapacitor helps extend the range of the operating voltage past the thermodynamic voltage of the electrolyte decomposition. In addition, the asymmetric design overcomes the charge storage limitation seen frequently within symmetric supercapacitors' designs. However, there are challenges that still remain in terms of electric wastes, bio-un-degradability, high processing cost, non-durability, inherently unsafe design, and un-scalability [146].

The performance and environmental sustainability of a supercapacitor are heavily dependent on the processing methods and materials used. Employing state-of-art biomaterials in electrochemical devices is plagued by outstanding challenges such as unknown surface chemistry, low volumetric energy density, random pore distribution, uncontrolled pore geometry, and structure. These challenges severely affect the fabricated electrode’s performance, cycle life, capacitance retention, and limits potential applications [54]. The crucial elements that affect the device’s usability and performance are the source of the raw materials, extraction methods, and pretreatment processes selected for obtaining the carbon-based biomaterials. The fundamental understanding of carbon reactivity in bioderived materials is yet to be achieved due to its complicated structure and varied chemical composition. Furthermore, modern methods to produce carbon fibers from biomass include electrospinning, ink-jet printing, and spraying however, these techniques use hazardous chemicals and have a high carbon footprint [49]. For example, Schlee et. al used Kraft lignin and employed salt-based oxidation including electrospinning since the widely used PAN fibers use hazardous chemicals and are expensive to obtain [50]. Alkali lignin has a high oxygen percentage which is highly beneficial for advantageous pseudocapacitance properties however, this also limits electrical conductance [51]. Compromise is required when choosing between the expensive Kraft lignin-based process or using alkali lignin with the modified process. Currently, there is an impending need for a simpler and safer activation process which can yield high-performance characteristics.

Also, the surface morphology and microstructure relationship with electrochemistry remain unexplained which restricts the development of new electrode material designs. One significant challenge in biomass is to achieve higher porosity for higher pseudocapacitance. However, this comes at the cost of sacrificing electrical conductivity due to higher porosity leading to reduced electrical conductivity due to pore impedance [17]. Hence, understanding the microstructure and morphologies of electrodes and their impact on electrode porosity and electrical conductance hold the key to better designs. To address this challenge, this research utilized synchrotron X-ray microtomography (μ-CT) with high-resolution in order to observe the surface packing density, surface roughness, particle size, morphology, and interface compactness in sharp detail. ZnO, MnO_2, CoO, RuO_2, NiO, and CuO are some the examples of transition metal oxides highly studied for their use in supercapacitor applications due to their auspicious pseudocapacitance properties [29, 52, 55]. Though RuO_2 is considered the most ideal electrode material, it is scarcely available and therefore, very expensive. On the other hand, MnO_2 is cheaper, available in abundance, and safer in comparison to RuO_2 [56, 57]. However, the low electrical conductivity of MnO_2 ($10^{-5} – 10^{-6}$ S cm^{-1}) limits its use [58]. In recent works, lignin has been used as an active material for supercapacitor electrodes [147-150]. An innovative lignin-Si composite electrode was synthesized as an anode for lithium-ion batteries [151]. Lignin derived carbon materials have also been combined with conducting polymers which have yielded high specific capacitances and energy densities [152]. Active lignin from quinol/ubiquinol enzymes (Q/QH_2) redox moieties has recently garnered a lot of attention [153]. MWCNTs were derived from lignin to make printable MWCNT-based electrodes and RUO_2/MWCNT nanocomposites as active material for electrodes [154, 155]. Most of the studies report the use of lignin as a carbon precursor, or it is pretreated and then combined with conducting polymers, transition metal oxides, etc. to enhance their performance [156, 157]. The processes used to synthesize them, though, are extensive and expensive. The objectives of this research are i) to understand the effect of MnO_2 functionalization on the electrochemical behavior of plant-derived alkali lignin when used in a solid-state asymmetric supercapacitor, ii) to develop an inexpensive and sustainable design strategy for using alkali lignin in a solid-state supercapacitor using green chemistry principles.

To address the challenges in using alkali lignin and the problematic electrical conduction of MnO_2, this research focuses on the development of new materials. This work reports a novel approach of using low-cost alkali lignin as an active carbon-based material, decorated with MnO_2 ions, for lightweight, flexible, asymmetric supercapacitor with high potential for scalability and commercialization. The facile supercapacitor fabrication process uses non-hazardous chemicals; the materials used are from plant feedstock which is bio-degradable, and the performance is optimized for energy storage. Thus, the process used is in line with the green chemistry principles of 'Waste Prevention', 'Use of Renewable Feedstocks', 'Less Hazardous Chemical Synthesis', and 'Design for Energy Efficiency'. The experiment section addresses the fine details of the fabrication and assembly of the supercapacitor. The designed supercapacitor is an excellent substitute for PAN-based fibers. It even shows improved performance than the hazardous PAN fiber-based or the expensive Kraft lignin-based supercapacitors which are also waste generating and high carbon footprint-based methods. Moreover, the design process addresses the problem of achieving high specific capacitance and high electrode conductance at the same time for biomass-derived electrodes. This is done by selecting the elements of the supercapacitor and then optimizing performance for those chosen elements. This research has revealed a new class of electrodes that would be beneficial for the future development of energy storage devices.

5.2 Experimental setup

5.2.1 Fabrication of the Composite Electrode and Electrolyte Gel

Three electrode samples of varying lignin:MnO_2 ratios were prepared. According to the varying ratios, the samples have been designated as, 2X:Y, X:0.5Y, and X:Y. The concentration of the $KMnO_4$ solution is, Y = 47.5 µmol, and X = 0.3 g of lignin. The method used to prepare the three samples is the same throughout all the samples. For instance, to make the X:Y sample, 0.0003 g of crystalline powdered $KMnO_4$ (Aldrich, size <150 µm, MW=158.03 $gmol^{-1}$) was added to distilled water (50 ml) in order to prepare a 47.5 µmol (Y) $KMnO_4$ solution. Alkaline lignin (from TCI) of quantity X was added to the $KMnO_4$ solution of concentration Y in a Teflon liner. This liner was then placed in a hydrothermal autoclave reactor. For the formation and deposition of the MnO_2 nanoparticles, the solution was treated hydrothermally for 60 minutes at 160^0 C [158]. The solution obtained was drained of the excess liquid. The slurry obtained was then dried at 50^0C overnight. PVDF (MW = 180,000 by GPC, Sigma Aldrich) was added to the slurry obtained earlier (Lig-MnO_2) in 4:1 ratio with the solvent, NMP (2 ml) (>

99% pure, MW = 99.13 gmol^{-1}, density = 1.028 g ml^{-1}, Sigma Aldrich). The resulting slurry mixture was then coated on a substrate made of aluminum foil (thickness = 0.98 mm). The circular (diameter = 4 cm) cut substrate had adjoining strips (1 cm x 3 cm) that were flexible over 360^0. Heat treatment was done on the coated substrate in a vacuum atmosphere at 100^{0}C after which the composite lignin/MnO_2 electrode was obtained. The PVA/H_3PO_4 electrolyte gel was obtained in a similar manner in our recently published work [62].

5.2.2 Assembly of the Quasi-Solid State and Asymmetric Supercapacitor

The supercapacitor was constructed using Al/AC for the cathode and Al/lignin/MnO_2 as the anode. The electrolyte coated separator was sandwiched in between the two electrodes. The representation of the assembly process of the supercapacitor is represented in Figure 5.1.

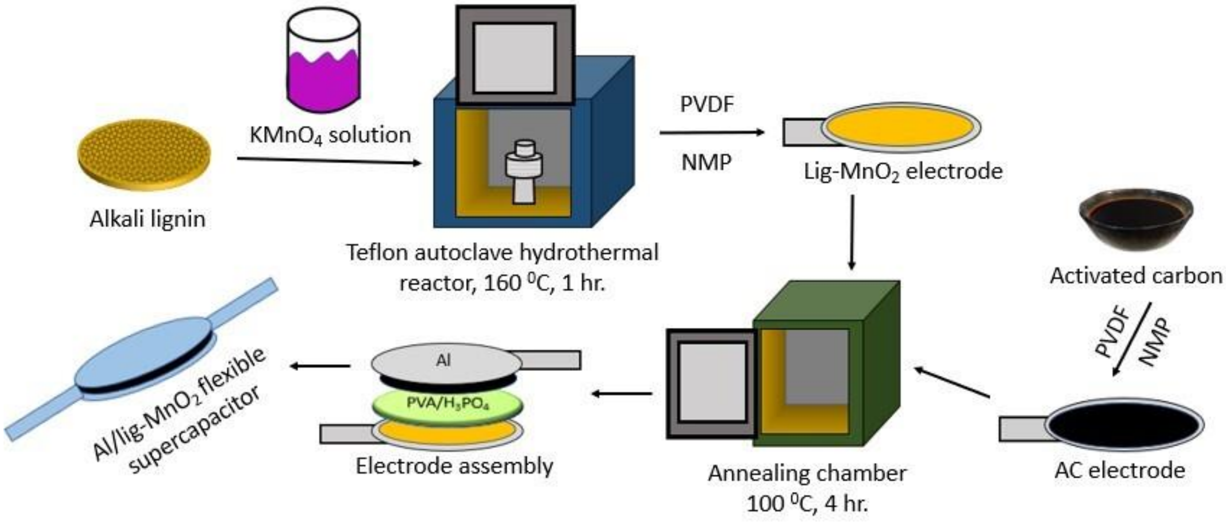

Figure 5.1 Fabrication process of the lignin/MnO_2 supercapacitor.

5.2.3 Materials Characterization

The supercapacitor surface characteristics were observed using a scanning electron microscope (SEM) characterization (VEGA/TESCAN model at 5 kV, 100x). Synchrotron tomography (X-rays at 35 keV) of the supercapacitor electrodes was done in order to observe the 3D morphology of complex molecules within lignin in detail and AC in a non-destructive manner. The details of experimental set up are similar to our recently published work.[21]

5.2.4 Electrochemical testing

The capacitive performance of our supercapacitor was tested using cyclic charge-discharge (CCD), electrochemical impedance spectroscopy (EIS), and cyclic voltammetry (CV) by using a Gamry (version 6.33) potentiostat. The lignin/MnO_2 based electrode was used as the anode. The reference electrode and the AC based electrode connections were linked at the positive terminal of the potentiostat. The CV was carried out at several scan rates and voltage ranges (Figure 5.6). In the CCD experiment, a 40 mA g^{-1} current density was applied, and 60 seconds was used for each charge and discharge cycle. The total cycles run were 3000 and 20 V was the upper voltage limit. An EIS test was performed (10^6 Hz - 0.1 Hz frequency, with DC of 1 V, and 10 mV AC) so that the parameters of the experiment were consistent with the potentiostat guidelines on the diffusion and mass transfer limited processes.

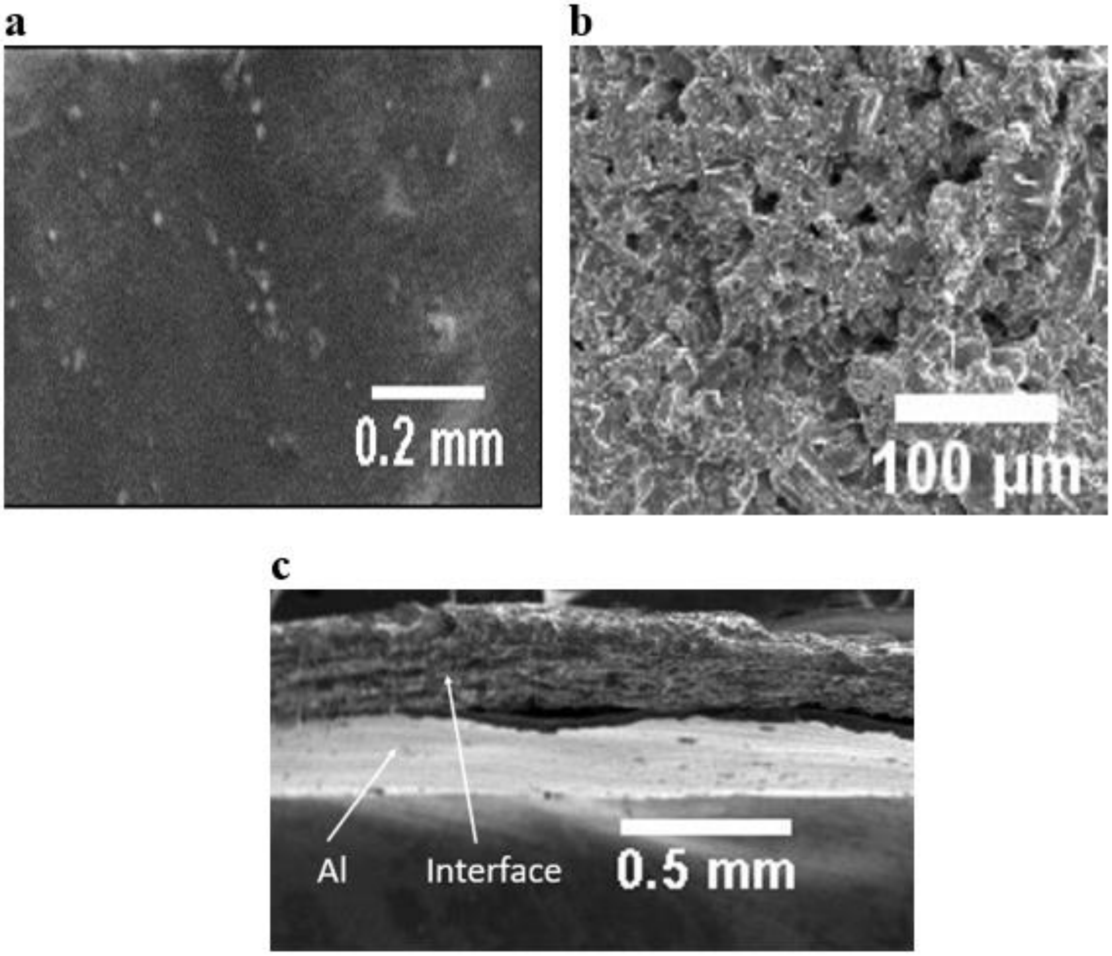

Figure 5.2 SEM images of (a) gel electrolyte (PVA/H_3PO_4), (b) negative electrode (AC), and (c) the supercapacitor interface displaying the gel electrolyte layer over the lignin-MnO_2 electrode with the Al substrate underneath.

5.3 Results and discussions

5.3.1 Scanning Electron Microscope (SEM)

SEM was utilized to observe the electrode's surface along with the interface of the supercapacitor (Figure 5.2). As seen from Figure 5.2a, the PVA/H_3PO_4 gel electrolyte surface is smooth and undamaged. This helps ensure good interfacial contact with the electrodes. The AC particles of the cathode (Figure 5.2b) seem to be evenly distributed with the presence of pores. Porosity is essential for a higher area of contact for electrochemical reactions. In Figure 5.2c, the interface of the assembled supercapacitor has a thickness close to 200 microns. The gel-electrolyte layer is seen to have adhered strongly to the underneath Al substrate. This suggests strong mechanical stability and interface integrity which are critical for strong electrochemical performance.

5.3.2 Synchrotron Micro-Tomography (μ-CT)

Synchrotron micro-tomography technique was employed in order to observe and compare the detailed particle morphologies of the activated carbon and composite lignin-MnO_2-based supercapacitor electrodes (see Supplementary Information Figure 5.3S). Since the lignin and AC particle have carbon chains which are complex and randomly oriented in 3D space, synchrotron tomography presents a highly suitable non-destructive technique for observing the particle nature. Two separate supercapacitor electrodes, one made of AC (Figure 5.3a) and the other made of lignin-MnO_2 (Figure 5.3b), were subjected to high-resolution tomographic scans. A rectangular section of size 100 × 50

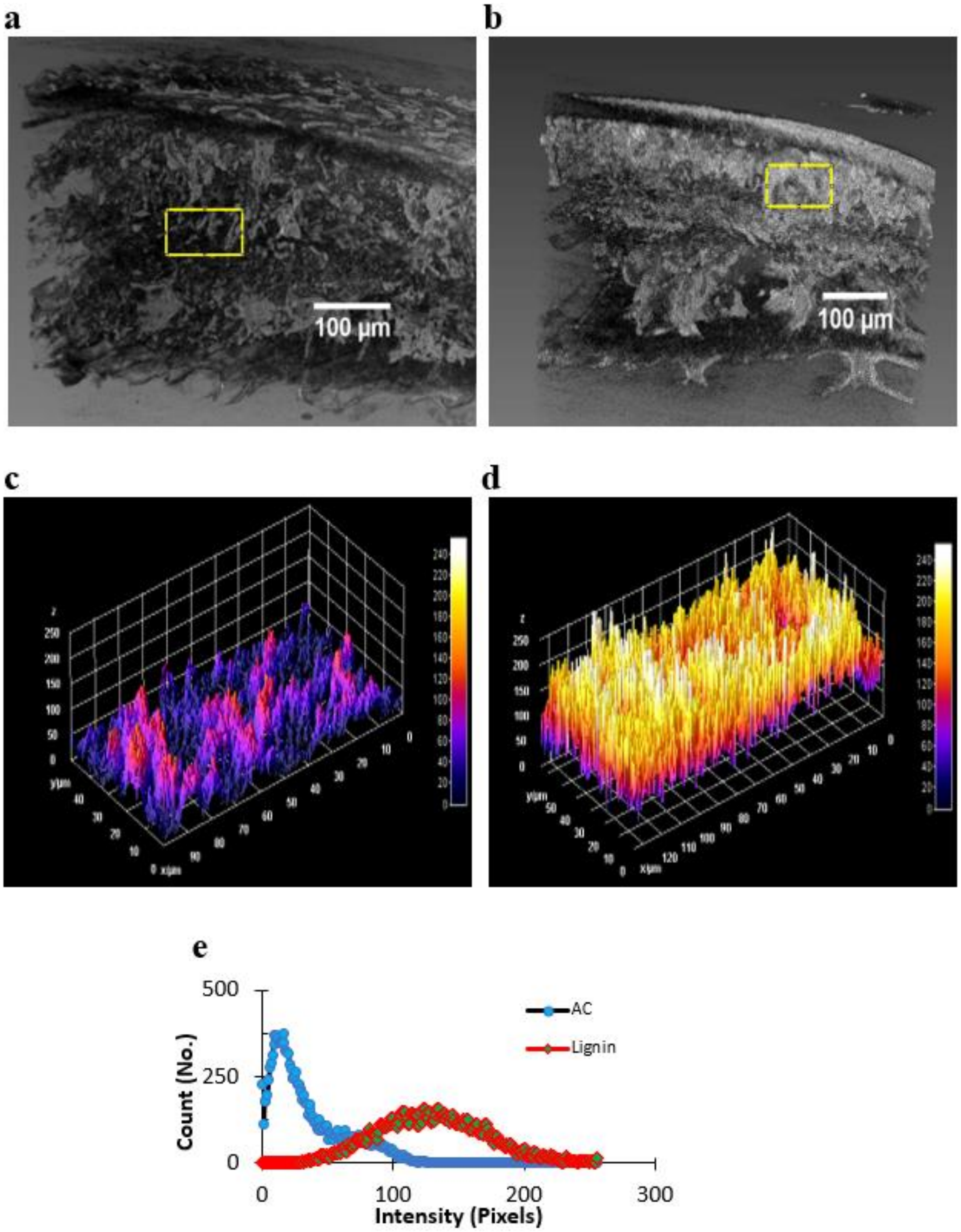

Figure 5.3 Synchrotron micro-tomographic images of the lignin/MnO_2 based supercapacitor sample materials: (a) The AC supercapacitor electrode as reference, and (b) the lignin/MnO_2-based supercapacitor electrode. The yellow rectangular section (100 × 50 µm) is depicted in (a) and (b). The horizontal line denotes the X-axis direction

(width) and the vertical line denotes the Y-axis (height). Interactive surface plot (3D) of (c) the AC electrode surface; and (d) the lignin/MnO_2 electrode surface of the supercapacitor (color bar on the right indicates the pixel value). The histogram plot (e) comparing particle count (Y-axis) at varying intensities (pixels) for in the images (a) and (b).

µm (marked yellow in Figure 5.3a and Figure 5.3b) was used to measure the particle morphological features using image (Table 7).

Table 7. Measured particle morphology parameters from the image obtained via tomography for the lignin and the AC-based supercapacitor electrodes.

Morphology parameter	Activated carbon electrode	Lignin electrode
Circ.	0.69	6.68
IntDen	170675	114780
Mean	33.96	130
Round	0.5	0.48
StdDev	27.29	40.26
Min	0	12
Max	139	255
Skew	1.03	0.15
Kurt	-0.21	0.19
AR	2	2.07

A higher circularity value of AC (Circ. = 0.69) than lignin (Circ. = 0.68) shows that the AC particles are more circular than lignin particles. This indicates a more branched carbon chain structure of lignin. It is ascertained again by the ‘Round’ parameter value, which is higher for AC (0.5) than lignin (0.48). The dividend of the major axis length to the minor axis length of an elliptical-shaped particle is represented by the ‘AR’ or aspect ratio. Lignin particles have a higher aspect ratio (AR = 2.07) suggesting at a smaller minor axis compared to that of AC (AR = 2). The ‘IntDen’ parameter measures the total number of pixels within a region which is directly proportional to the surface packing density of molecules. ‘IntDen’ value for lignin (170,675) is higher than AC (114,780) hereby 48.7 %. This suggests that the lignin electrode surface has a greater surface mass packing density. This surface mass packing density directly affects a supercapacitor’s energy density and a greater surface mass packing density is highly desirable for improved energy density. In the surface analysis, skewness (‘skew’) compares a surface profile to a Gaussian surface (bell-shaped distribution) while kurtosis (‘Kurt’) presents a measure of the sharpness of the peaks of the surface profile. A larger ‘skew’ value for AC (1.03) compared to lignin (0.15) exists which suggests that the lignin electrode surface is comparatively closer to a Gaussian surface. This is also evidenced by a long tail in the AC plot and a symmetric plot in the lignin curve in Figure 5.3e. A negative ‘Kurt’ value (-0.21) for the AC electrode surface suggests that the surface is flatter when compared to the lignin electrode surface (Kurt = 0.19). Thus, the lignin-electrode surface compared to the AC electrode is rougher. A low surface roughness aids in good interfacial contact and in enhanced transport of charge across the interface. The intensity response to the X-rays directly corresponds to the particle nature of the sample. It particularly points to the chemical identity and functional groups present. A particle having a higher K-edge shows a higher average intensity to the X-rays in tomography. As seen from Figure 5.3e, the lignin curve is right-shifted (mean =130) to the AC curve (mean = 33.96) in the intensity-count plot. This suggests that the incoming X-rays face a comparatively larger resistance from the complex chemical and functional groups in the lignin molecules. The 3D interactive surface plot across the 100 × 50 μm section of AC (Figure 5.3c) and lignin (Figure 5.3d) electrodes gives a qualitative visual understanding of the particle distribution across the electrode surface. Intensity distribution across a surface of an electrode is directly related to the chemical nature (functional groups and monomers) of the active material. Besides, the mass distribution on the surface is easily visualized using a 3D plot. The AC electrode (Figure 5.3c) peaks are all lying below the 100 pixels line while for the lignin electrode (Figure 5.3d), most peaks fall below the 200 pixels line and a few cross the 240 pixels mark. A higher average intensity in the lignin electrode surface is due to its highly complex chemical identity. In both the AC and lignin electrode surfaces, the intensity distribution is continuous which indicates there is continuity in surface mass distribution which is essential for achieving enhanced surface and volumetric energy density. Thus, it is seen that for the Al/lig/MnO_2//AC/Al asymmetric supercapacitor, there is a greater density of surface mass packing on the lignin electrode and a lower value of roughness on the AC electrode surface. This synergistic combination of materials and electrode design helps in reducing surface void fraction and in achieving improved interfacial charge transport.

5.3.3 FTIR Analysis

In our recently published work, FTIR spectroscopy was done for lignin and AC based electrodes to identify the chemical bonds present in both the materials and understand their chemical structure [62]. The peaks were referenced with the literature report for both materials [84, 159, 160]. Detailed discussion will not be provided here.

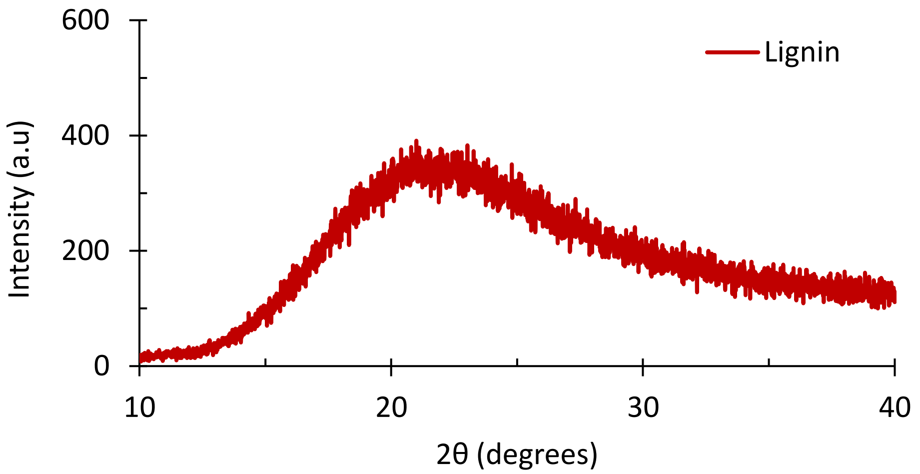

Figure 5.4 X-ray Diffraction of lignin particles used in the lignin/MnO_2 electrode

5.3.4 X-ray Diffraction

To elucidate the crystallinity of lignin, X-Ray Diffraction (XRD) was done. In the XRD plot (Figure 5.4S), a broad peak of diffraction can be seen at $2\theta = \sim 22^\circ$. This broad peak indicates the amorphous nature of lignin [161].

5.3.5 UV-vis Spectra

Figure 5.5 shows the UV-vis spectra of MnO_2. A typical broad absorption peak is visible between the range 310-360 nm confirming the presence of MnO_2 after a successful hydrothermal deposition. The d-d transition occurring in the Mn^{4+} ions is indicated by a peak at approximately 360 nm. The formation of this peak is due to the thermal decomposition of $KMnO_4$ [80].

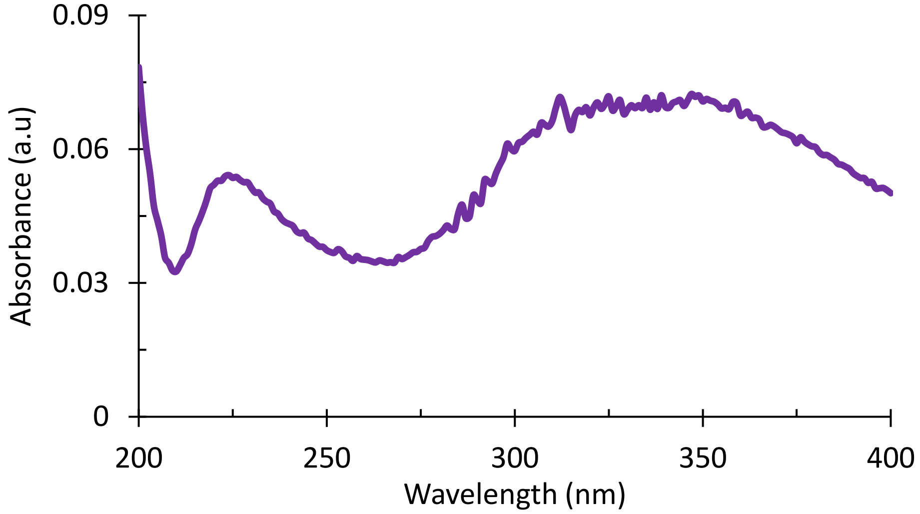

Figure 5.5 UV-vis Spectra of MnO_2 used in the lignin/MnO_2 electrode

5.3.6 Electrochemical Analysis

A three-electrode test was performed using Ag(s)/AgCl (reference electrode) and a graphite rod as the anode. The lignin-MnO_2 electrode or the AC electrode was used as the cathode (working electrode). The electrolyte used was H_3PO_4 (85 wt. %). In Figure 5.6a, the CV curves are shown for the optimal potential window of -1 to 0 V, for the AC-based electrode. Similarly, the optimal potential window for the lignin-MnO_2 was 0 to -1 V (Figure 5.6b). The CV test was run for 25, 50, 70, 100, and 200 mV/s for both, lignin-MnO_2 and AC. Good cyclic performance was exhibited by the working electrodes. Figure 5.6c and figure 5.6d, show the discharge voltage versus time plots at varying current densities, for AC and lignin-MnO_2, respectively. The slope of voltage discharge is observed to be steeper for AC than for lignin-MnO_2. The plot of specific capacitances at varying current densities can be seen in figure 6e. It is observed that with the rise in current density, the specific capacitance decreases for both the working electrodes. As the specific capacitance values for lignin-MnO_2 were higher than AC at all current densities, the lignin-MnO_2 electrode was employed as the cathode and AC as anode for further electrochemical testing and analysis.

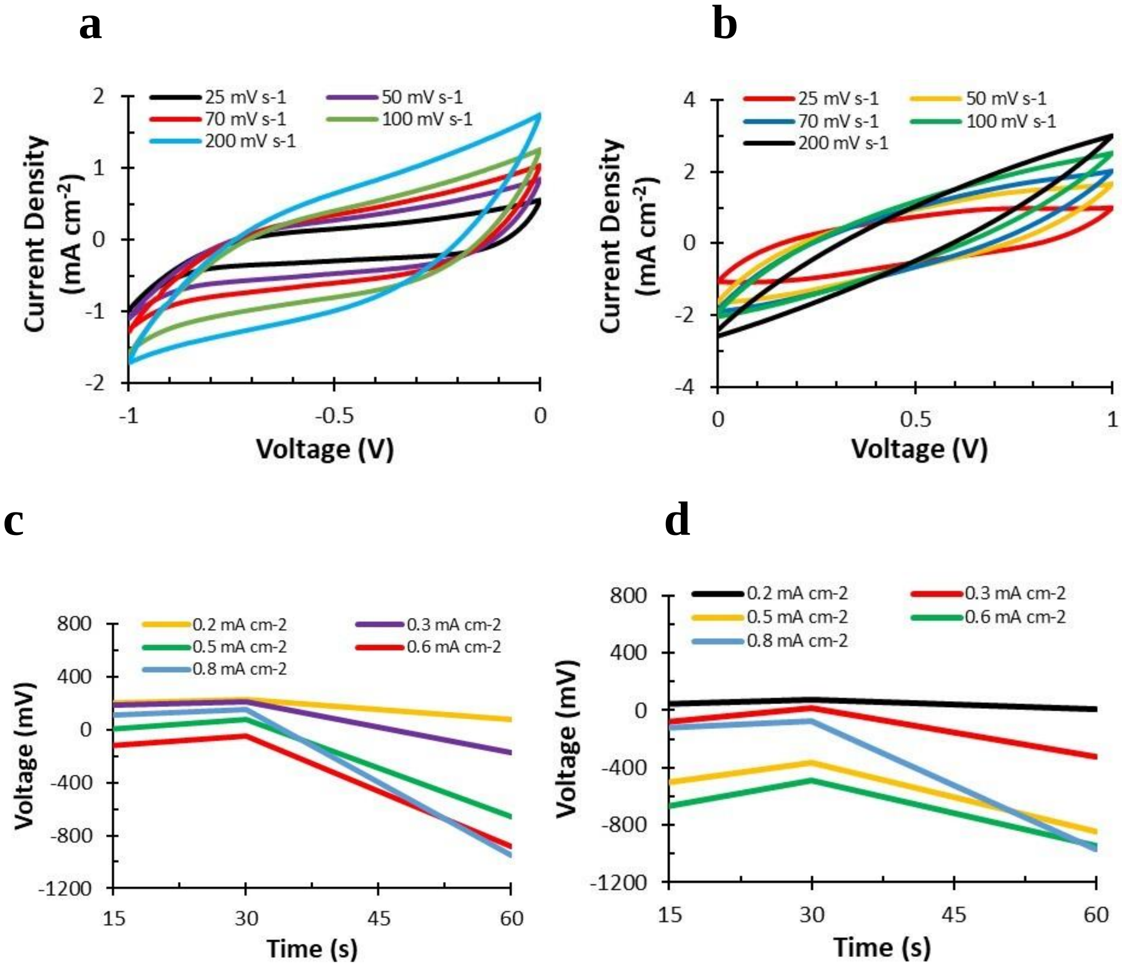

e

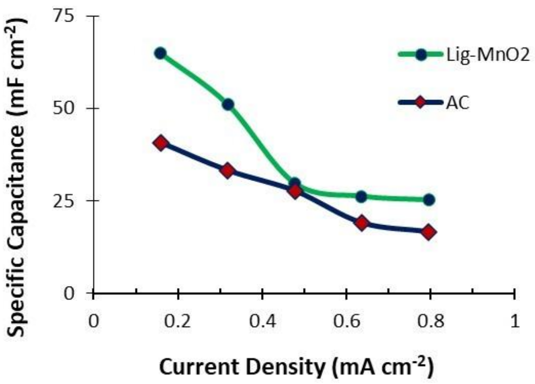

Figure 5.6 Three-electrode tests for the AC and lig-MnO2 electrodes: CV plots for the AC (a) and lig-MnO_2 (b) electrodes at varying scan rates. Voltage versus time plots for the AC (c) and lig-MnO_2 (d) electrodes at varying current densities, and (e) the specific capacitance versus current density plots for the AC and AC/lig-MnO_2 electrodes.

For testing the capacitive performance, cyclic charge-discharge (CCD) and cyclic voltammetry (CV) experiments were run. For cyclic voltammetry, the assembled supercapacitor was first tested at decreasing scan rates of 50, 25, 10, and 5 mVs^{-1} (Figure 5.7a).

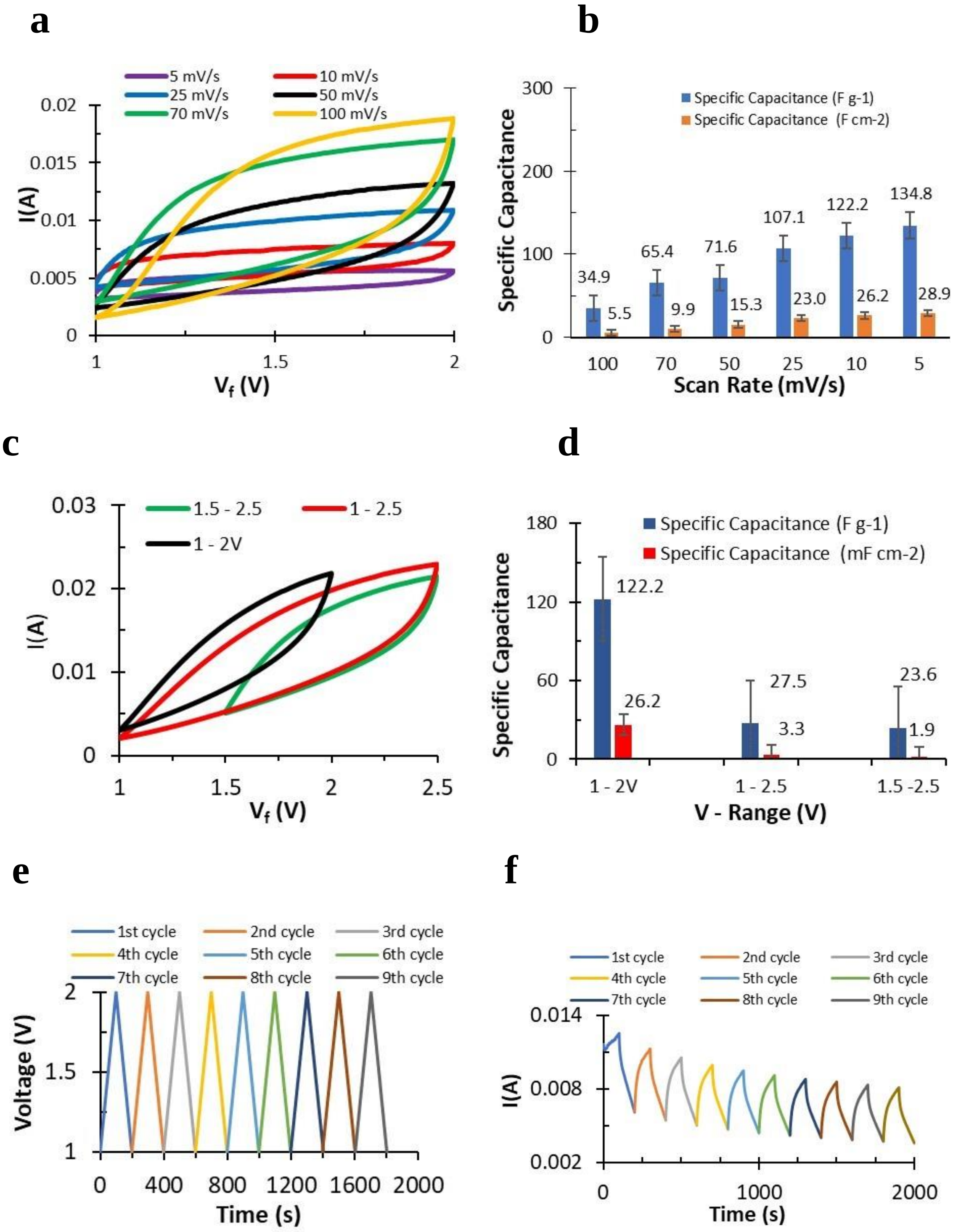

Figure 5.7 (a) CV curve at different scan rates of lig/MnO_2 supercapacitor; (b) comparison of specific capacitance vs varying scan rates, (c) CV plots of varying voltage

windows, and (d) comparison of specific capacitances with varying voltage windows at a constant scan rate of 10 mVs^{-1}. From the CV experiment the (e) the voltage-time curve, and (f) the current-time curve.

For rates of scan voltage above 10 mVs^{-1}, the voltage scan appeared fast, resulting in a low specific capacitance. At rates of the scan voltage below 10 mVs^{-1}, the system was unstable, despite a higher specific capacitance. Thus, the cyclic voltammetry was done at the optimal rate of scan voltage 10 mVs^{-1}. Due to unprocessed lignin in the composite lig-MnO_2 electrode, there is a possibility of many chemical impurities present. These varied chemical entities lead to many side surface electrode reactions which may be coupled with charge transfer kinetics. This leads to the occurrence of multiple side reaction peaks and consequently a high degree of noise (instability) in the system. It has been observed that, in case of slow irreversible chemical reactions, the thickness of the diffusion layer is dependent on the applied potential (proportional to scan rate) and it is smaller at a higher applied potential [162, 163]. Thus, at higher scan rates, the slow irreversible reactions are predominantly favored leading to high current. This leads to the absence of side reaction peaks and consequent noise from the system leading to a smoother CV curve. This phenomenon is, however, a complex one and dependent on multiple factors like the choice of electrode material, chemical species present, competing chemical reactions, diffusion coefficients, kinetics, and thermodynamics of reactions in question. Therefore, there is no general rule that can, as such, be provided here for the instability and noise in the system. This fact is also corroborated in Figure

5.7b. The average specific capacitance of the supercapacitor is 122.21 Fg^{-1} (26.19 mF cm^{-2}) at 10 mVs^{-1} and 71.58 Fg^{-1} (15.34 mF cm^{-2}) at 50 mVs^{-1}. Since it is important to determine an optimal operating voltage range, CV plots were also obtained at different voltage ranges (Figure 5.7c). In Figure 5.7d, the specific capacitances for the different voltage ranges can be seen (optimal scan rate of 10 mVs^{-1}). For the voltage window of 1-2V, the highest specific capacitance (122.21 F g^{-1}) was obtained. The lowest average value of specific capacitance (23.59 Fg^{-1}) was obtained for a voltage range of 1.5 – 2.5 V. Therefore, the supercapacitor displayed optimal performance in the potential window of 1V - 2V and 10 mVs^{-1} scan rate. Based on similar earlier works that used MnO_2 based active material, it is reasoned that MnO_2 displays the pseudocapacitance property via reactions that occur in the positive potential window in which Mn^{+4} is reduced to Mn^{+2} oxidation state [164, 165]. As such, in the negative potential window, the supercapacitor's CV plot does not show considerable capacity retention. In those ranges, the CV curves appear almost as straight lines which is indicative of no charge storage within the supercapacitor. This is because of the choice of material (lig-MnO_2) and the pseudocapacitance potential window. The current-time and voltage-time plots (Figure 5.7e and Figure 5.7f) were obtained for further analysis. The variation in the voltage, for each cycle (Figure 5.7e), is constant. Each charge cycle starts at 1V and ends at 2V. For the discharge cycle, the polarity of the electrode is reversed. A negative slope showing the voltage decay can be seen until 1V. For the voltage variation at each cycle, a current developed correspondingly. This current is reliant on the material of the electrode, the electrolyte, the design, and the assembly of the supercapacitor. In Figure 5.7f, the current vs time plot obtained is almost similar to the voltage-time plot. However, the current variation is non-linear, unlike the voltage variation. The slope of the discharge current is observed to be steeper than that of the charge current. This shows that supercapacitor has a tendency to get discharged faster compared to getting charged. It can also be seen that the current, highest in the first cycle, falls gradually in succeeding cycles. This can be attributed to the electrochemical reactions causing the eventual decay of the electroactive material.

To assess the capacitance performance of the electroactive material, 500 cycles of CCD were run for each at 40 mA g^{-1} current density for the three-electrode samples with varied lig:MnO_2 ratios. The variation of specific capacitance (areal) for 500 cycles, is obtained (Figure 5.8a). The specific capacitance (areal) retention can be seen in Figure 5.8b. From

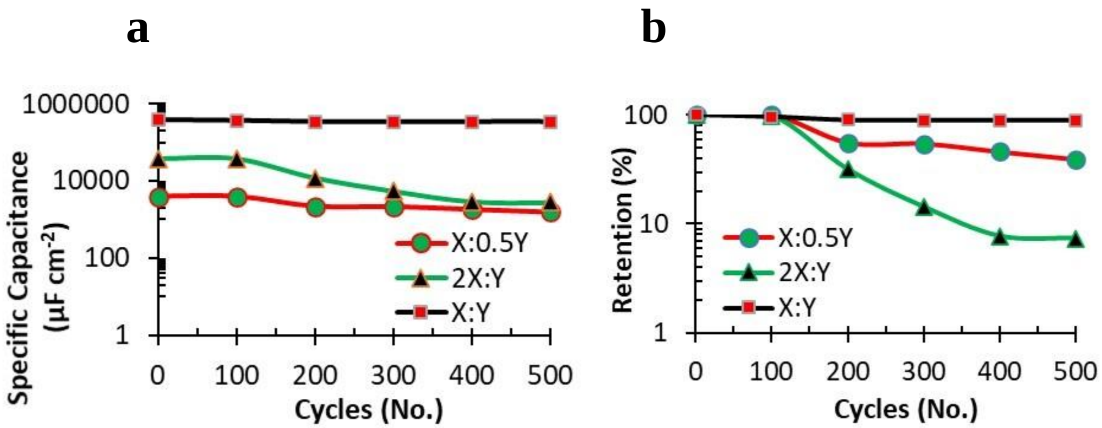

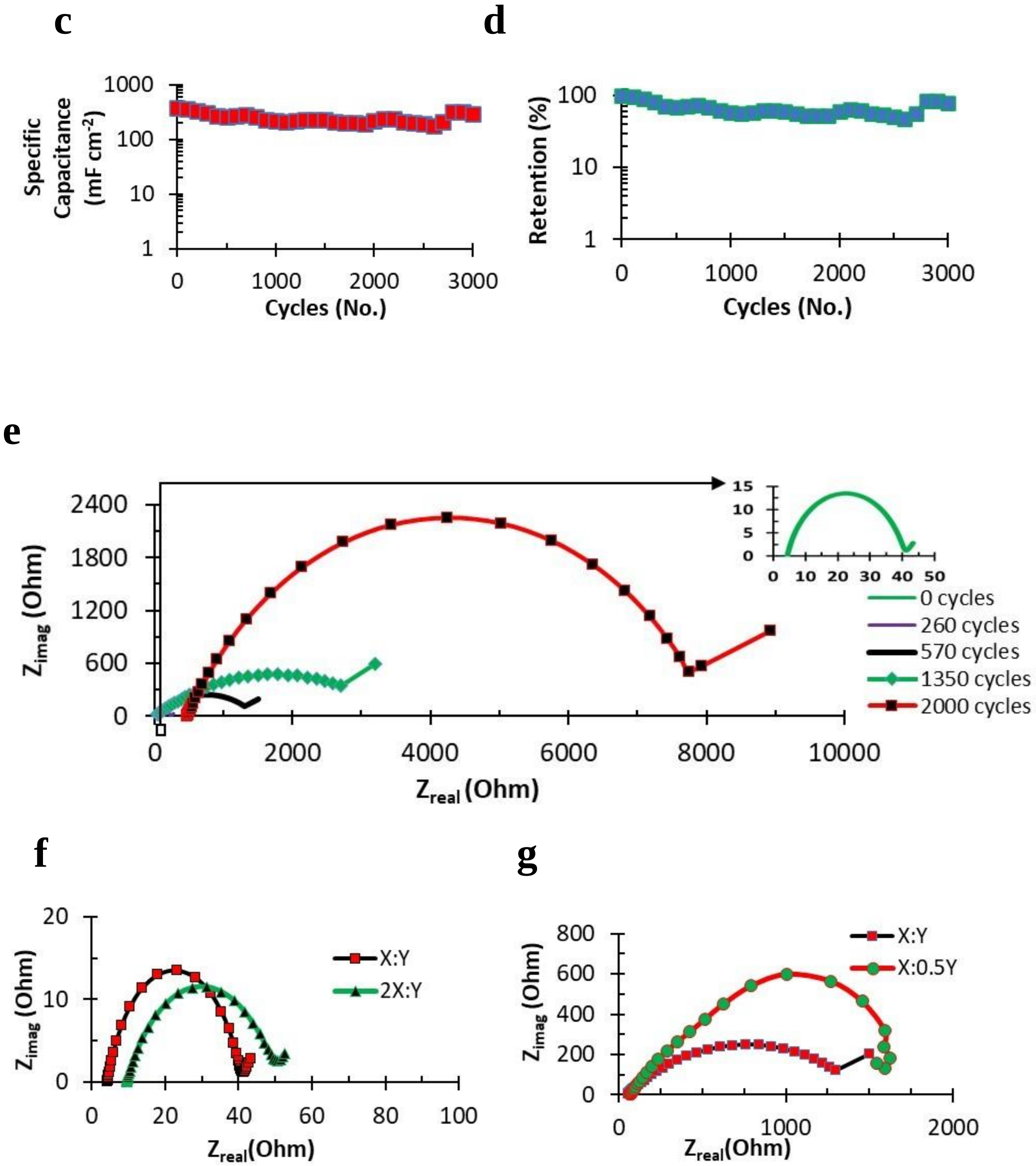

Figure 5.8 For the CCD experiment at 40 mAg^{-1}current density: plot of the changes of areal specific capacitance (a) and retention (b) with cycles for 500 cycles for samples X:Y, X:0.5Y and 2X:Y; plot of the change of areal specific capacitance (c) and capacitance retention (d) for the sample X:Y run for 3000 cycles; (e) Nyquist plots of

EIS test run for X:Y sample; (f) Nyquist plots of the samples 2X:Y and X:Y for the 1st cycle; (g) Nyquist plots of samples 2X:Y and X:Y after 500 cycles.

Figure 5.8a and Figure 5.8b, it is observed that the specific capacitance (about 379 mF cm^{-2}), and areal specific capacitance retention, for the 500 cycles is highest for sample X:Y. However, final retention is in the order X:Y > X:0.5Y > 2X:Y as observed from Figure 5.8b After the comparison of X:Y and 2X:Y samples, it was observed that both the retention and the specific capacitance decreases when the lignin weight % is increased or a lower concentration of $KMnO_4$ is used. Thus, the sample X:Y had the optimal lig:MnO_2 ratio which showed high specific capacitance and high retention. Herou et. al reasoned that due to the heterogeneous nature of the biomass morphology, there is greater variability in the diffusion of ionic species which is used to functionalize the biomass molecules [48]. As such, we find that X:Y sample, in this case, performs the best compared to other samples. The sample (X:Y) was further run up to 3000 cycles (Figure 5.8c). The specific capacitance (areal) initially was 379 mF cm^{-2} (Figure 5.8c), while after 3000 cycles it was 304 mF cm^{-2} (80 % retention, Figure 5.8d). Schlee et. al used Kraft lignin fibers and obtained specific capacitance in the range 147 – 350 mF cm^{-2} [50]. Thus, the obtained result with alkali lignin in this report is optimal. Furthermore, the fabricated supercapacitor shows characteristics of being highly efficient, economy-friendly, and more environmentally friendly in comparison to many other literature reports (Table 8). The maximum values of power and energy density obtained were 355 Wkg^{-1} and 6 Wh kg^{-1}, respectively. Youe et. al used Polyacrylonitrile fibers (PAN) to produce nanofiber mats in symmetric pseudocapacitor applications. However, PAN production uses many hazardous chemicals. Also, the power density achieved was only 160 W kg^{-1} which is lower than this report (355 W kg^{-1}) [166]. Considering the cost and carbon footprint involved in fiber production, the fabricated asymmetric supercapacitor reported in this research is much simpler and cost-effective which is much more appealing for scalability and commercialization. An EIS experiment was run to understand the impedance characteristic of sample X:Y and Nyquist plots were obtained which can be seen in Figure 5.8e. At the 0th cycle, the impedance is 40 ohm and after the 2000th cycle is 7930 ohm. The trend of the impedance values goes from the lowest value to the highest value, as expected. This behavior indicates that, with increasing cycle numbers, the impedance also increases. This leads to a lesser flow of current resulting in lower retention. However, the initial impedance rate is relatively slow (beginning to-570th cycle). The impedance after that increases faster between the 570th cycle and the 2000th cycle. For comparison, the initial (0th cycle) EIS curves (Nyquist) of the samples 2X:Y (green) and X:Y (red) are shown in Figure 5.8f. The initial impedance for sample 2X:Y is 49 ohms which is higher than that for sample X:Y (40 ohms). This accounts for higher current flow and charge storage (specific capacitance) initially in sample X:Y when compared to the sample 2X:Y. Similarly, after 500 cycles (Figure 5.8g), the total impedance of sample X:0.5Y (1590 ohm) is greater than that of sample X:Y (1300 ohm) indicating higher charge storage (specific capacitance) in sample X:Y.

A detailed comparison of the lig/MnO_2 supercapacitor’s capacitive performance with other literature reports is presented in Table 8. The fourth column presents the ratio of current work's specific capacitance (SCP) to that of the work in the literature (SCL). The ratio ranges from 2 – 900 which is remarkable and significant.

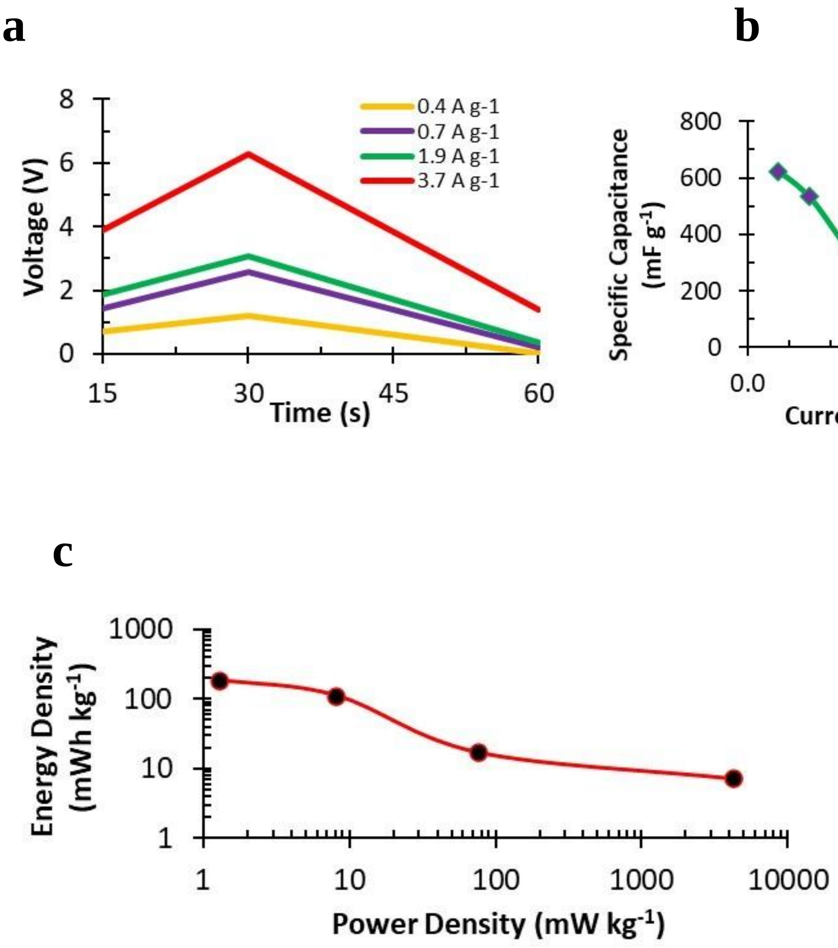

Figure 5.9 For the lig/MnO_2 supercapacitor, (a) Variation of voltage with time comparison at changing current densities, (b) variance of specific capacitances with discharge current density at 1 mA charge current, and (c) the Ragone plot.

The influence of different current densities on the discharge voltage is shown in Figure 5.9a. The resulting voltage curves are plotted for changing current densities. It is observed that as the current density rises, the voltage vs time curve's slope gets steeper.

Hence, the voltage drop rate is the highest at the highest value of current density (3.7 Ag^{-1}). Figure 5.9b shows the current density (discharge) effect on the areal specific capacitance (for charge current =1 mA). The specific capacitance drops hyperbolically as the discharge current density increases which is the expected behavior of a supercapacitor. A Ragone plot is shown in Figure 5.9c. The relative change in energy density corresponding to power density, for different current densities, can be observed in this plot. The Ragone plot obtained for the MnO_2 based supercapacitor in this work is similar to those reported. Here, we observe an upward convex part of the curve which is followed by an upwards concave decline of energy density corresponding to an increasing value of power density.

Table 8. Comparison of capacitive performances of the current work with reports in the literature.

Material of substrate	Electrode materials	Maximum Specific Capacitance (SPC)	SCP/ SCL[†]	Energy Density (Wh kg^{-1})	Power Density (Wkg^{-1})	Ref.
Al	Lignin/MnO_2	379 mF cm^{-2}), 3000 cycles, at 40 mAg^{-1}	1	6	355	This work
Au	MnO_2	12 mF cm^{-2}, 2000 cycles, at 0.3 mA cm^{-2}	31.58	-	-	[166]
PET	Graphene/MWNT	0.74 mF cm^{-2}, 20,000 cycles at 1 μA cm^{-2}	505.33	-	-	[167]

[†] (SCP/SCL) is the ratio of specific capacitance of current work (SCP) and specific capacitance of the cited work (SCL))

mCel-membrane	Activated carbon	153 mF cm^{-2}, 1000 cycles at 10 mVs^{-1}	2.5	4.37	249	[168]
PET	$SnSe_2$	0.406 mF cm^{-2}, 1000 cycles at 20 mA m^{-2}	933.5	-	-	[68]
Carbon fabric	MnO_2//MoO_3	3.2 mF cm^{-2}, 3000 cycles at 5 mA cm^{-2}	118.44	-	-	[74]
Carbon fabric	MnO_2	42.4 mF cm^{-2}, 2000 cycles at 5 mVs^{-1}	8.94	-	25	[169]
FTCF	rGO/PANI	6.4 mF cm^{-2}, 2000 cycles at 0.08 mA cm^{-2}	59.22	7.07	707	[77]
Xerox printing paper	MnO_2/Au/MnO_2	8.14 mF cm^{-2}, 5000 cycles at 0.2 mA cm^{-2}	46.56	-	-	[170]
PET	N-doped rGO	3.4 mF cm^{-2} at 20 µA cm^{-2}, 2000 cycles	111.48	-	-	[75]
A4 commercial paper	Graphene sheets	11.3 mFcm^{-2} for scan rate 1 mVs^{-1}	33.53	-	-	[171]
Ti	CNT	1.84 mF cm^{-2}, 1000 cycles at 1 mA,	206	-	-	[73]
PET	β-$Ni(OH)_2$/graphene	2.57 mF cm^{-2}, 2000 cycles at 0.2 Am^{-1}	147.5	-	-	[76]
PET	SnS/S doped graphene	2.98 mF cm^{-2}, 10000 cycles at 60 mA cm^{-2}	127.18	-	-	[172]

5.4 Summary

A new class of biomass-derived supercapacitor was successfully fabricated using a facile and low-cost synthesis. The supercapacitor is lightweight, portable, and flexible. In contrast to AC (cathode), the lignin/MnO_2 (anode) shows a higher surface packing density. This is confirmed by the 'IntDen' parameter value which is larger for lignin compared to AC. A higher surface packing density resulted in achieving a high value of energy density. The smoother AC electrode surface ensures a stable interface that aids in enhanced charge transport. The AC particles have a high porosity which contributes to the higher contact area between the active material and electrolyte for improved electrochemical reaction. Nanostructured MnO_2 was deposited on alkali lignin (lig) to boost the electrochemical reaction. At 40 mAg^{-1} current density, the peak value of areal specific capacitance achieved is 379 $mF\ cm^{-2}$ (up to 900 times greater than the reported). The highest power and energy densities achieved were 355 $W\ kg^{-1}$ and 6 $Wh\ kg^{-1}$, respectively. These values are in the high-value range among the ones reported. The retention of capacitance obtained for the supercapacitor is 80 %. The capacitive performance exhibited by the supercapacitor makes it suitable for several real-world applications. Various compositions of lig:MnO_2 have been tested in order to obtain optimal quantities of the constituents for the best capacitive performance. Research results revealed three aspects: 1) Alkali lignin can be used as an active material to obtain high-performance electrodes for supercapacitors. 2) An optimal lignin:MnO_2 ratio results in a high specific capacitance and high retention. 3) An inexpensive, sustainable, and green chemistry-based design and fabrication strategy for alkali lignin supercapacitors developed in this work shows a significant advance over the traditionally used hazardous and highly expensive processes. Given the challenge of obtaining satisfactory electrochemical performance using a low-cost method focused on sustainability, this work is exemplary in exploring the future potential of alkali lignin in flexible supercapacitors. On account of the cost-effective method used, the non-hazardous process, superior performance, and the choice of raw materials extracted from biomass, this work will earmark a crucial step in developing electronics from green and sustainable sources.

CHAPTER VI

STRUCTURAL INVESTIGATION OF NANO SPHERICAL LIGNIN

Lignin nanoparticles (LNP) of the spherical morphology are investigated for their electrochemical properties in supercapacitor. Nanoparticles from renewable resources are biodegradable in nature. Among the different available methods for LNP, acid precipitation is simple and cost-effective and utilized here. Material characterization involved XRD, FTIR and SEM. Asymmetric supercapacitors were assembled for the three types of lignin alkali lignin (AL), Dealkaline lignin (DAL), and Lignosulfonate (LS). Electrochemical performance of the supercapacitors were studied against varying catalyst, drop rate of catalyst, and UV exposure time.

6.1 Background

The last few decades witnessed tremendous growth and development in the field of engineered nanomaterials and their broad-spectrum applications in science and technology. Nanomaterials encompass the fields of engineering, biotechnology, biomedicine, and natural sciences and have the potential to address challenges in these fields. There are various methods available for the production of nanomaterials. Nanomaterial synthesis usually have a toxic effect on the environment and living things and also, they are expensive. Thus, there is a need for a cost-effective, simple and green route for the synthesis of nanomaterials in accordance with green chemistry principles, such as the biosynthesis of nanomaterials using microbes or plant extracts and directly or indirectly obtaining nanoparticles from biobased materials. Nanoparticles from renewable resources are biodegradable in nature and have the potential to be used in the different eco-friendly applications. There are a number of biomaterials used to synthesize their nanoparticles for example, cellulose, chitosan, and lignin.

Recently, interests have grown in the synthesis of lignin nanoparticles (LNP), which have been fabricated by different methods such as CO2 saturation, solvent exchange (of pure lignin and acetylated lignin) and dialysis, flash-precipitation methods, sonication, water-in-oil microemulsion methods as well as precipitation methods with pH lowering by acid. LNP are also used as micro-emulsions in the synthesis of metal/metal-oxide nanoparticles. The lignin precursor and the nanoparticle synthesis technique affect the physical properties of these particles and the wide variation in the surface properties of the LNP makes them suitable for different environment-friendly applications. Among the different available methods, acid precipitation is simple and cost-effective. Nanoparticle synthesis from lignin is environmentally benign and in accordance with green chemistry principles as it utilizes lignin available in the form of industrial/agricultural waste.

6.1.1 Synthesis Methods

One type of synthesis method used to develop lignin nanoparticles is the process of acid precipitation. One study designed the lignin nanoparticles using a SERSL solution in carbon monoxide. Then 1M of 20 mL HCl was added dropwise into the reaction mixture, which was in a prominent nitrogen environment. Afterward, the nanoparticles were washed in ethanol and water to stabilize the pH at 7.00 [173]. Utilizing the acid precipitation method improved thermal stability as initial thermal degradation tests showed less than 20 percent degradation at the 50-300 degrees Celsius range [173]. However, acid precipitation has been reported to be weak against agglomeration or particles' attraction to each other or solid surfaces [174]. Another study that used acid precipitation synthesis to develop silver infused lignin nanoparticles coated with poly diallyldimethylammonium chloride found that these nanoparticles could neutralize common gram-negative and gram-positive bacteria while using ten times less silver than silver nanoparticles or silver nitrate solutions [175]. However, the study did not thoroughly discuss the environmental impacts of this type of lignin nanoparticle as the silver released by the nanoparticles are potentially harmful to the environment. Another type of synthesis method used is ultrasonication. One study synthesized lignin nanoparticles first through an aqueous suspension of the lignin. Afterward, the lignin was taken through the process of sonication for approximately 1 hour and then dried [176]. Although the study showed uniformity in the shape and size distribution of the lignin nanoparticles, the study failed to discuss the nanoparticles' thermal or corrosion properties [176]. Another study that developed lignin nanoparticles incorporated with waterborne polyurethanes nanocomposites found an inverse relationship between ultrasonication treatment time and the lignin's particle size [177]. Furthermore, nanocomposite had improved tensile strength and thermal stability [177]. The solvent exchange has also been a commonly used synthesis method used in the fabrication of lignin nanoparticles. The study designed the nanoparticles by using tetrahydrofuran as the solvent. Because tetrahydrofuran is not polar, it would be more soluble with lignin and would allow for better solvent interactions with water. The solvent exchange was done through dialysis [178]. The study found that there were a more uniform size distribution and a more spherical shape to the nanoparticles due to the lignin extracted from the kraft pulping process and the tetrahydrofuran [178]. Similarly, another study focused on biodegradable lignin nanoparticles and their medical applications. The iron (II, III) oxide infused lignin nanoparticles were developed by creating a mixture of lignin solution and oleic acid-coated iron (II, III) oxide nanoparticles. This was then mixed with tetrahydrofuran and then added into a dialysis bag in order to develop the lignin-iron (II, III) oxide nanoparticles [179]. The nanoparticles had uniform size distribution and spherical shape and exhibited superparamagnetic properties useful in magnetic resonance imaging [179]. However, the studies failed to mention the environmental effects of using tetrahydrofuran. A study that focuses on the characterization of tetrahydrofuran discusses how the chemical is an environmental pollutant and can cause human illnesses [180].

6.2 Experimental Set-up

Materials

The materials used were: Alkali Lignin (Sigma Aldrich); DMSO (Sigma Aldrich); 100 W UV lamp (P/N 34-0054-01); Potassium Hydroxide (Sigma); Sodium Hydroxide (NaOH)

Synthesis of Lignin nanoparticles (NP)

For the synthesis of UV-based LNP, 0.1g of Alkali Lignin was added to a 10 ml DMSO solution. This solution was magnetically stirred while being exposed to UV irradiation. After a certain exposure time, the basic catalyst was added drop-by-drop. The drop rate of the catalyst was varied 5 times to obtain 5 different sets of lignin NPs. The optimal sample was further exposed to 4 different UV exposure times. Two basic catalysts, NaOH and KOH are used.

Assembly of asymmetric supercapacitors

The nanoparticles were mixed with PVDF as the binder and NMP as the solvent. The substrate used is an Al foil of the dimensions 4 cm x 1 cm. The slurry was coated on the foil and placed in a vacuum oven at -20 Hg and 160˚C. A paper separator coated with the electrolyte (NaOH) was sandwiched between the two strip electrodes to complete the supercapacitor assembly.

Characterization

Material characterization involved XRD (Fig. 6.1a-b), SEM (Fig. 6.2), and FTIR (Fig. 6.3). XRD shows that the UV LNP at 12h 5s is more amorphous as indicated by a gentler curve of the intensity versus 2 theta. Comparatively, the UV LNP at 24h 15 s (a) is somewhat crystalline in nature as indicated by sharp regions in the plot. SEM shows that the 24h 15 s UVLNP (a) is more monodispersed and smaller in size than the UVLNP formed at 12 h 5s (b).

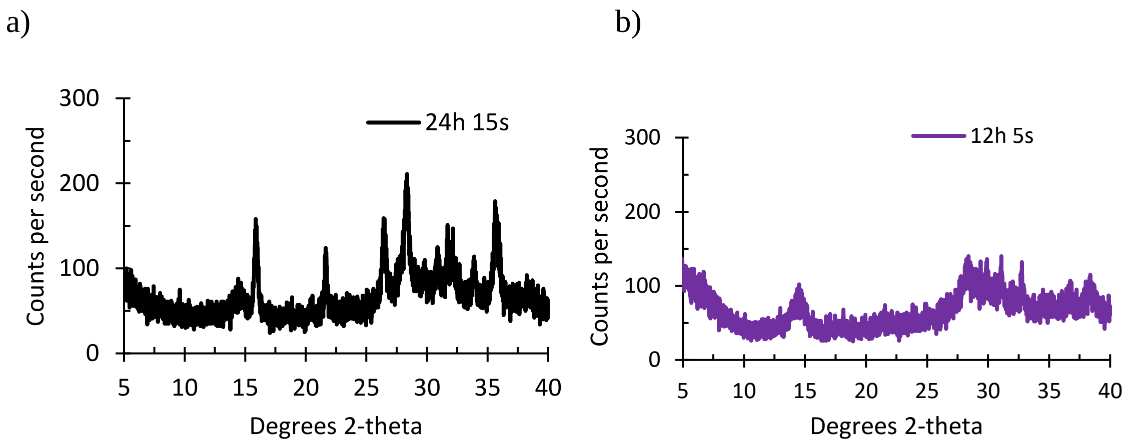

Fig. 6.1 XRD plots for alkali lignin np for a) 24 h US exposure and 15 s drop rate and b) 12 h US exposure and 5 s drop rate.

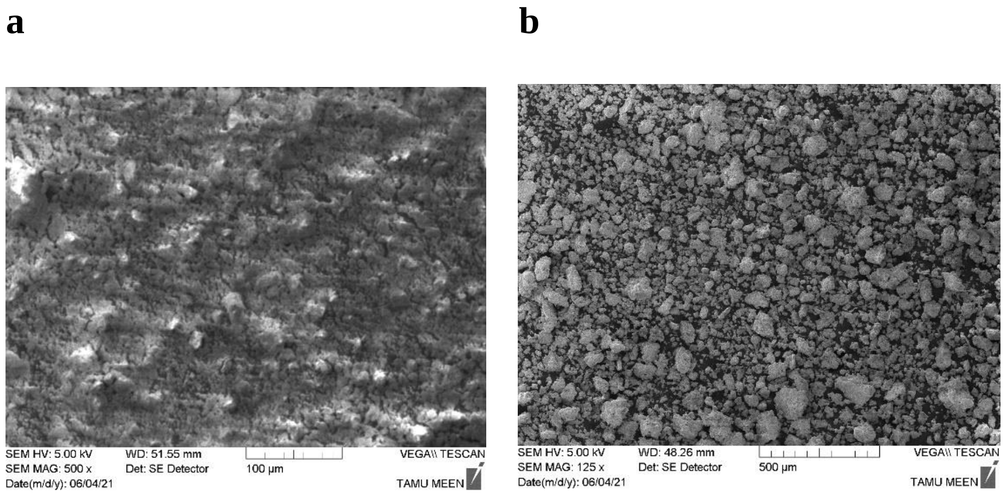

Fig. 6.2 SEM plots for alkali lignin np for a) 24 h US exposure and 15 s drop rate and b) 12 h US exposure and 5 s drop rate

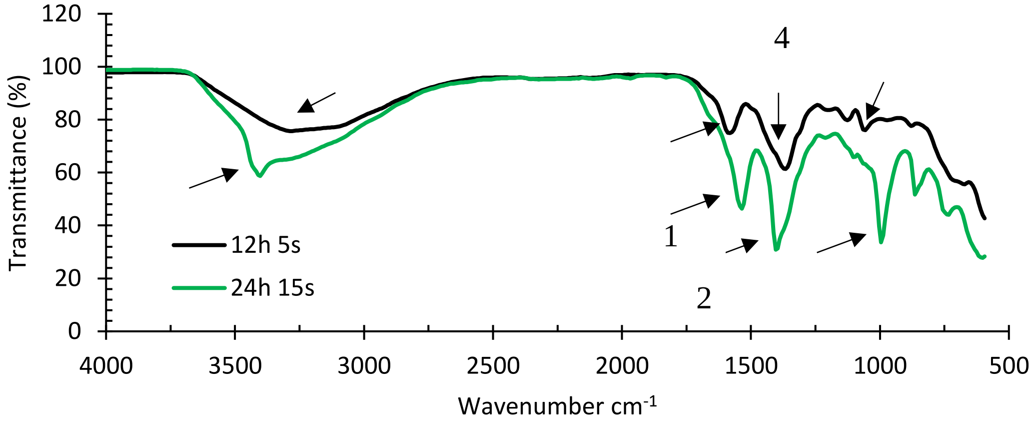

Fig. 6.3 FTIR plot for alkali lignin np.

In order to study the chemical composition of the UV based lignin nanoparticles, FTIR analysis was performed. Peak 1 at 1604 cm-1 and peak 2 1535 indicates the stretching vibration of C=C bonds in the aromatic rings. The peaks at about 1396 cm-1 and 1327 cm-1 can be attributed to the alkene groups present in lignin nanoparticles. It also corresponds to the stretching vibration of the guaiacyl ring in lignin. Peak 4 at 1302 cm-1 corresponds to the OH in-plane bend. The peaks at 1204 and 1099 correspond to the stretching vibrations of the syringyl and guaiacyl groups, and the vibration of ether bonds. The peaks in the range 1184 - 1150 represent the bond vibration in the carboxylic acid groups and phenolic groups of lignin nanoparticles. The FTIR results obtained are similar to the those reported in the literature.

6.3 Results and Discussions

The initial type of nanoparticles examined were produced using the UV synthesis method. Two sets of lignin nanoparticles were synthesized. The parameters controlling the particle size are (a) the catalyst, (b) the rate at which the catalyst was added, and (c) the radiation exposure time. The particles were characterized for their electrochemical and surface properties.

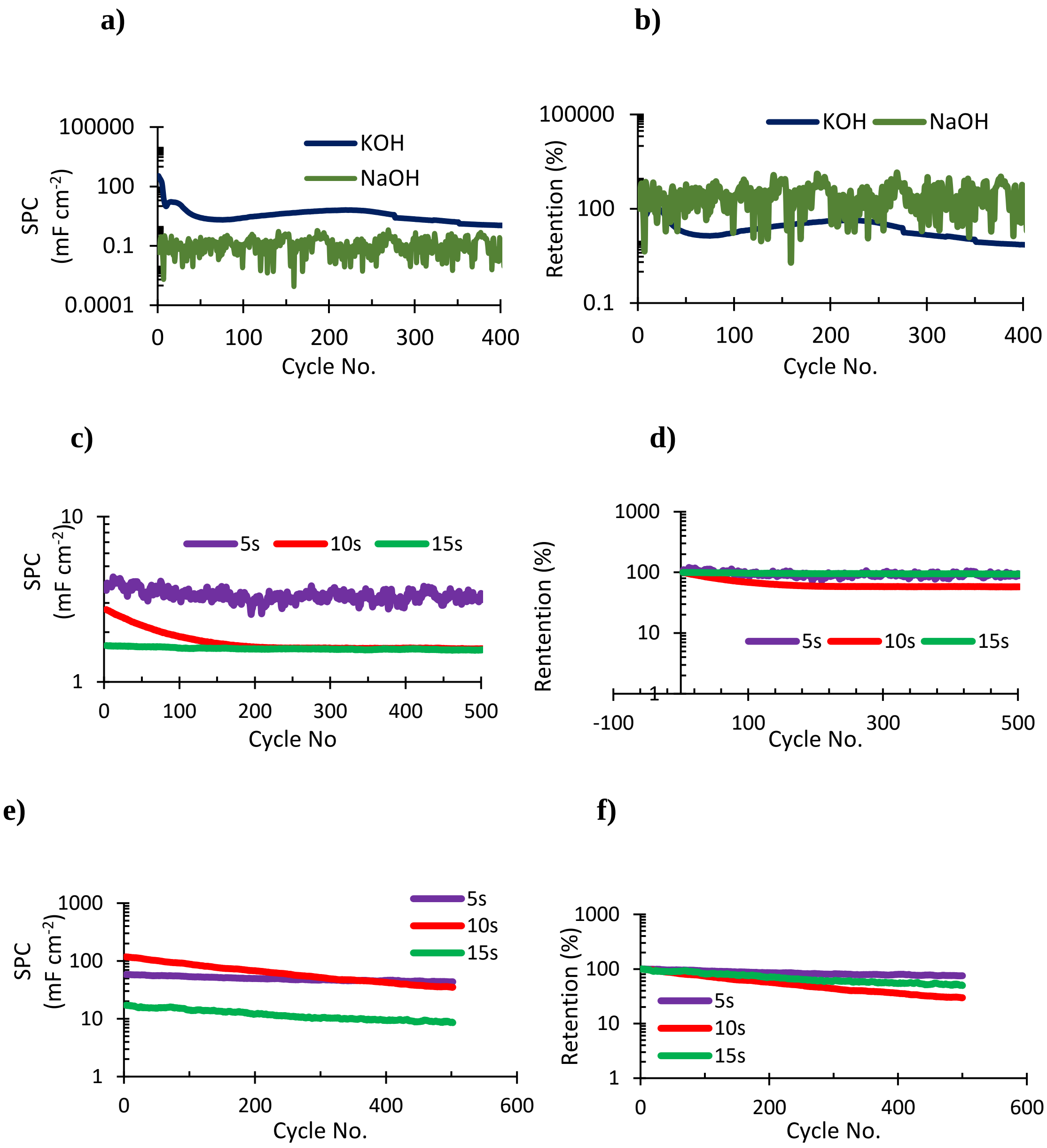

Fig. 6.4 Comparative electrochemical plots for nano-lignin alkaline lignin based supercapacitors: for varying drop rate of catalyst (KOH vs NaOH) at exposure time of

24 hours a) specific capacitance and b) retention variation with cycles; for varying drop rate of catalyst (KOH) at exposure time of 12 hours c) specific capacitance and d) retention variation with cycles; for varying drop rate of catalyst (KOH) at exposure time of 24 hours e) specific capacitance and f) retention variation with cycles.

To understand the effect of different catalysts on its pseudocapacitance behavior, the electrochemical performance of UV based lignin np synthesized using NaOH (UVlnp-NaOH) was compared to that of UV based lignin np synthesized using KOH (UVlnp-KOH). For both samples, the UV exposure time was 24 hours with a drop addition rate of 1 drop per second. Two cyclic charge–discharge (CCD) experiments were run for 400 cycles at a current density of 2.8 mA cm-2. The assembled pseudocapacitor is symmetric with UV based lignin nps as the electroactive material. As observed in **Fig. 6.4a and b**, the initial and final areal specific capacitance (SPC) values for the UVlnp-KOH pseudocapacitor are 15 mF cm-2 and 1.92 mF cm-2 and for UVlnp-NaOH pseudocapacitor are 0.5 mF cm-2 and 0.06 mF cm-2. The noise in the UVlnp-NaOH pseudocapacitor can be attributed to the particle size distribution of the nanoparticles.

To understand the effect of the particle size on the electrochemical performance, KOH was selected as the catalyst. Further samples of UVlnp-KOH were synthesized with varying drop addition rates of the catalyst. The lignin nps were irradiated at 24 hours. Three different drop rates of 1 drop per 5 seconds (24h 5s), 1 drop per 10 seconds (24h 10s), and 1 drop per 15 seconds (24h 15s) were implemented. CCD tests were performed for 500 cycles at Fig 6.4c and d display the SPC and retention for these nps.

Even though the 24h 5s sample displays the highest SPC of 3.576 mF cm-2, the system exhibits a lot of fluctuations. Whereas sample 24h 15s exhibits a smooth performance for 500 cycles with a high retention of ~ 95% making it more reliable for electrochemical applications. Initially sample 24h 10s starts with a high SPC 2.9 mF cm-2, however it can be observed that the SPC of the system quickly drops with a final retention of ~57%. Hence, the rate of addition of the basic catalyst affects not only the particle size but also the electrochemical performance of the system. For 24 hours UV exposure time, the sample 24h 15s is selected as the optimal sample.

Along with the catalyst drop addition rate, another parameter that plays a vital role in controlling particle size and thereby improving the electrochemical performance is UV the radiation exposure time. The next set of samples tested were irradiated for 12 hours with the same drop addition rates. The samples were named 12h 5s, 12h 10s, and 12h 15s respectively. From Fig 6.4 d and e it can be observed that initially the sample 12h 10s exhibits a better performance. But the final SPC of the system drops down with a final retention of ~50%, similar to the performance of 24h 10s. The lowest performance is exhibited by the sample 12h 15s. The sample 12h 5s exhibits a stable and high performance throughout with a retention of ~85%. The initial and final SPC values are 58.1 mF cm-2 and 49.3 mF cm-2. Hence, for 12 hours UV exposure time, the sample 12h 5s is selected as the optimal sample.

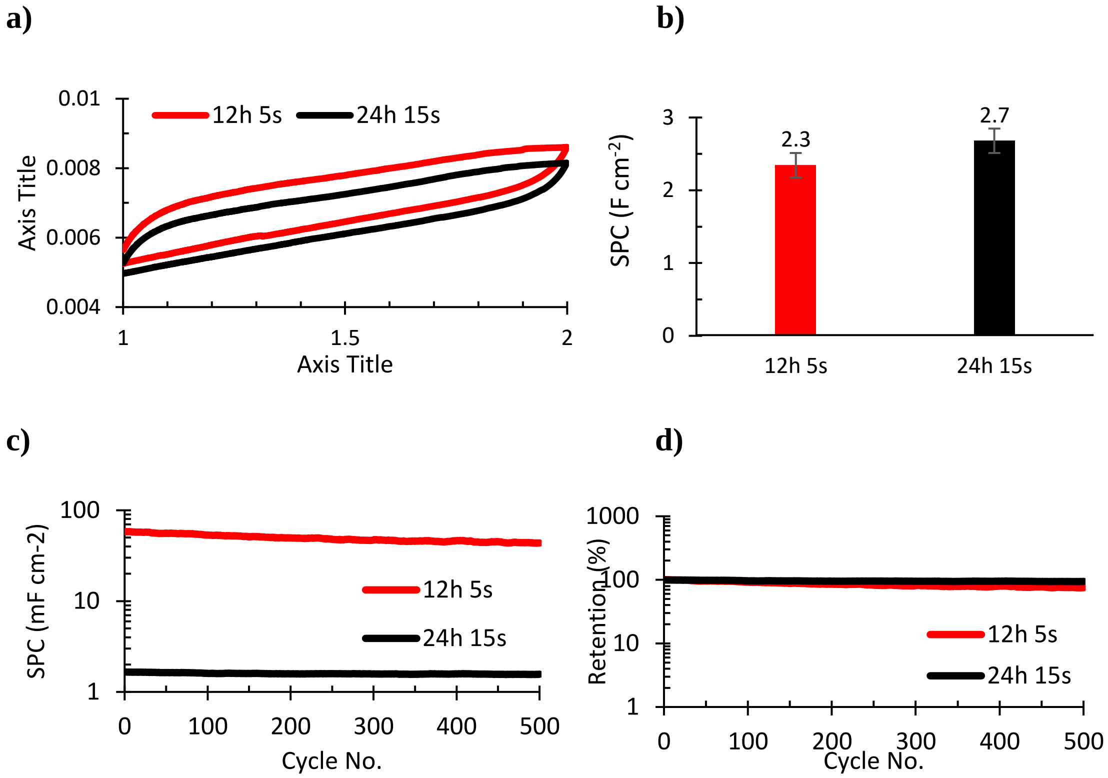

Fig. 6.5 Comparative electrochemical plots for nano-lignin alkali lignin based supercapacitors: a) CV, b) SPC for the CV plots, c) CCD for 500 cycles and d) retention for the 500 cycles.

In order to characterize the supercapacitor, a cyclic charge-discharge (CCD) test was performed for 500 cycles at 0.1 A g^{-1} current density. **Fig 6.5c** shows the specific capacitance and the respective retention percentage of the asymmetric supercapacitor. With an initial specific capacitance of 29.74 mF g-1 and the final specific capacitance of 26 mF g-1, the asymmetric supercapacitor displayed a high retention of ~ 87 %. Thus, only a marginal drop in the storage capacitance is seen. The maximum power density is 2016.82 mW kg^{-1} and the maximum energy density obtained is 33.62 mWh kg^{-1}.

UV – De-alkaline Lignin 12h vs. 24h

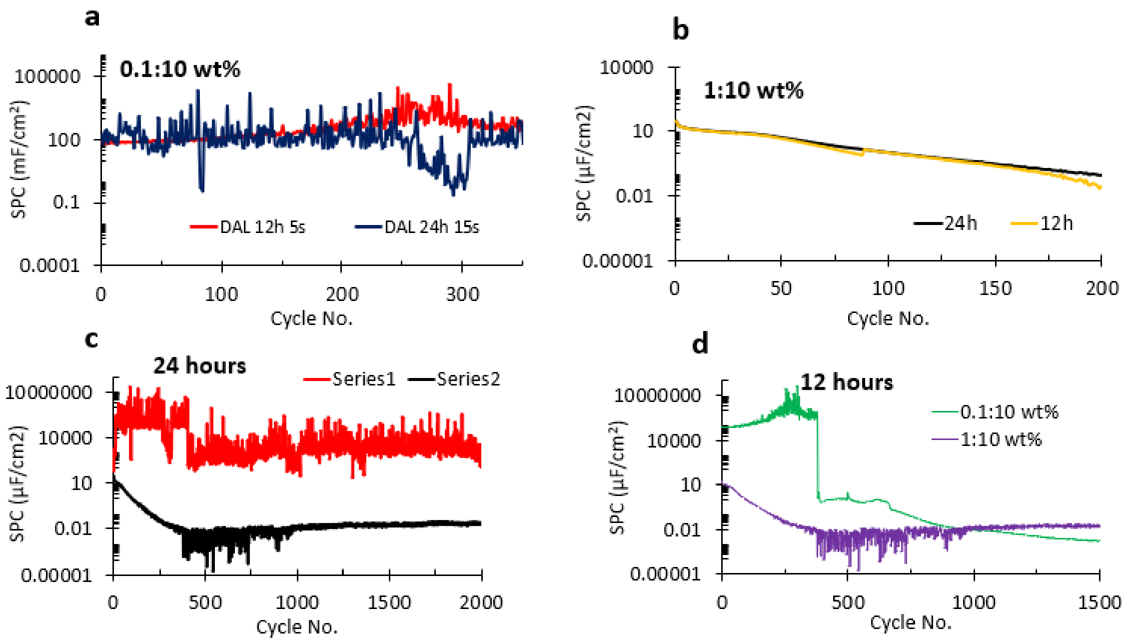

Fig. 6.6 Comparative electrochemical plots for De-alkaline (DAL) based supercapacitors.

1) Effect of lignin : catalyst weight ratio (Fig. 6.6a-b): The specific capacitances at a lower lignin : catalyst weight ratio (0.1:10) was at least 3 orders of magnitude higher than that at a higher lignin : catalyst ratio (1:10) for both UV exposure times (12h and 24 h).

2) Effect of exposure time at a given lignin: catalyst ratio (Fig. 6.6c-d): The specific capacitances were almost the same for both exposure times at each lignin : catalyst ratio. This indicated that for a particular lignin : catalyst weight ratio, the effect of UV exposure time was negligible in affecting the charge storage characteristics.

3) Effect of lignin: catalyst ratio at a constant UV exposure time: It is observed that a lower lignin : catalyst ratio has a higher specific capacitance (at least 3 orders of magnitude higher) at a constant UV-exposure time. When the exposure time was varied and the same two lignin : catalyst ratio were tested, there was no significant difference in the specific capacitances.

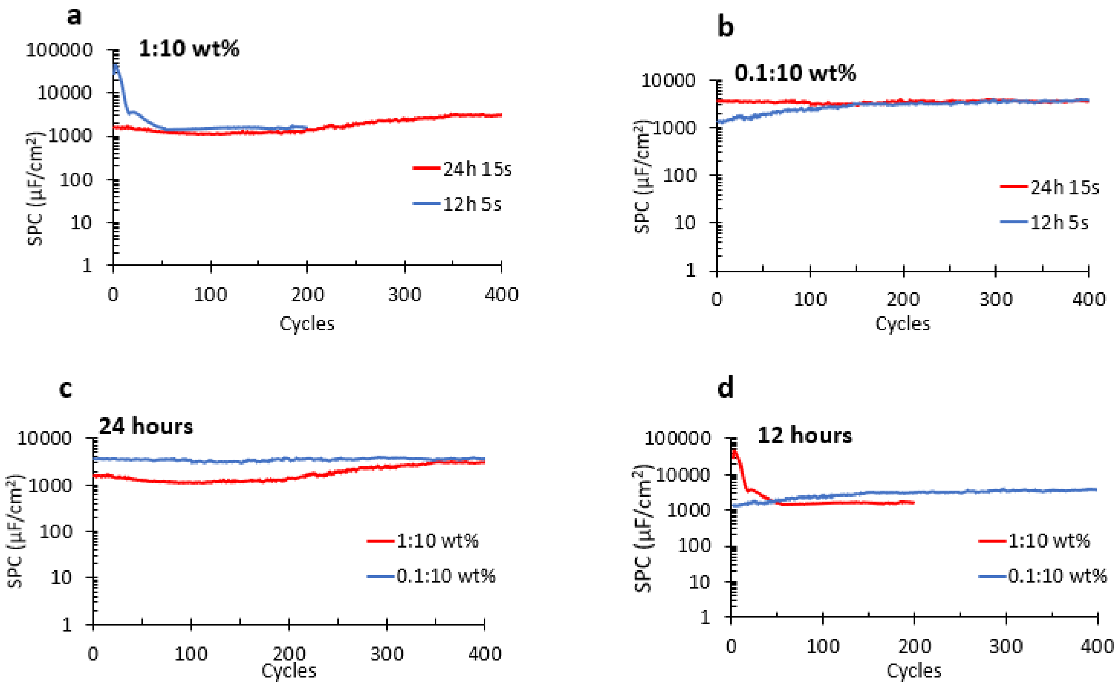

Fig. 6.7 Comparative electrochemical plots for nano-lignin lignosulfonate (UVLS) based supercapacitors.

1) Effect of exposure time at different LS: catalyst ratios (Fig. 6.7a-b): At different weight ratio of LS: catalyst, there is negligible difference in the specific capacitances. At different weight ratios of LS: catalyst too, the specific capacitances vary similarly.

2) Effect of weight ratios at constant exposure time (Fig. 6.7c-d): The specific capacitances for the lower LS: catalyst ratio is higher in both the cases (12 h and 24 h). Exposure time does not seem to impact too much the charge storing property of the material.

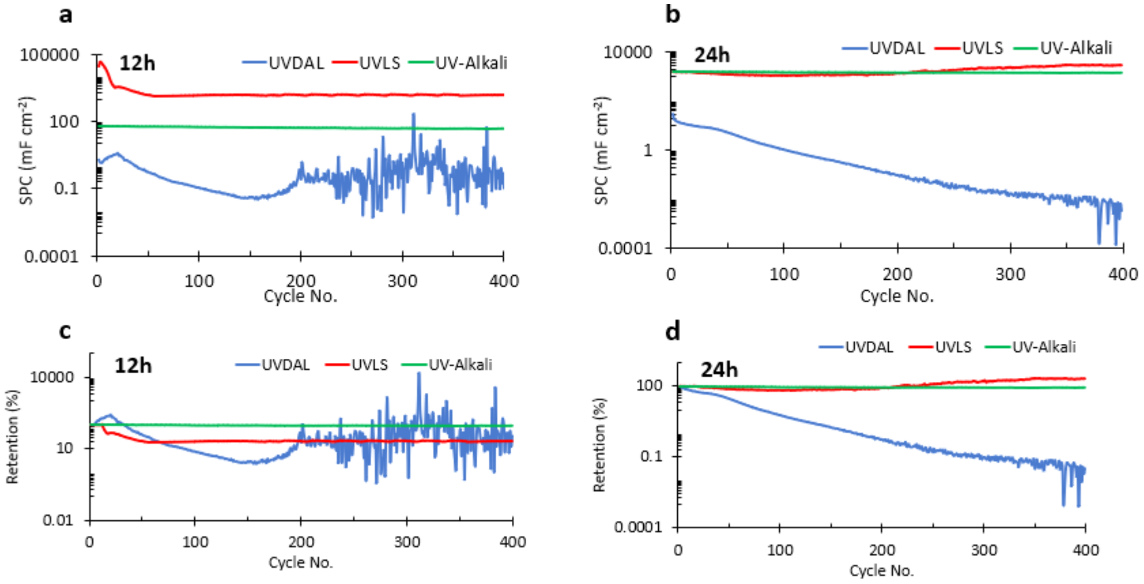

Fig. 6.8 Comparative electrochemical plots for nano-lignin based supercapacitors: a) specific capacitance variation with cycles at 12 hours UV exposure time, b) specific capacitance variation with cycles at 24 hours UV exposure time, c) retention variation with cycles at 12 hours UV exposure time, and d) retention variation with cycles at 24 hours UV exposure time. Alkali lignin (UV-Alkali is in green color), De-alkaline lignin (UVDAL is in blue color), and lignosulfonate (UVLS is in red color).

The electrochemical performances of nano-lignin based supercapacitors are compared in Fig. 6.8. Alkali lignin (UV-Alkali is in green color), De-alkaline lignin (UVDAL is in blue color), and lignosulfonate (UVLS is in red color). At 12 h UV exposure time, the specific capacitances follow the order: UVLS>UV-Alkali> UVDAL (Fig. 6.8 a) whereas retention follows the order UV-Alkali> UVLS = UVDAL (Fig. 6.8c) This is so because of the higher weight percentage of electroactive sulphonate groups in lignosulfonate which aid in redox reaction induced pseudocapacitance. The weight percentage of these sulphonate groups are low in alkali lignin and further lower in dealkaline lignin. DAL also has lower amount of methoxy groups and has C carbon percentage (44.4%) compared to alkali lignin (51.8%). In addition, DAL has low activation energy of depolymerization (86.5 – 133.2 kJ/mol at 299 – 350 ^{0}C) which leads to easier degradation compared to alkali lignin (120 – 143 kJ/mol at 300 – 350 ^{0}C). This lower activation energy of depolymerization leads to faster material degradation and hence lower retention. A higher moisture content in DAL (10.2%) compared to alkali lignin (1.2%) leads to further reduction in charge transfer behavior due to impedance from water molecules, thus, resulting in a lower specific capacitance. At 24 hour UV exposure time, the specific capacitance follow the same order: UVLS>UV-Alkali> UVDAL (Fig. 6.8b) whereas retention follows the order UVLS = UV-Alkali> UVDAL. At 24 hours UV exposure, there is reduction in particle size and increase in monodispersity as observed in the SEM images. For LS, the specific capacitance remains more or less the same. For DAL, there is a steeper decline in specific capacitance with cycles due to loss of active functional groups on the surface sites. On the other hand, for alkali lignin, the size reduction leads to higher surface to volume ratio of the material which accounts for higher surface area of contact. Also, the alkali lignin surface functional groups have a higher percentage of β-O-4 linkages which are comparatively more stable to breaking or degradation than the other linkages present in LS and DAL. In alkali lignin, since the surface functional groups are more active now in electrochemical event due to higher surface area, therefore, there is a corresponding increase in pseudocapacitance compared to that under 12 h UV exposure time. A higher UV exposure time also does not lead to more bond cleavage in LS accounting for its relatively stable retention behavior.

Micro-lignin

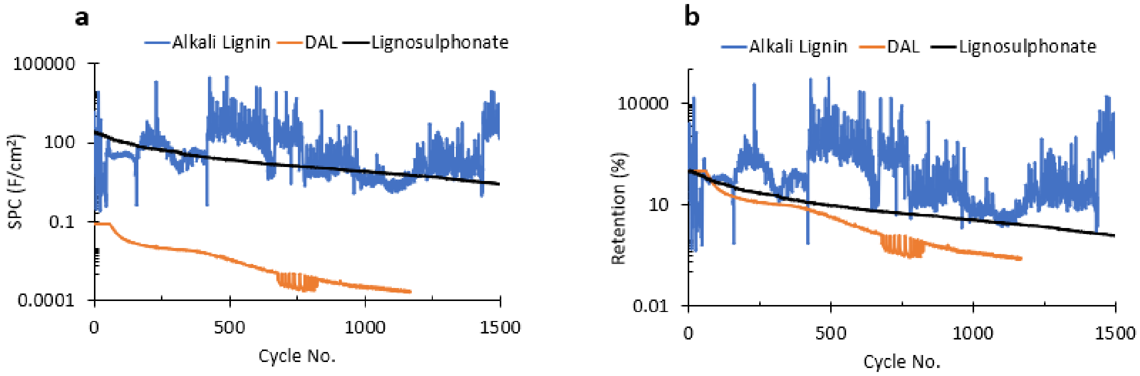

Fig. 6.9 Comparative electrochemical plots for micro fiber-lignin based supercapacitors: a) specific capacitance variation with cycles b) retention variation with cycles.

Figure 6.9 shows the electrochemical performances of micro-fiber lignin based supercapacitors. Though the starting specific capacitance of LS is the highest (Fig. 6.9a) due to the presence of a high amount of sulphonate groups, it falls behind that of alkali lignin's specific capacitance after a few hundred cycles. This is because alkali lignin has highly stable β-O-4 linkage groups that resist material degradation and consequent availability of active sites for pseudocapacitance. Hence, the retention (Fig 6.9b) follows the order Alkali lignin > LS > DAL. The DAL has the least specific capacitance and retention. This is because of less electroactive oxide and sulphonate groups, high moisture content, low carbon percentage, and a higher activation energy of depolymerization in DAL which leads to easier material degradation accounting for the least retention.

CHAPTER VII

CONCLUSIONS AND FUTURE RECOMMENDATIONS

7.1 Conclusions

To meet future energy demand in a sustainable manner, renewable energy technologies will need to be advanced to a great extent. As far as energy storage technologies are concerned, there is a huge potential for using plant based sources as raw materials. Even though plant based carbon has immense potential for use in electrochemical devices such as supercapacitors, there are many outstanding challenges to be solved. Hence, plant based supercapacitors have not yet been commercialized. Some challenges that exist include understanding the complex surface chemistry, effect of structure of molecules, morphology, dopant and impurity effects, and pore size and pore distribution effects on the electrochemical performance of plant based devices. Naturally occurring lignin, found in plants, is an abundant source of carbon that can be fruitfully utilized in supercapacitor applications. However, lignin has a very complex structure and its surface chemistry is not yet completely understood. This work utilized different variants of lignin morphologies (micro-fiber lignin and spherical nano-lignin). For each of the morphology of lignin, different chemical structures (alkali lignin (AL), lignosulfonate (LS), and dealkaline lignin (DAL)) were studied for their electrochemical performance in quasi solid-state flexible supercapacitors.

Effects of micro-fiber lignin morphology: Alkali lignin showed the best promising electrochemical performance among the lignin variants considering cycle life and charge storage ability. Additionally, the micro-fiber lignin had comparatively better performance than the nano spherical lignin variants. For the three chemical structures of fiber-lignin, the specific capacitance (SPC) varied as LS > AL > DAL and the retention varied as AL > LS > DAL. Though the starting specific capacitance of LS is the highest due to the presence of a high amount of sulphonate groups, it falls behind that of alkali lignin's specific capacitance after a few hundred cycles. This is because alkali lignin has highly stable β-O-4 linkage groups that resist material degradation and consequent availability of active sites for pseudocapacitance. The DAL has the least specific capacitance and retention. This is because of fewer electroactive oxide and sulphonate groups, high moisture content, low carbon percentage, and a higher activation energy of depolymerization in DAL which leads to easier material degradation accounting for the least retention. Various AL structures were explored that included impregnation with metal oxides, including transition metal oxides, metallic tungstates, bimetallic tungstates, and novel nanoparticles. In AL structures, the SPC trend was- AL-MnO2->AL-NiWO4> AL-NiCoWO4 >AL. Thus, decoration with metal oxides tremendously enhances electrochemical performance due to the pseudocapacitance property. The electrochemical performance was better than many state-of-the-art devices.

Various material synthesis strategies for lignin supercapacitors were also explored as part of this work including hydrothermal synthesis and microwave synthesis. The processing focused on green chemistry enabled synthesis of materials. A novel route for processing UV-rays impregnated lignin nanoparticles was also developed for the first time in this work. For the first time, synchrotron tomography was used to study the surface chemistry features of lignin electrode and characterize its surface. Synthesized supercapacitors were tested for durability, flexibility, and longevity. Thus, this work focused on and improved several design aspects of a flexible lignin based supercapacitor.

Roles of nano-spherical lignin morphology: For the three chemical structures of nano-lignin, the SPC varied as LS> AL > DAL and the retention varied as AL > LS = DAL. The effect of UV exposure time was also studied. A higher UV exposure time led to greater loss of electroactive functional groups in LS and DAL leading to less charge storage ability. In AL, the effect of size reduction was an increase in SPC due to comparatively lesser loss of surface functional groups on account of more stable β-O-4 linkages.

Both in the micro-fiber morphology and in the nano-spherical morphology, different structures of lignin have different specific capacitances and retention. These indicate that lignin structure and morphology, along with processing, play prominent roles in affecting the charge storage and transfer in electrochemical reactions. Micro-fiber lignin showed higher specific capacitance than nano-spherical lignin. This is attributed to a greater loss of electroactive surface functional groups in nano-spherical lignin.

7.2 Future recommendations

This work generated new insights into the use of lignin for application as electrode materials. Future recommendations are provided in the following:

1) A careful and cautious study of the natural components of lignocellulose biomass, its various sources, surface area, chemistry, pore size, and pore distribution are paramount to understanding the working of these electrodes. Study of variants of lignin from different sources can be carried out. These studies should focus on both structure and morphologies of lignin.

2) Theoretical studies relating molecular structure and morphology to electrochemical performances may be performed.

3) Insights and knowledge generated from this work may be extended to other biomass systems like cellulose and hemicellulose. Extensive studies should be carried out on those systems to help obtain consistent performance of devices fabricated from them.

4) In bio-carbon of low surface area, ultra-small micropores are present. These micropores have been identified as the source of the high capacitance that the systems exhibit as opposed to the generally accepted view that capacitance is derived from the heteroatoms undergoing Faradic reactions. Further study on manipulation of the pore size, controlled pore distribution, and their effect on the capacitive performance is needed.

5) Multiple other morphologies like aerogels, mat, film, for lignin may be investigated. Further research may be required to understand fully the role of morphology in influencing the performance of the lignin supercapacitors.

6) Biomass-derived materials have low energy densities because they are electronically insulating and therefore have limited functionality. Chemical and physical manipulation of the materials is required for additional functionality. They require proper integration with other conductive and functioning materials.

7) A single pretreatment process is not able to meet the energy and process efficiency requirements often needed for commercial utilization. Hence, an integrated pretreatment strategy is crucial. Application-specific customized pretreatment and processing methods (cascade utilization) of lignocellulose is an innovative strategy for electrochemical devices.

8) An overlooked yet very important aspect for consideration should be life cycle analysis (LCA) of the lignocellulosic biomass from the end application point of view. The overall impact on environment, energy balance ratio (ratio of the heat content of the material to primary energy input from non-renewable material), and carbon footprint should be an important criterion for lignocellulose applications in energy storage.

9) There is a need for combined experimental and theoretical studies that can provide new insights into physical parameter modulation for lignocellulosic biomass. For instance, recently, the pore size distribution was theoretically shown to relate to the tuning of density.

10) The electrolyte system plays an important role in any electrochemical energy system. The influence of the electrolyte is a deciding factor in the performance. Studying the effect of the electrolyte system on the physical properties and interactions at a molecular level of the lignocellulose biomass is extremely crucial. New insights that may be gained

from such studies can help the supercapacitors or batteries work with a higher conductivity at room temperature and also to operate at higher voltages.

REFERENCES

1. Poizot, P. and F. Dolhem, *Clean energy new deal for a sustainable world: from non-CO2 generating energy sources to greener electrochemical storage devices.* Energy & Environmental Science, 2011. **4**(6): p. 2003-2019.
2. Asif, M. and T. Muneer, *Energy supply, its demand and security issues for developed and emerging economies.* Renewable and Sustainable Energy Reviews, 2007. **11**(7): p. 1388-1413.
3. Dincer, I., *Renewable energy and sustainable development: a crucial review.* Renewable and Sustainable Energy Reviews, 2000. **4**(2): p. 157-175.
4. Ellabban, O., H. Abu-Rub, and F. Blaabjerg, *Renewable energy resources: Current status, future prospects and their enabling technology.* Renewable and Sustainable Energy Reviews, 2014. **39**: p. 748-764.
5. Chu, S. and A. Majumdar, *Opportunities and challenges for a sustainable energy future.* Nature, 2012. **488**(7411): p. 294-303.
6. Hoffert, M.I., et al., *Advanced technology paths to global climate stability: energy for a greenhouse planet.* Science, 2002. **298**(5595): p. 981-7.
7. Yue, Y. and H. Liang, *3D Current Collectors for Lithium-Ion Batteries: A Topical Review.* Small Methods, 2018. **2**(8): p. 1800056.
8. Yue, Y., et al., *Hierarchical Structured Cu/Ni/TiO2 Nanocomposites as Electrodes for Lithium-Ion Batteries.* ACS Applied Materials & Interfaces, 2017. **9**(34): p. 28695-28703.

9. Yue, Y. and H. Liang, *Micro- and Nano-Structured Vanadium Pentoxide (V2O5) for Electrodes of Lithium-Ion Batteries.* Advanced Energy Materials, 2017. **7**(17): p. 1602545.

10. Zhang, Y., et al., *Chemo-mechanical degradation in V2O5 thin film cathodes of Li-ion batteries during electrochemical cycling.* Journal of Materials Chemistry A, 2019.

11. Yue, Y. and H. Liang, *Hierarchical micro-architectures of electrodes for energy storage.* Journal of Power Sources, 2015. **284**: p. 435-445.

12. Jha, S., V. Ponce, and J.M. Seminario, *Investigating the effects of vacancies on self-diffusion in silicon clusters using classical molecular dynamics.* Journal of Molecular Modeling, 2018. **24**(10): p. 290.

13. Kyeremateng, N.A., T. Brousse, and D. Pech, *Microsupercapacitors as miniaturized energy-storage components for on-chip electronics.* Nature Nanotechnology, 2016. **12**: p. 7.

14. Yu, D., et al., *Emergence of fiber supercapacitors.* Chemical Society Reviews, 2015. **44**(3): p. 647-662.

15. Wang, F., et al., *Latest advances in supercapacitors: from new electrode materials to novel device designs.* Chem Soc Rev, 2017. **46**(22): p. 6816-6854.

16. Miller, J.R. and P. Simon, *Electrochemical Capacitors for Energy Management.* Science, 2008. **321**(5889): p. 651-652.

17. El-Kady, M.F. and R.B. Kaner, *Scalable fabrication of high-power graphene micro-supercapacitors for flexible and on-chip energy storage.* Nature Communications, 2013. **4**: p. 1475.

18. Lokhande, C.D., D.P. Dubal, and O.-S. Joo, *Metal oxide thin film based supercapacitors.* Current Applied Physics, 2011. **11**(3): p. 255-270.

19. Yuan, C., et al., *Mixed Transition-Metal Oxides: Design, Synthesis, and Energy-Related Applications.* Angewandte Chemie, 2014. **53**(6): p. 1488-1504.

20. Yuan, D., et al., *Preparation of monodisperse carbon nanospheres for electrochemical capacitors.* Electrochemistry Communications, 2008. **10**(7): p. 1067-1070.

21. Lu, X., et al., *Flexible solid-state supercapacitors: design, fabrication and applications.* Energy & Environmental Science, 2014. **7**(7): p. 2160-2181.

22. Conway, B.E., V. Birss, and J. Wojtowicz, *The role and utilization of pseudocapacitance for energy storage by supercapacitors.* Journal of Power Sources, 1997. **66**(1): p. 1-14.

23. Pech, D., et al., *Ultrahigh-power micrometre-sized supercapacitors based on onion-like carbon.* Nature Nanotechnology, 2010. **5**(9): p. 651-654.

24. Liu, C.-C., et al., *Electrochemical micro-capacitors of patterned electrodes loaded with manganese oxide and carbon nanotubes.* Journal of Power Sources, 2011. **196**(13): p. 5761-5768.

25. Yang, P. and W. Mai, *Flexible solid-state electrochemical supercapacitors.* Nano Energy, 2014. **8**: p. 274-290.

26. Manisha, V., P. Tonya, and J. Li, *Supercapacitors: Review of Materials and Fabrication Methods.* Journal of Energy Engineering, 2013. **139**(2): p. 72-79.
27. Liu, L., Y. Feng, and W. Wu, *Recent progress in printed flexible solid-state supercapacitors for portable and wearable energy storage.* Journal of Power Sources, 2019. **410-411**: p. 69-77.
28. Zeng, L., L. Qiu, and H.-M. Cheng, *Towards the practical use of flexible lithium ion batteries.* Energy Storage Materials, 2019.
29. Palchoudhury, S., et al., *Flexible Supercapacitors: A Materials Perspective.* Frontiers in Materials, 2019. **5**(83).
30. Dubal, D.P., et al., *Towards flexible solid-state supercapacitors for smart and wearable electronics.* Chemical Society Reviews, 2018. **47**(6): p. 2065-2129.
31. Liu, Y., M. Pharr, and G.A. Salvatore, *Lab-on-Skin: A Review of Flexible and Stretchable Electronics for Wearable Health Monitoring.* ACS Nano, 2017. **11**(10): p. 9614-9635.
32. Han, Y. and L. Dai, *Conducting Polymers for Flexible Supercapacitors.* Macromolecular Chemistry and Physics, 2019. **220**(3): p. 1800355.
33. Zhang, Z., et al., *Flexible fiber-shaped supercapacitors with high energy density based on self-twisted graphene fibers.* Journal of Power Sources, 2019. **433**: p. 226711.
34. Ho, K.-C. and L.-Y. Lin, *A review of electrode materials based on core–shell nanostructures for electrochemical supercapacitors.* Journal of Materials Chemistry A, 2019. **7**(8): p. 3516-3530.

35. Zhao, X., et al., *Fabrication, characteristics and applications of carbon materials with different morphologies and porous structures produced from wood liquefaction: A review*. Chemical Engineering Journal, 2019. **364**: p. 226-243.

36. Zhang, L.L. and X.S. Zhao, *Carbon-based materials as supercapacitor electrodes.* Chemical Society Reviews, 2009. **38**(9): p. 2520-2531.

37. Zhang, R., et al., *Coralloid Carbon Fiber-Based Composite Lithium Anode for Robust Lithium Metal Batteries.* Joule, 2018. **2**(4): p. 764-777.

38. Zhang, Y., et al., *Effects of activation temperatures on the surface structures and supercapacitive performances of porous carbon fibers.* Surface and Coatings Technology, 2018. **349**: p. 384-391.

39. Yue, L., et al., *Highly hydroxylated carbon fibres as electrode materials of all-vanadium redox flow battery.* Carbon, 2010. **48**(11): p. 3079-3090.

40. Xie, Y., et al., *Hierarchically nanostructured carbon fiber-nickel-carbon nanotubes for high-performance supercapacitor electrodes.* Materials Letters, 2017. **186**: p. 70-73.

41. Xiao, H., et al., *A comparison of the effect of hot stretching on microstructures and properties of polyacrylonitrile and rayon-based carbon fibers.* Journal of Materials Science, 2014. **49**(14): p. 5017-5029.

42. Li, K., et al., *Preparation of nitrogen-doped cotton stalk microporous activated carbon fiber electrodes with different surface area from*

hexamethylenetetramine-modified cotton stalk for electrochemical degradation of methylene blue. Results in Physics, 2017. **7**: p. 656-664.

43. Vujković, M., et al., *Mechanically activated carbonized rayon fibers as an electrochemical supercapacitor in aqueous solutions.* Electrochimica Acta, 2017. **245**: p. 796-806.

44. Qiang, C., et al., *Magnetic properties and microwave absorption properties of carbon fibers coated by Fe3O4 nanoparticles.* Journal of Alloys and Compounds, 2010. **506**(1): p. 93-97.

45. Liu, Y. and S. Kumar, *Recent Progress in Fabrication, Structure, and Properties of Carbon Fibers.* Polymer Reviews, 2012. **52**(3): p. 234-258.

46. Wang, J., et al., *Biomass derived carbon for energy storage devices.* Journal of Materials Chemistry A, 2017. **5**(6): p. 2411-2428.

47. Enock, T.K., et al., *Status of Biomass Derived Carbon Materials for Supercapacitor Application.* International Journal of Electrochemistry, 2017. **2017**: p. 6453420.

48. Herou, S., et al., *Biomass-derived electrodes for flexible supercapacitors.* Current Opinion in Green and Sustainable Chemistry, 2018. **9**: p. 18-24.

49. Wang, H., et al., *From lignin to valuable products–strategies, challenges, and prospects.* Bioresource Technology, 2019. **271**: p. 449-461.

50. Schlee, P., et al., *Free-standing supercapacitors from Kraft lignin nanofibers with remarkable volumetric energy density.* Chemical Science, 2019. **10**(10): p. 2980-2988.

51. Jeon, J.-W., et al., *Controlling Porosity in Lignin-Derived Nanoporous Carbon for Supercapacitor Applications.* ChemSusChem, 2015. **8**(3): p. 428-432.

52. Wei, W., et al., *Manganese oxide-based materials as electrochemical supercapacitor electrodes.* Chemical Society Reviews, 2011. **40**(3): p. 1697-1721.

53. Zhang, S.W. and G.Z. Chen, *Manganese oxide based materials for supercapacitors.* Energy Materials, 2008. **3**(3): p. 186-200.

54. Wang, Z., et al., *Long Cyclic Life in Manganese Oxide-Based Electrodes.* ACS Applied Materials & Interfaces, 2016. **8**(28): p. 18078-18088.

55. Nagarajan, N., M. Cheong, and I. Zhitomirsky, *Electrochemical capacitance of MnOx films.* Materials Chemistry and Physics, 2007. **103**(1): p. 47-53.

56. Zhang, Q.Z., et al., *Research Progress in MnO2 -Carbon Based Supercapacitor Electrode Materials.* Small, 2018. **14**(24): p. e1702883.

57. Zhang, Y., et al., *Electrochemical investigation of MnO2 electrode material for supercapacitors.* International Journal of Hydrogen Energy, 2011. **36**(18): p. 11760-11766.

58. Youe, W.-J., et al., *MnO2-deposited lignin-based carbon nanofiber mats for application as electrodes in symmetric pseudocapacitors.* International Journal of Biological Macromolecules, 2018. **112**: p. 943-950.

59. Yue, Y. and H. Liang, *A theoretical model to determine the capacity performance of shape-specific electrodes.* Journal of Power Sources, 2018. **390**: p. 242-248.

60. Yue, Y., et al., *Superhierarchical Nickel–Vanadia Nanocomposites for Lithium Storage.* ACS Applied Energy Materials, 2018. **1**(5): p. 2056-2066.

61. Yue, Y., et al., *Hierarchical structured nickel–copper hybrids via simple electrodeposition.* Journal of Applied Electrochemistry, 2018. **48**(3): p. 275-286.

62. Jha, S., et al., *Design and Synthesis of Lignin Based Flexible Supercapacitors.* ACS Sustainable Chemistry & Engineering, 2019.

63. Zhou, Z., et al., *Metal–Organic Framework Derived Spindle-like Carbon Incorporated α-Fe2O3 Grown on Carbon Nanotube Fiber as Anodes for High-Performance Wearable Asymmetric Supercapacitors.* ACS Nano, 2018. **12**(9): p. 9333-9341.

64. Guo, J., et al., *Direct growth of vanadium nitride nanosheets on carbon nanotube fibers as novel negative electrodes for high-energy-density wearable fiber-shaped asymmetric supercapacitors.* Journal of Power Sources, 2018. **382**: p. 122-127.

65. Li, Q., et al., *All Hierarchical Core–Shell Heterostructures as Novel Binder-Free Electrode Materials for Ultrahigh-Energy-Density Wearable Asymmetric Supercapacitors.* Advanced Science, 2019. **6**(2): p. 1801379.

66. Chupka, É.I. and T.M. Rykova, *Electrical properties of lignin.* Chemistry of Natural Compounds, 1983. **19**(1): p. 78-80.

67. Eranjaneya, H., et al., *Nickel tungstate nanoparticles: synthesis, characterization and electrochemical sensing of mercury(II) ions.* Journal of Materials Science: Materials in Electronics, 2019. **30**(4): p. 3574-3584.

68. Zhang, C., et al., *Two-Dimensional Tin Selenide Nanostructures for Flexible All-Solid-State Supercapacitors.* ACS Nano, 2014. **8**(4): p. 3761-3770.

69. Pandolfi, R.J., et al., *Xi-cam: a versatile interface for data visualization and analysis.* Journal of Synchrotron Radiation, 2018. **25**(4): p. 1261-1270.

70. Schindelin, J., et al., *Fiji: an open-source platform for biological-image analysis.* Nature Methods, 2012. **9**(7): p. 676-682.

71. Ago, M., et al., *Mesoporous carbon soft-templated from lignin nanofiber networks: microphase separation boosts supercapacitance in conductive electrodes.* RSC Advances, 2016. **6**(89): p. 85802-85810.

72. Thompson, A.C., et al., *Computed tomography using synchrotron radiation.* Nuclear Instruments and Methods in Physics Research, 1984. **222**(1): p. 319-323.

73. Chen, T. and L. Dai, *Flexible and wearable wire-shaped microsupercapacitors based on highly aligned titania and carbon nanotubes.* Energy Storage Materials, 2016. **2**: p. 21-26.

74. Noh, J., et al., *High performance asymmetric supercapacitor twisted from carbon fiber/MnO2 and carbon fiber/MoO3.* Carbon, 2017. **116**: p. 470-478.

75. Liu, S., et al., *Nitrogen-doped reduced graphene oxide for high-performance flexible all-solid-state micro-supercapacitors.* Journal of Materials Chemistry A, 2014. **2**(42): p. 18125-18131.

76. Xie, J., et al., *Layer-by-layer β-Ni(OH)2/graphene nanohybrids for ultraflexible all-solid-state thin-film supercapacitors with high electrochemical performance.* Nano Energy, 2013. **2**(1): p. 65-74.

77. Chen, F., et al., *Flexible Transparent Supercapacitors Based on Hierarchical Nanocomposite Films.* ACS Applied Materials & Interfaces, 2017. **9**(21): p. 17865-17871.

78. Liu, X.-Y., et al., *Preparation of a Carbon-Based Solid Acid Catalyst by Sulfonating Activated Carbon in a Chemical Reduction Process.* Molecules (Basel, Switzerland), 2010. **15**: p. 7188-96.

79. Ravishankar, K., et al., *Biocompatible hydrogels of chitosan-alkali lignin for potential wound healing applications.* Materials Science and Engineering: C, 2019. **102**.

80. Jaganyi, D., M. Altaf, and I. Wekesa, *Synthesis and characterization of whisker-shaped MnO2 nanostructure at room temperature.* Applied Nanoscience, 2013. **3**(4): p. 329-333.

81. He, L., et al., *Colorimetric sensing of silver ions based on glutathione-mediated MnO 2 nanosheets.* Sensors and Actuators B: Chemical, 2017. **254**.

82. Xie, Z., et al., *Production of Biologically Activated Carbon from Orange Peel and Landfill Leachate Subsequent Treatment Technology.* Journal of Chemistry, 2014. **2014**: p. 1-9.

83. Chaudhary, R. and P.L. Dhepe, *Solid base catalyzed depolymerization of lignin into low molecular weight products.* Green Chemistry, 2017. **19**(3): p. 778-788.

84. Hua, W., et al., *Analysis of Structural Units and Their Influence on Thermal Degradation of Alkali Lignins.* BioResources, 2016. **11**.

85. Chiou, Y.D., et al., *Cycle stability of the electrochemical capacitors patterned with vertically aligned carbon nanotubes in an LiPF6-based electrolyte.* Nanoscale, 2013. **5**(17): p. 8122-9.
86. Bi, Z., et al., *Biomass-derived porous carbon materials with different dimensions for supercapacitor electrodes: a review.* Journal of Materials Chemistry A, 2019. **7**(27): p. 16028-16045.
87. Gong, Y., et al., *Highly porous graphitic biomass carbon as advanced electrode materials for supercapacitors.* Green Chemistry, 2017. **19**(17): p. 4132-4140.
88. Deng, J., M. Li, and Y. Wang, *Biomass-derived carbon: synthesis and applications in energy storage and conversion.* Green Chemistry, 2016. **18**(18): p. 4824-4854.
89. Liu, Y., et al., *Self-crosslinking carbon dots loaded ruthenium dots as an efficient and super-stable hydrogen production electrocatalyst at all pH values.* Nano Energy, 2019. **65**: p. 104023.
90. Sheberla, D., et al., *Conductive MOF electrodes for stable supercapacitors with high areal capacitance.* Nature Materials, 2017. **16**(2): p. 220-224.
91. Pomerantseva, E., et al., *Energy storage: The future enabled by nanomaterials.* Science, 2019. **366**(6468): p. eaan8285.
92. Jha, S., et al., *NiWO4 Nanoparticle Decorated Lignin as Electrodes for Asymmetric Flexible Supercapacitors.* Journal of Materials Chemistry C, 2020.

93. Gür, T.M., *Review of electrical energy storage technologies, materials and systems: challenges and prospects for large-scale grid storage.* Energy & Environmental Science, 2018. **11**(10): p. 2696-2767.

94. Jin, H., et al., *Recent Progress in Biomass-Derived Electrode Materials for High Volumetric Performance Supercapacitors.* Advanced Energy Materials, 2018. **8**(23): p. 1801007.

95. Zhou, S., et al., *Upgrading earth-abundant biomass into three-dimensional carbon materials for energy and environmental applications.* Journal of Materials Chemistry A, 2019. **7**(9): p. 4217-4229.

96. Lu, H. and X.S. Zhao, *Biomass-derived carbon electrode materials for supercapacitors.* Sustainable Energy & Fuels, 2017. **1**(6): p. 1265-1281.

97. Zhang, G., et al., *Transition metal oxides with one-dimensional/one-dimensional-analogue nanostructures for advanced supercapacitors.* Journal of Materials Chemistry A, 2017. **5**(18): p. 8155-8186.

98. Gonçalves, J.M., et al., *Trimetallic oxides/hydroxides as hybrid supercapacitor electrode materials: a review.* Journal of Materials Chemistry A, 2020. **8**(21): p. 10534-10570.

99. Griffith, K.J., et al., *Niobium tungsten oxides for high-rate lithium-ion energy storage.* Nature, 2018. **559**(7715): p. 556-563.

100. Ling, T., et al., *Atomic-level structure engineering of metal oxides for high-rate oxygen intercalation pseudocapacitance.* Science Advances, 2018. **4**(10): p. eaau6261.

101. Huang, Y., et al., *Ni0.85Co0.15WO4 nanosheet electrodes for supercapacitors with excellent electrical conductivity and capacitive performance.* Nano Energy, 2018. **48**: p. 430-440.

102. Priya, A.M., et al., *Synthesis and characterization of CdWO4 nanocrystals.* Ceramics International, 2011. **37**(7): p. 2485-2488.

103. Rajpurohit, A.S., et al., *Fabrication of high energy density symmetric supercapacitor based on cobalt-nickel bimetallic tungstate nanoparticles decorated phosphorus-sulphur co-doped graphene nanosheets with extended voltage.* Chemical Engineering Journal, 2019. **371**: p. 679-692.

104. Denk, M., et al., *Metal Tungstates at the Ultimate Two-Dimensional Limit: Fabrication of a CuWO4 Nanophase.* ACS Nano, 2014. **8**(4): p. 3947-3954.

105. Lacomba-Perales, R., et al., *Optical absorption of divalent metal tungstates: Correlation between the band-gap energy and the cation ionic radius.* EPL (Europhysics Letters), 2008. **83**(3): p. 37002.

106. Hosseinpour-mashkani, S.M. and A. Sobhani-Nasab, *Simple synthesis and characterization of copper tungstate nanoparticles: investigation of surfactant effect and its photocatalyst application.* Journal of Materials Science: Materials in Electronics, 2016. **27**(7): p. 7548-7553.

107. Feng, M., et al., *Facile synthesis of cobalt/nickel tungstate and its application in hybrid supercapacitor.* International Journal of Chemical Studies, 2017. **5**(6): p. 1954-1960.

108. Kim, D.W., et al., *Electronic band structures and photovoltaic properties of MWO4 (M=Zn, Mg, Ca, Sr) compounds.* Journal of Solid State Chemistry, 2011. **184**(8): p. 2103-2107.

109. Hoang, K., M. Oh, and Y. Choi, *Electronic structure, polaron formation, and functional properties in transition-metal tungstates.* RSC Advances, 2018. **8**(8): p. 4191-4196.

110. Hoang, K., *Polaron formation, native defects, and electronic conduction in metal tungstates.* Physical Review Materials, 2017. **1**(2): p. 024603.

111. Mathew, T., N.M. Batra, and S.K. Arora, *Electrical conduction in CuWO4 crystals.* Journal of Materials Science, 1992. **27**(15): p. 4003-4008.

112. Montini, T., et al., *Synthesis, characterization and photocatalytic performance of transition metal tungstates.* Chemical Physics Letters, 2010. **498**(1): p. 113-119.

113. Yoon, S.H., et al., *Investigation of the relations between structure and microwave dielectric properties of divalent metal tungstate compounds.* Journal of the European Ceramic Society, 2006. **26**(10): p. 2051-2054.

114. Nagirnyi, V., et al., *Separation of excitonic and electron–hole processes in metal tungstates.* Journal of Luminescence, 2003. **102-103**: p. 597-603.

115. Bharati, R., R.A. Singh, and B.M. Wanklyn, *Electrical conduction in manganese tungstate.* Journal of Physics and Chemistry of Solids, 1982. **43**(7): p. 641-644.

116. Bharati, R., R.A. Singh, and B.M. Wanklyn, *Electrical conductivity, thermoelectric power and dielectric constant of NiWO4.* Journal of Materials Science, 1980. **15**(5): p. 1293-1296.

117. Liu, Y., et al., *A General Route to Prepare Low-Ruthenium-Content Bimetallic Electrocatalysts for pH-Universal Hydrogen Evolution Reaction by Using Carbon Quantum Dots.* Angew Chem Int Ed Engl, 2020. **59**(4): p. 1718-1726.

118. Wang, Y., et al., *High rate capability of mesoporous NiWO4–CoWO4 nanocomposite as a positive material for hybrid supercapacitor.* Materials Chemistry and Physics, 2016. **182**: p. 394-401.

119. Low, W.H., et al., *Recent development of mixed transition metal oxide and graphene/mixed transition metal oxide based hybrid nanostructures for advanced supercapacitors.* Journal of Alloys and Compounds, 2019. **775**: p. 1324-1356.

120. Li, W., et al., *Carbon quantum dots enhanced the activity for the hydrogen evolution reaction in ruthenium-based electrocatalysts.* Materials Chemistry Frontiers, 2020. **4**(1): p. 277-284.

121. Pourmortazavi, S.M., et al., *Facile Chemical Synthesis and Characterization of Copper Tungstate Nanoparticles.* Journal of Inorganic and Organometallic Polymers and Materials, 2014. **24**(2): p. 333-339.

122. M Zawawi, S.M., et al., *Structural and optical characterization of metal tungstates (MWO4; M=Ni, Ba, Bi) synthesized by a sucrose-templated method.* Chemistry Central Journal, 2013. **7**(1): p. 80.

123. Phuruangrat, A., T. Thongtem, and S. Thongtem, *Cyclic microwave-assisted synthesis and characterization of nano-crystalline alkaline earth metal tungstates.* Journal of the Ceramic Society of Japan, 2008. **116**(1353): p. 605-609.

124. Parhi, P., T.N. Karthik, and V. Manivannan, *Synthesis and characterization of metal tungstates by novel solid-state metathetic approach.* Journal of Alloys and Compounds, 2008. **465**(1): p. 380-386.

125. Cui, X., et al., *Selective synthesis and characterization of single-crystal silver molybdate/tungstate nanowires by a hydrothermal process.* Chemistry, 2004. **10**(1): p. 218-23.

126. Talebi, R., *Simple sonochemical synthesis and characterization of nickel tungstate nanoparticles and its photocatalyst application.* Journal of Materials Science: Materials in Electronics, 2016. **27**(4): p. 3565-3569.

127. Shinde, P.A. and S.C. Jun, *Review on Recent Progress in the Development of Tungsten Oxide Based Electrodes for Electrochemical Energy Storage.* ChemSusChem, 2020. **13**(1): p. 11-38.

128. Nithiyanantham, U., et al., *Shape-selective formation of MnWO4 nanomaterials on a DNA scaffold: magnetic, catalytic and supercapacitor studies.* RSC Advances, 2014. **4**(72): p. 38169-38181.

129. Nithiyanantham, U., et al., *Self-Assembled NiWO4 Nanoparticles into Chain-like Aggregates on DNA Scaffold with Pronounced Catalytic and Supercapacitor Activities.* Crystal Growth & Design, 2015. **15**(2): p. 673-686.

130. Jha, S., et al., *Design and synthesis of high performance flexible and green supercapacitors made of manganese-dioxide-decorated alkali lignin.* Energy Storage, 2020. **2**(5): p. e184.

131. González, A., et al., *Review on supercapacitors: Technologies and materials.* Renewable and Sustainable Energy Reviews, 2016. **58**: p. 1189-1206.

132. Shao, Y., et al., *Design and Mechanisms of Asymmetric Supercapacitors.* Chem Rev, 2018. **118**(18): p. 9233-9280.

133. Bessler, R., U. Duerig, and E. Koren, *The dielectric constant of a bilayer graphene interface.* Nanoscale Advances, 2019. **1**(5): p. 1702-1706.

134. Bellucci, S., et al., *Electrical Permittivity and Conductivity of a Graphene Nanoplatelet Contact in the Microwave Range.* 2018. **11**(12): p. 2519.

135. Shkal, F., et al., *Microwave Characterization of Activated Carbons.* Journal of Computer and Communications, 2018. **6**: p. 112-123.

136. Phillips, J., *Toward an Improved Understanding of the Role of Dielectrics in Capacitors.* Materials (Basel), 2018. **11**(9).

137. Dincer, I. and C. Acar, *A review on clean energy solutions for better sustainability*. International Journal of Energy Research, 2015. **39**(5): p. 585-606.

138. Jha, S., et al., *Influence of morphology on electrochemical and capacity performance of open-porous structured electrodes*. Journal of Applied Electrochemistry, 2020. **50**(2): p. 231-244.

139. Deng, X., et al., *Three-dimensional porous carbon materials and their composites as electrodes for electrochemical energy storage systems.* Materials Chemistry Frontiers, 2019. **3**(11): p. 2221-2245.

140. Chen, T., et al., *All-solid-state high performance asymmetric supercapacitors based on novel MnS nanocrystal and activated carbon materials.* Scientific Reports, 2016. **6**: p. 23289.

141. Chen, L., et al., *Synthesis and pseudocapacitive studies of composite films of polyaniline and manganese oxide nanoparticles.* Journal of Power Sources, 2010. **195**(11): p. 3742-3747.

142. Noori, A., et al., *Towards establishing standard performance metrics for batteries, supercapacitors and beyond.* Chemical Society Reviews, 2019. **48**(5): p. 1272-1341.

143. Qiu, Y., X. Zhang, and S. Yang, *High performance supercapacitors based on highly conductive nitrogen-doped graphene sheets.* Physical Chemistry Chemical Physics, 2011. **13**(27): p. 12554-12558.

144. Chen, J., et al., *Facile and scalable fabrication of three-dimensional Cu(OH)2 nanoporous nanorods for solid-state supercapacitors.* Journal of Materials Chemistry A, 2015. **3**(33): p. 17385-17391.

145. Gao, B., et al., *Recent progress in nanostructured transition metal nitrides for advanced electrochemical energy storage.* Journal of Materials Chemistry A, 2019. **7**(1): p. 14-37.

146. Ghosh, K., et al., *Development of 3D Urchin-Shaped Coaxial Manganese Dioxide@Polyaniline (MnO2@PANI) Composite and Self-Assembled 3D Pillared Graphene Foam for Asymmetric All-Solid-State Flexible Supercapacitor Application.* ACS Applied Materials & Interfaces, 2017. **9**(18): p. 15350-15363.

147. Wu, X., et al., *Lignin-derived electrochemical energy materials and systems.* Biofuels, Bioproducts and Biorefining, 2020. **14**(3): p. 650-672.

148. Tolba, R., et al., *Electrochemical oxidation of lignin at IrO2-based oxide electrodes.* Journal of Electroanalytical Chemistry, 2010. **649**(1): p. 9-15.

149. Jin, J., et al., *Lignin-based electrospun carbon nanofibrous webs as free-standing and binder-free electrodes for sodium ion batteries.* Journal of Power Sources, 2014. **272**: p. 800-807.

150. Shao, D., et al., *Electrochemical oxidation of lignin by two typical electrodes: Ti/SbSnO2 and Ti/PbO2.* Chemical Engineering Journal, 2014. **244**: p. 288-295.

151. Niu, X., et al., *Confined silicon nanospheres by biomass lignin for stable lithium ion battery.* Nanotechnology, 2017. **28**(40): p. 405401.

152. Admassie, S., et al., *A renewable biopolymer cathode with multivalent metal ions for enhanced charge storage.* Journal of Materials Chemistry A, 2014. **2**(6): p. 1974-1979.

153. Casado, N., et al., *Electrochemical Behavior of PEDOT/Lignin in Ionic Liquid Electrolytes: Suitable Cathode/Electrolyte System for Sodium Batteries.* ChemSusChem, 2017. **10**(8): p. 1783-1791.

154. Ates, M., et al., *Supercapacitor performances of RuO2/MWCNT, RuO2/Fullerene nanocomposites.* Energy Storage, 2019. **1**(5): p. e86.

155. Meng, X., et al., *Development of printable, flexible nickel-iron batteries based on composite electrodes.* Energy Storage, 2020. **2**(1): p. e105.

156. Espinoza-Acosta, J.L., et al., *Lignin in storage and renewable energy applications: A review.* Journal of Energy Chemistry, 2018. **27**(5): p. 1422-1438.

157. Naseem, A., et al., *Lignin-derivatives based polymers, blends and composites: A review.* International Journal of Biological Macromolecules, 2016. **93**: p. 296-313.

158. Duan, X., et al., *Controllable hydrothermal synthesis of manganese dioxide nanostructures: shape evolution, growth mechanism and electrochemical properties.* CrystEngComm, 2012. **14**(12): p. 4196-4204.

159. Abdelaziz, O.Y. and C.P. Hulteberg, *Physicochemical Characterisation of Technical Lignins for Their Potential Valorisation.* Waste and Biomass Valorization, 2017. **8**(3): p. 859-869.

160. Brazil, T.R., et al., *Structural, morphological, and thermal characterization of kraft lignin and its charcoals obtained at different heating rates.* Materials Research Express, 2018. **5**(4): p. 045502.

161. Goudarzi, A., L.-T. Lin, and F.K. Ko, *X-Ray Diffraction Analysis of Kraft Lignins and Lignin-Derived Carbon Nanofibers.* Journal of Nanotechnology in Engineering and Medicine, 2014. **5**(2).

162. Molina, A., et al., *On the meaning of the diffusion layer thickness for slow electrode reactions.* Physical Chemistry Chemical Physics, 2013. **15**(7): p. 2381-2388.

163. Seeber, R., C. Zanardi, and G. Inzelt, *The inherent coupling of charge transfer and mass transport processes: the curious electrochemical reversibility.* J ChemTexts

2016. **2**(2): p. 8.

164. Chen, H., et al., *A new insight into the rechargeable mechanism of manganese dioxide based symmetric supercapacitors.* RSC Advances, 2017. **7**(14): p. 8561-8566.

165. Demarconnay, L., E. Raymundo-Piñero, and F. Béguin, *Adjustment of electrodes potential window in an asymmetric carbon/MnO2 supercapacitor.* Journal of Power Sources, 2011. **196**(1): p. 580-586.

166. Xu, H., et al., *Flexible fiber-shaped supercapacitors based on hierarchically nanostructured composite electrodes.* Nano Research, 2015. **8**(4): p. 1148-1158.

167. Yun, J., et al., *All-solid-state flexible micro-supercapacitor arrays with patterned graphene/MWNT electrodes.* Carbon, 2014. **79**: p. 156-164.

168. Zhao, D., et al., *High Performance, Flexible, Solid-State Supercapacitors Based on a Renewable and Biodegradable Mesoporous Cellulose Membrane.* Advanced Energy Materials, 2017. **7**(18): p. 1700739.

169. Lu, X.-F., et al., *High-performance supercapacitors based on MnO2 tube-in-tube arrays.* Journal of Materials Chemistry A, 2015. **3**(32): p. 16560-16566.

170. Gao, Y., et al., *Highly flexible and transferable supercapacitors with ordered three-dimensional MnO2/Au/MnO2 nanospike arrays.* Journal of Materials Chemistry A, 2015. **3**(19): p. 10199-10204.

171. Parvez, K., et al., *Exfoliation of Graphite into Graphene in Aqueous Solutions of Inorganic Salts.* Journal of the American Chemical Society, 2014. **136**(16): p. 6083-6091.

172. Liu, C., et al., *Supercapacitors: 3D Porous Nanoarchitectures Derived from SnS/S-Doped Graphene Hybrid Nanosheets for Flexible All-Solid-State Supercapacitors.* Small, 2017. **13**.

173. Rahman, O.u., et al., *Lignin nanoparticles: synthesis, characterization and corrosion protection performance.* New Journal of Chemistry, 2018. **42**(5): p. 3415-3425.

174. Low, L.E., et al., *Lignin nanoparticles: The next green nanoreinforcer with wide opportunity.* Environmental Nanotechnology, Monitoring & Management, 2021. **15**: p. 100398.

175. Richter, A.P., et al., *An environmentally benign antimicrobial nanoparticle based on a silver-infused lignin core.* Nat Nanotechnol, 2015. **10**(9): p. 817-23.

176. Gilca, I.A., V.I. Popa, and C. Crestini, *Obtaining lignin nanoparticles by sonication.* Ultrasonics Sonochemistry, 2015. **23**: p. 369-375.

177. Garcia Gonzalez, M.N., et al., *Lignin nanoparticles by ultrasonication and their incorporation in waterborne polymer nanocomposites.* Journal of Applied Polymer Science, 2017. **134**(38): p. 45318.

178. Lievonen, M., et al., *A simple process for lignin nanoparticle preparation.* Green Chemistry, 2016. **18**(5): p. 1416-1422.

179. Figueiredo, P., et al., *In vitro evaluation of biodegradable lignin-based nanoparticles for drug delivery and enhanced antiproliferation effect in cancer cells.* Biomaterials, 2017. **121**: p. 97-108.

180. Huang, H., et al., *Enrichment and characterization of a highly efficient tetrahydrofuran-degrading bacterial culture.* Biodegradation, 2019. **30**(5): p. 467-479.